NTNU
Norwegian University of
Science and Technology

Harmonic Sharing in Microgrid Applications

Modeling, Developing and Evaluating a Microgrid Control System With Harmonic Sharing Capability

Ruben Buchmann

Master of Energy and Environmental Engineering
Submission date: June 2018
Supervisor: Olimpo Anaya-Lara, IEL
Co-supervisor: Raymundo Torres-Olguin, SINTEF Energi AS

Norwegian University of Science and Technology
Department of Electric Power Engineering

Preface

This master's thesis is the product of my final semester at the Department of Electric Power Engineering, Norwegian University of Science and Technology (NTNU). The work is a continuation of the specialization project completed in the fall of 2017, titled *"Converter Control for Harmonic Compensation in Microgrid Applications"*.

The thesis is carried out as a part of FME CINELDI, a research project lead by SINTEF Energy Research in collaboration with NTNU to develop the smart grid of the future. The work is encompassed by work package 4, microgrids.

An important remark is that the thesis was supposed to contain experimental as well as simulation results. Due to postponed delivery of necessary equipment, and a tight schedule for the existing equipment, obtaining experimental results in the available time frame, i.e. one semester, was not feasible. However, the model has been made with the intent of using it to obtain experimental results.

Trondheim, 11.06.2018

Ruben Buchmann

Acknowledgements

I would like to thank my supervisors, comprising Team Mexico. That is, prof. Olimpo Anaya-Lara and research scientist Raymundo E. Torres-Olguin. They have given me the possibility to learn a lot this past year about the exciting field of microgrids, as well as provided me with helpful proofreading. Thank you. In addition, a sincere thanks goes to guest research scientist Javier Roldan-Pérez at SINTEF Energy Research, whose crucial advice made the thesis realizable in the set time frame.

Moreover, the extensive help and open door of the excellent Fredrik T. B. W. Göthner has been of immense value. Thank you $e^{\pi^{\tau}}$ times.

It must also be acknowledged that many cookies have been consumed in office E-422, together with Anders, Maren, Knut and Sondre. It has been a great year. Thank you.

Lastly, I would like to thank the most important grid in my life, namely my girlfriend, In*grid*, for her moral support, patience and ability to make me laugh during stressful times.

Abstract

The world is critically dependent on a transition from fossil fuels to renewable energy. Microgrids represent a promising systematic approach to increasing the reliability of the power system and solving the challenge of integrating intermittent renewable energy sources into the existing grid.

Several renewable energy sources, such as wind and photovoltaic, utilize power electronic converters, representing distinctly different characteristics compared to the technology used in the conventional power system of today. Among several traits, the converter's inherent ability to compensate harmonics is a cost-effective solution to meet the persistent challenge of harmonic distortion, which is a typical power quality issue in microgrids. However, uneven line impedances between the converters and the PCC lead to imbalance between the harmonic currents supplied by the converters, potentially harming the converter supplying most of the harmonic load.

This master's thesis investigates a harmonic sharing scheme to meet the challenge of harmonic current sharing imbalance. A simple AC microgrid in island mode is developed, consisting of two converters, their individual LCL filters, uneven line impedances and one non-linear load. In addition, the control system of the microgrid's converters is developed and elaborated. It consists of primary control, including current, voltage and droop control, as well as control measures to achieve harmonic compensation of the capacitor voltage for both converters. This way, the issue of uneven harmonic current sharing is displayed, as the converter facing the lowest line impedance supplies the majority of the harmonic load. A virtual impedance-based harmonic sharing scheme is then implemented in the control system of the converter facing the lowest impedance, to achieve better sharing of the harmonic load. Specifically, the sharing of the 1st, 5th and 7th harmonic current component is studied.

The implemented harmonic sharing scheme is displayed with simulation results in a case study, proving the feasibility of the elaborated control system. The 5th and 7th harmonic currents are observed to be shared almost perfectly, while the fundamental current sharing is improved substantially, but still has a value of 0.033 p.u. in constant offset. This indicates the need for a secondary control layer in order to update the power references, thus achieving perfect fundamental current sharing. Additional key performance indicators (KPIs), namely apparent power, THD and load parameters, are simultaneously monitored to give a broad assessment of the harmonic sharing scheme. In this case, all KPIs are deemed adequate, resulting in assessing the harmonic sharing scheme as successful, but with room for improvement in terms of fundamental current sharing.

Three additional cases are displayed to evaluate the control system's resilience towards certain system alterations. The first of the three additional cases investigates harmonic compensation of the PCC voltage. Isolated, the scheme is successful, as the THD of the PCC voltage is lowered from 16.2% to 8.20%. However, the system as a whole is not compatible with this configuration, ending in inadequate performance of all other KPIs than the THD.

The second of the additional cases studies the effect of implementing opposite droop compared to a conventional droop scheme. The difference in system responses between the two implementations is observed to be marginally different, with the opposite droop delivering an improvement of fundamental harmonic current sharing. Specifically, opposite droop achieves a mismatch in fundamental current sharing of 0.013 p.u., compared to the corresponding number of 0.033 p.u. for the conventional droop.

The last of the additional cases simulates the connection of a linear load to the PCC. The harmonic sharing remains efficient, showing only a decrease in performance for the fundamental current component. However, the load experiences large ripples. E.g., the voltage has a ripple of approximately 131 V, constituting a suboptimal loading scenario. Hence, as a whole, the control system is not compatible with connecting an additional linear load between two phases.

Summarized, the harmonic sharing scheme proposed and developed demonstrates efficient harmonic sharing. However, it has been found that the proposed scheme may reduce its effectiveness when system conditions change substantially. Hence, recommendations for further work are provided which include enhancing robustness of the harmonic sharing approach.

Sammendrag

Verden er kritisk avhengig av en overgang fra fossil energi til fornybar energi. Mikronett representerer en lovende og systematisk tilnærming til å øke påliteligheten i kraftsystemet som helhet, samt å løse utfordringen med å integrere varierende fornybare energikilder inn i det eksisterende nettet.

Disse fornybare energikildene, slik som vind- og solkraft, er avhengig av kraftelektronikk, som representerer særegne egenskaper sammenliknet med teknologien som i hovedsak brukes i dagens kraftsystem. I dette henseendet har kraftomformeren flere fordeler, blant annet dens evne til kostnadseffektiv harmonisk kompensasjon. Denne egenskapen kan brukes til å møte utfordringen med harmonisk forvrengning i nettet, som er et typisk kraftkvalitetsproblem i mikronett. Hvis det er tilfelle at omformerne i mikronettet har forskjellig linjeimpedans mellom seg og PCC, vil de dele den harmoniske kompenseringen ulikt, som potensielt kan skade omformeren som forsyner majoriteten av den harmoniske lasten.

Denne masteroppgaven undersøker et harmonisk lastdelingssystem for å møte utfordringen med ujevn harmonic strømdeling. Et enkelt AC mikronett i øymodus blir utviklet, bestående av to omformere, deres individuelle LCL-filtre, ujevne linjeimpedanser og én ikke-lineær last. I tillegg blir reguleringssystemet til mikronettets omformere utviklet og utdypet. Reguleringssystemet består av primærkontroll, inkludert strøm-, spenning- og "droop"-kontroll, i tillegg til regulering av harmonisk kompensajon for begge omformerne. På denne måten blir problemet med ujevn harmonisk strømdeling vist, siden omformeren som har den laveste linjeimpedansen mellom seg og PCC vil forsyne majoriteten av den harmoniske lasten. Et virtuell impedansbasert harmonisk strømdelingsystem blir så implementert i kontrollsystemet til omformeren som møter den laveste linjeimpedansen, slik at bedre strømdeling kan bli oppnådd. Spesifikt blir delingen av den første, femte og syvende harmoniske strømkomponenten undersøkt.

Det implementerte strømdelingssystemet blir fremvist med simuleringsresultater i et casestudie som viser effektiviteten til det utdypede kontrollsystemet. I casen blir femte- og syvendekomponenten delt nært perfekt, mens delingen av fundamentalstrøm også forbedres betraktelig, men ender med en konstant ujevnhet i deling på 0.033 p.u.. I tillegg blir flere ytelseskriterier lagt til (KPIer), nærmere bestemt tilsynelatende effekt, total harmonisk forvrengning (THD) og lastparametre. Disse måles også for å gi en bredere evaluering av det harmoniske strømdelingssystemet. For denne casen blir alle KPIer ansett til å være tilstrekkelige, noe som resulterer i en godkjenning av strømdelingssystemet og kontrollsystemet som helhet. Dog må den fundamentale strømdelingen forbedres for at systemet skal fungere perfekt.

Tre ekstra caser blir undersøkt for å teste kontrollsystemets evne til å fungere ved et ut-

valg systemendringer. Den første av disse tre casene ser på harmonisk kompensasjon av PCC-spenningen. Ser man bare på THD-responsen fungerer systemet, i og med at THD blir målt til å synke fra 16.2% til 8.20%. Systemet som helhet fungerer dog ikke, da responsen til alle de tre andre KPIer blir ansett som for dårlige.

Den andre av de tre ekstra casene implementerer "opposite droop" i stedet for konvensjonell droop, som er tilfelle i de andre casene. Forskjellen i KPI-respons mellom et system med opposite droop og et med konvensjonell droop måles til å være marginal, men opposite droop oppnår noe bedre fundamental strømdeling. Spesifikt oppnår opposite droop en endelig ujevnhet på 0.013 p.u., mens konvensjonell droop oppnår 0.033 p.u., som nevnt over.

Den siste av de tre ekstra casene kobler en ekstra lineær last til PCC. Den harmoniske strømdelingen observeres til å fortsatt være effektiv, med kun en marginal forverring i deling av den fundamentale strømkomponenten. Dog opplever den ikke-lineære lasten store oscillasjoner i sine parametre. For eksempel måles spenningsoscillasjonen til å være 131 V, noe som representerer en suboptimal lastsituasjon. Dette vil si at systemet som helhet, slik det er nå, ikke er kompatibelt med en tilkobling av en ekstra ikke-lineær last.

Oppsummert så fungerer det harmoniske delingssystemet som blir lagt frem godt, med stort sett effektiv deling av de strømkomponentene som er studert. Dog synker effektiviteten når systemet blir utsatt for store endringer. Derfor inneholder avslutningsvis denne oppgaven forslag til videre arbeid som inkluderer å øke motstandsdyktigheten til strømdelingssystemet.

Contents

List of Figures

List of Tables

Abbreviations

2L-VSC	2-level Voltage Source Converter
CIGRÉ	The Council on Large Electric Systems
DER	Distributed Energy Resource
EMRF	Efficient Multiple Reference Frame
IEA	International Energy Agency
KCL	Kirchoff's Current Law
KPI	Key Performance Indicator
KVL	Kirchoff's Voltage Law
LPF	Low-Pass Filter
MSRF	Multiple Synchronous Reference Frame
PCC	Point of Common Coupling
PI	Proportional Integral
PLL	Phase-Locked Loop
PWM	Pulse-Width-Modulated
RMS	Root Mean Square
SHC	Selective Harmonic Compensation
THD	Total Harmonic Distortion
VSC	Voltage Source Converter

Chapter 1

Introduction

1.1 Background and Motivation

The International Energy Agency (IEA) states in their annual energy projections, the World Energy Outlook 2017, that the world will demand large amounts of energy in the years to come. Specifically, renewable energy will constitute the majority of the additions in net energy capacity, as depicted in Fig. 1.1.

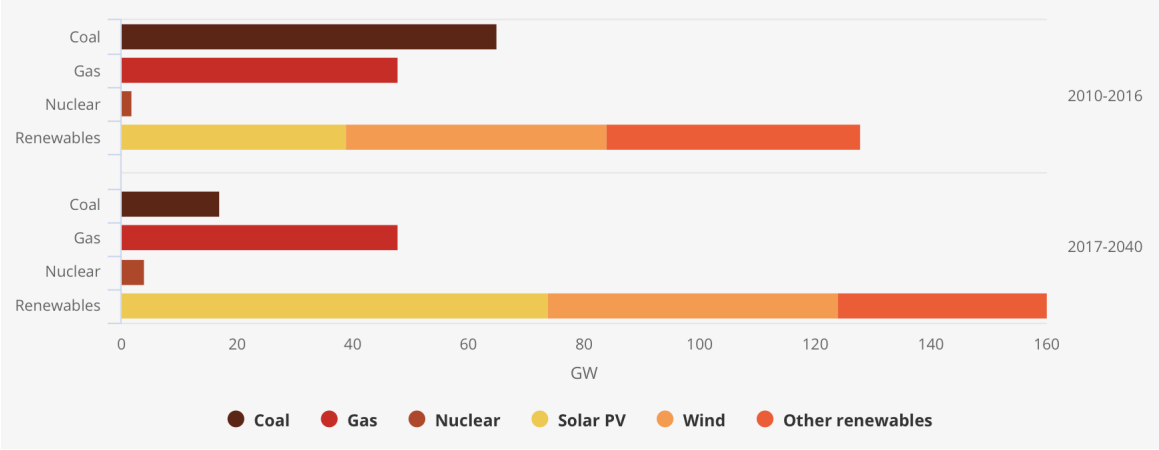

Figure 1.1: Global average annual net capacity additions by type [1].

Furthermore, inspecting Fig. 1.2, the amount of people without access to electricity is decreasing, but still above one billion, as of 2016. Sub-saharan Africa encompasses the majority of the electricity-less population, with India coming in second.

These statistics clearly present that the demand for renewable electricity is enormous, and that it will not decrease in the foreseeable future. It is also important to note that wind and photovoltaic (PV) power constitute the majority of the renewable energy capacity increase. The

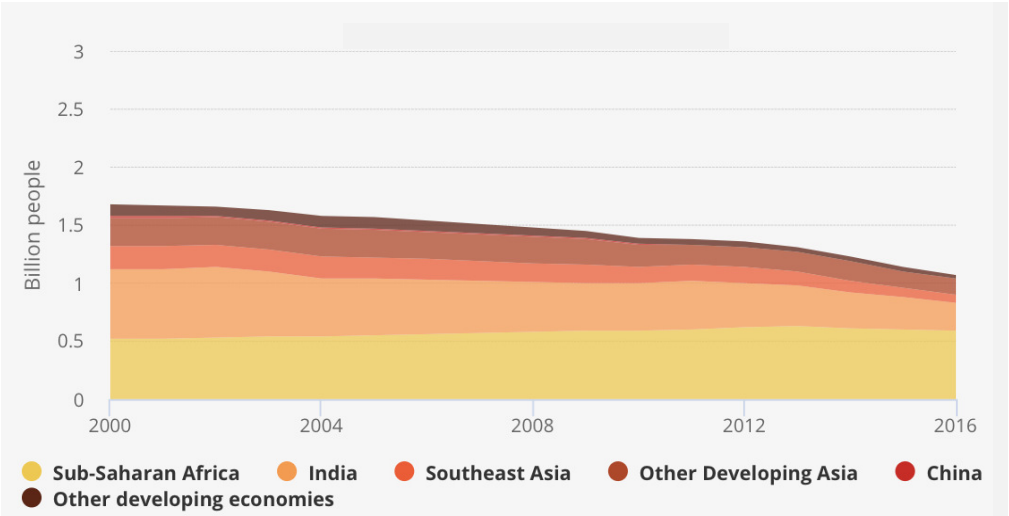

Figure 1.2: Amount of people without access to electricity [1].

technologies affiliated with these energy sources represent separate characteristics when compared to the synchronous generators comprising most conventional power systems of today.

Firstly, wind and PV power are dependent on power electronic interfaces. Moreover, their production is of an inherent intermittent nature, demanding auxiliary storage solutions to be flexible in order to meet the load demand. A promising and widely studied power system concept able to meet these challenges is the microgrid. A microgrid typically consists of energy sources, storage solution(s) and loads, and is connected to the main grid at one or several points. In addition, they can be operated in a controlled and coordinated manner [5]. Figure 1.3 depicts a typical microgrid. The internal voltage of the microgrid can be both AC and DC, and a microgrid operating disconnected from the main grid is termed to be in island mode. This is a fundamental characteristic of the microgrid, and represents a demanding situation in terms of stability, as the primary controllers directly regulate the voltage and frequency. For additional reading of the state-of-the-art of microgrids, the reader is advised to inspect the literature review provided in Appendix E, which was part of the specialization project mentioned in the preface.

Configuring a power system as a microgrid results in several benefits. These include:

1. Facilitating the implementation and use of renewable energy sources at their original location, which relieves the need for extensive transmission systems between the energy source and consumption, thus also reducing transmission line losses [6].

2. Providing ancillary services to the grid, and meanwhile improving the overall reliability of the power system by being able to disconnect during faults in the microgrid or in the main grid [7].

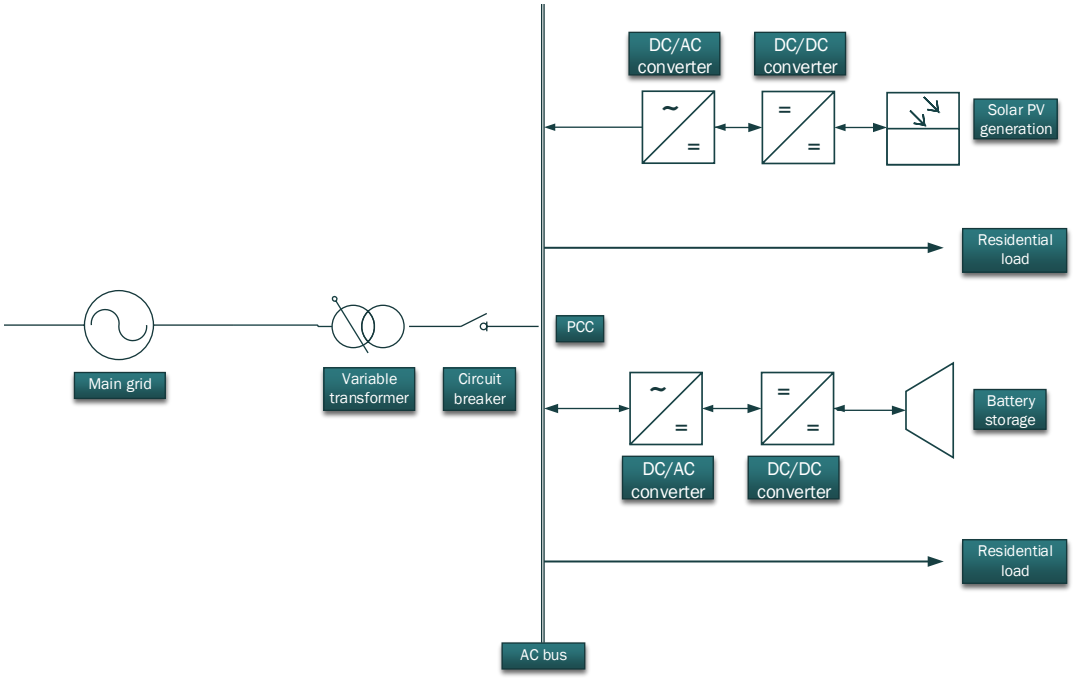

Figure 1.3: An illustration of a typical microgrid [2].

3. Interoperability, allowing frequent connection and disconnection of sources and loads while operating according to grid standards [4, 6].

4. Facilitating the use of flexible loads, allowing more precise matching of production and consumption. This increases the system efficiency and defers the need for grid reinforcements [8].

5. A cost-effective way to facilitate rural electrification, as no main power system is needed to operate the microgrid [7].

However, several challenges in microgrids must be addressed before their full potential is utilized. Central technical challenges found in the current literature consist of:

1. Designing a protection scheme capable of responding properly to both island and grid-connected mode. This constitutes a fundamental challenge, as the fault currents between the two modes of operations are significantly different [9].

2. Avoiding stability issues. The control systems in the microgrid may interfere, causing local oscillations. Moreover, seamless transition between grid-connected and island mode is

challenging in terms of stability [10].

3. Low inertia. As microgrids often consist of primarily inverter-interfaced generation, the inertia in the system is low compared to the conventional power system. This can lead to large frequency deviations in island mode [10].

4. Maintaining sufficient power quality [6]. With the increasing use of nonlinear loads in the distribution system, the presence of low-order current harmonics are becoming a concern, as these harmonics lead to voltage distortions [11].

A cost-effective way to meet the challenge elaborated in the last point, i.e. to provide harmonic compensation, is to use parts of the available power rating of the converters in the microgrid for compensation purposes [11]. However, the converters will share the load affiliated with this compensation unevenly according to the line impedance between the converters and the load. In turn, this may lead to overstressing the converter providing the majority of the compensation. To meet this challenge, a harmonic sharing scheme is introduced to share the harmonic currents evenly between the supplying converters. Developing, presenting and evaluating such a scheme constitutes the main goal of this thesis.

This introduction provides the motivation for the developed model and issues investigated in this master's thesis. The detailed objectives, methodology, main contributions and thesis outline follow in the subsequent sections.

1.2 Objectives

The objectives of this master's thesis are:

- To describe the simulated islanded microgrid model and all its components, including the reason behind the choice of their values, thus allowing subsequent reproduction of the model for both simulation and experimental purposes.

- To develop and elaborate the primary control, consisting of an inner current control loop, an outer voltage control loop, and droop control.

- To develop and elaborate the harmonic compensation scheme, including a method of extracting the value of individual harmonic components.

- To develop and elaborate the harmonic sharing scheme.

- To present simulation results verifying the applicability of the elaborated control system to achieve harmonic sharing.

- To present additional cases, including simulation results, investigating how different system changes affect the harmonic sharing scheme.

1.3 Methodology

- The development and elaboration of the microgrid are done by first introducing the entire structure, providing av overview. Then, each component is handled, introducing their function and value in the microgrid.

- The control system is developed and elaborated using methods obtained from the current literature, and used in recent, conventional research.

- The proposed microgrid and complementary control system is simulated using the MATLAB/Simulink environment. Hence, simulations results for the case studies are obtained. The simulations are run in discrete time with a fixed step time.

1.4 Main Contributions

This work is part of the research project FME CINELDI, which aims to provide an essential scientific effort to solve microgrid technology challenges. Hence, a meticulous effort has been made throughout this thesis to make the procedure as transparent as possible, allowing subsequent use in the research project. All parameters have been given, and a complete collection of them is displayed in Chapter 5. This has been done to ensure correct reproduction of the simulation model.

Several system configuration properties representing novelty have been identified, together comprising a combination seemingly underinvestigated in todays literature. However, the microgrid presented is not of unrealistic nature, rather, it could very well be of practical importance. The identified configuration properties are:

1. **High ratings of the converters.** Most of the papers examined test converters rated in the range of 1-10 kVA. The converters of this thesis are 60 kVA.

2. **Line impedances with R/X ratio equal to 1.43.** This ratio is only slightly predominantly resistive. This gives no clear coupling between electrical quantities, making the droop control less straightforward.

3. **Additional testing of the harmonic sharing scheme.** Most of the papers examined that propose a novel harmonic sharing scheme tests the scheme for one particular load situation. In this thesis, several cases are added to further evaluate the feasibility of the harmonic sharing scheme.

4. **Relatively high line impedances.** However, they are still within reasonable values according to CIGRÉ.

Point number four might constitute the most interesting point, as a non-linear current flowing through a line impedance leads to voltage distortion. When the current and the line impedance are high, the fundamental and harmonic voltage drops across the line impedance are substantial. In turn, this leads to severe issues at the Point of Common Coupling (PCC) with regards to power quality, as the voltage might be lower than allowed and contain substantial harmonic distortion. It seems little or no work has been done on the field of harmonic sharing where all the listed points are present, increasing the value of the results acquired in this thesis.

1.5 Structure of the Report

The thesis is organized as follows:
Chapter 2 presents the model of the microgrid used throughout the thesis. The model is described component by component, along with relevant background theory and reasons behind the chosen parameter values.
Chapter 3 elaborates the primary control, consisting of an inner current control loop, and outer voltage control loop and droop control. Essential background theory is provided, along with parameter values and tuning procedures.
Chapter 4 elaborates the outer layers of the control, namely the harmonic compensation and harmonic sharing schemes.
Chapter 5 presents the simulations results for the different cases along with their complementary discussion.
Chapter 6 draws the final conclusion made from the simulation results obtained.
Chapter 7 lists possibilities for future work.
Appendix A provides supporting material.

Appendix B elaborates the per unit system.
Appendix C contains an example of the MATLAB code used in conjunction with the Simulink model.
Appendix D contains Simulink model diagrams.
Appendix E contains an overview of the state-of-the-art of microgrids. The text is an excerpt from the specialization project written in the fall of 2017.

Chapter 2

System Description

This chapter describes the microgrid system investigated in this thesis. This is done by first presenting an overview of the system, introducing the different components. In the subsequent sections, every component is elaborated, presenting their values and the reason behind the choice of these values. Note that all values mentioned are collected in a Table 5.1 in Chapter 5.

2.1 Overview

The power system investigated in this thesis is an AC microgrid, depicted in Fig. 2.1. Two voltage source converters (VSCs) are observed, VSC_1 and VSC_2. The DC side of the VSCs is modeled as a constant voltage source, while the AC side is connected to the PCC via their respective LCL filters and line impedances.

R_{L1} and L_1 are the parasitic resistance and inductance of the LCL filter's converter side inductor, respectively. Furthermore, C denotes the filter capacitor, and R_{L2} and L_2 are the parasitic resistance and inductance of the LCL filter's grid side inductor, respectively. Observe that the filter values are identical for both filters. Moreover, the line impedance connecting converter 1 to the PCC are termed R_{Line_1} and L_{Line_1}, and the line impedance connecting converter 2 to the PCC are termed R_{Line_2} and L_{Line_2}. The non-linear load consists of a connecting inductor, L_L, a diode rectifier, a smoothing load capacitor, C_L and a resistive load, R_L.

The microgrid has a simple structure in terms of containing few elements. Limiting the size of the structure is a deliberate choice, mainly based on three factors:

1. Decreasing the size decreases the complexity, allowing a more thorough explanation of the approach taken in the thesis.

2. The chosen configuration, i.e. two converters supplying one load, is a common setup seen in current literature, e.g. in [12, 13, 14, 15]. Being able to compare the results obtained in this thesis with literature is valuable, as it helps assess the feasibility and degree of success of the results.

3. The results obtained can be easily extended towards a more complicated microgrid.

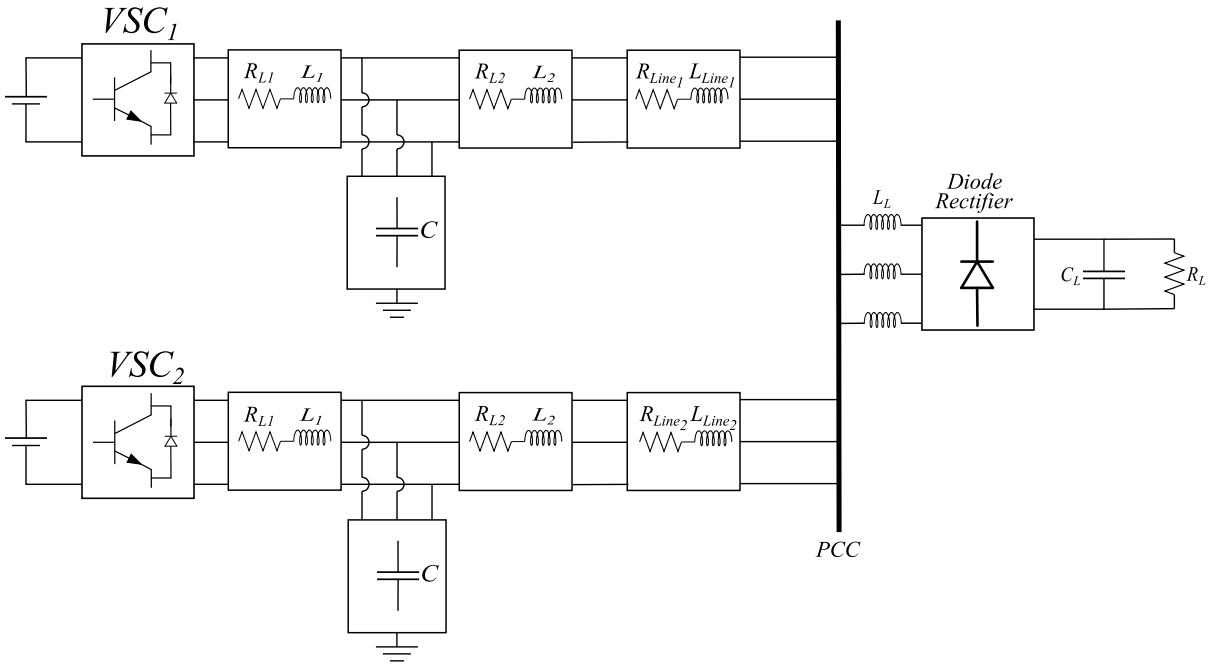

Figure 2.1: Illustration of the microgrid investigated in this thesis.

Furthermore, the microgrid is assumed to be operating in island mode, and issues related to feasibility in grid-connected mode are regarded as beyond the scope of the thesis. Without elaborating further, it can be noted that the use of a grid synchronizing scheme, e.g. a phase-locked loop (PLL), and different control objectives are notable differences between island and grid-connected mode.

The DC-side of the converters, represented by a constant voltage source, are assumed to be connected to an arbitrary power source, e.g. wind, solar or battery, or a combination of these. An important presumption is that the converters have specific power ratings, but the energy supply is not a limiting factor. The omission of an energy limit is a simplification, but does not degrade the results, as the evaluation of the harmonic sharing scheme is unaffected by unconstrained power conditions.

Also, note that the system is a three-wire system, i.e. there is no neutral wire present. The grounding associated with the filter capacitor establishes the voltage reference point.

2.2 Voltage Source Converter

The 2-level voltage source converter (2L-VSC) is used as the VSCs in the system. An example of this type of VSC is depicted in Fig. 2.2. In the figure, $v_{DC,inv}$ is the DC side voltage, maintained by the assumed ideal power source. The three converter legs consist of two switches, each of them coupled with antiparallel diodes. v_{LL}^{abc} is the line to line voltage output, set to 400 V. i_i^{abc} is the three-phase inverter line current.

The rating of the converters are 60 kVA each, and they are capable of switching frequencies in the range of 0-6000 kHz.

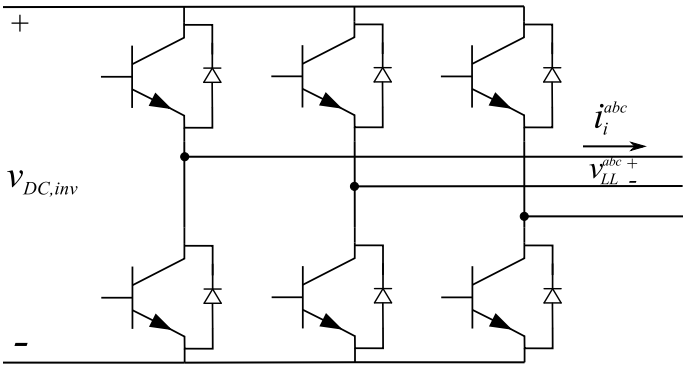

Figure 2.2: A detailed view of the VSC.

The type of VSC presented here is ubiquitous in the literature [7, 16], but the main reason for choosing this topology is the fact that it represents the available hardware to obtain experimental results in the proposed subsequent work.

2.2.1 Modeling the VSC in Simulink

The VSC utilizes a pulse-width-modulated (PWM) switching scheme, comparing a triangular carrier waveform with a desired sinusoidal waveform [17]. Implementing this in a simulation program, such as Simulink, implies limiting the simulation time step to the switching frequency. Naturally, this limitation extends the length of time domain simulations.

A way to decrease simulation time, while still maintaining sufficient converter dynamic accuracy, is using an *averaged model* as a VSC. This is used throughout this thesis, with a simulation time step of 50 μs. This time step is sufficiently small to provide valid results, also when using the averaged model of the VSC.

2.3 LCL Filter

As a natural consequence of the transistor switching, all converters will to some degree produce waveforms containing higher-order harmonics. To address this challenge, a passive filter at the output of the converter is often installed. It works as a low-pass filter, attenuating the higher-order harmonics.

The simplest filter in use is an inductor, i.e. an L filter [18]. However, LC or LCL filter topologies are more common, as they prove to be more efficient in terms of attenuation and cost [18]. The LC filter will provide an attenuation of 40 dB/decade after the cutoff frequency, while the LCL filter will provide 60 dB/decade [19]. To illustrate these characteristics, they can be observed in the Bode plot depicted in Fig. 2.3. The transfer functions of the different filters can be found in App. A.1.

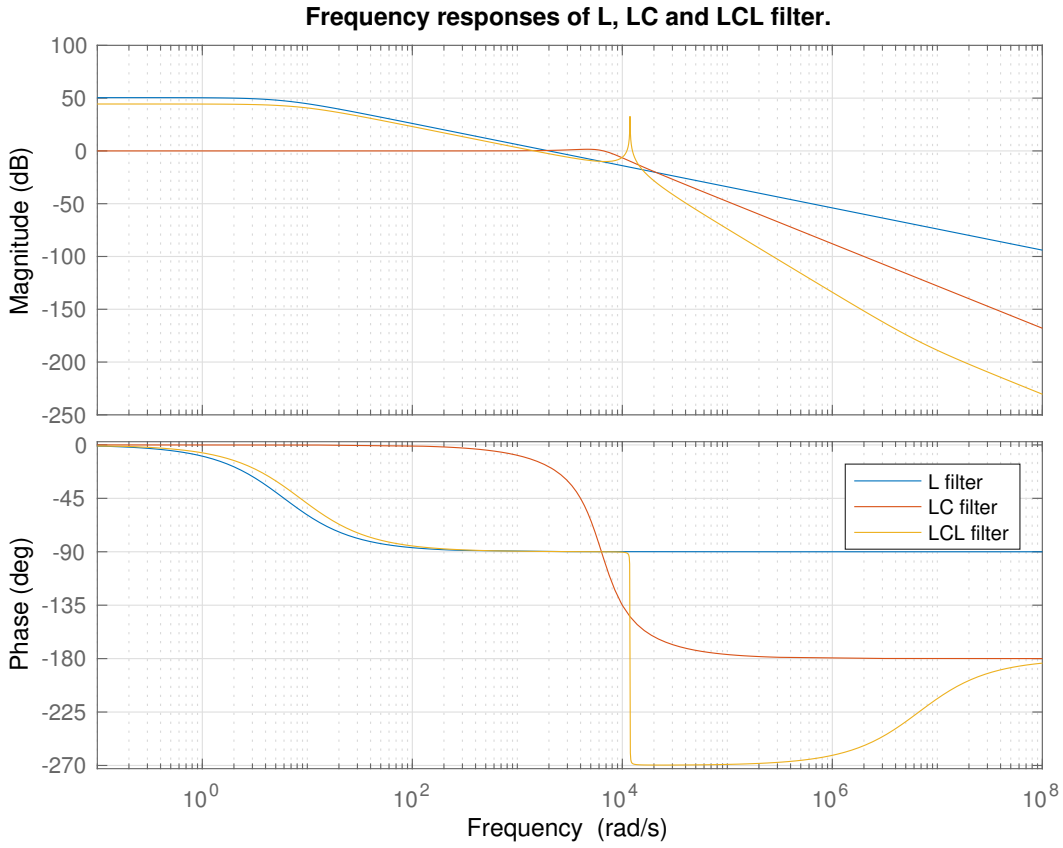

Figure 2.3: Frequency responses of L, LC and LCL filter.

One of the objectives of this thesis is to allow later comparison of acquired simulations results with experimental results. Hence, the LCL filter values of this simulation model should be iden-

tical to the ones used in the laboratory. The LCL filter available for experimental testing has constant inductor and capacitor values, while the parasitic resistances of the inductor are taken from [20], which is an inductor data sheet. These resistances are in the same order of magnitude as the ones in the lab. The LCL filter values can be observed in Table 2.1.

Table 2.1: LCL filter values

Parameter	L_1	R_{L_1}	C	L_2	R_{L_2}
Value	500 μ H	6 mΩ	50 μF	200 μH	0.8 mΩ
Value p.u.	0.0589	0.0023	0.0419	0.0236	0.0003

Resonant frequencies are present between L_1 and C, and L_2 and C. These are generally calculated according to Eq. 2.1:

$$\begin{aligned} \omega L &= \frac{1}{\omega C} \\ \implies f_{res} &= \frac{1}{2\pi\sqrt{LC}} \end{aligned} \tag{2.1}$$

For the parameter values given in Table 2.1, the resonant frequencies become:

$$\begin{aligned} f_{L_1C} &\approx 1592\ Hz \\ f_{L_2C} &\approx 1007\ Hz \end{aligned} \tag{2.2}$$

Inspecting the calculated resonant frequencies, it is important to note two observations:

1. The resonant frequencies are not close to the switching frequency, which is set to be 6 kHz in order to ensure that switching frequency harmonics are attenuated.

2. The resonant frequencies are also not close to the highest harmonic order which is compensated in the system, i.e. the 7th harmonic (350 Hz). Similarly, this avoids amplifying the low-order harmonics being compensated.

2.4 Line Impedance

To determine line impedance values which could be present in actual microgrids, and hence improve the fidelity of the obtained results, Table 2.2 is used as reference. It depicts typical line impedance values for different voltage levels, taken from [4].

The table shows the high R/X ratio present in low voltage grids, i.e. the values are valid for low voltage microgrids. However, lower X/R ratios also do occur: In [21], The Council on Large

Table 2.2: Typical line impedance values for different voltage levels [4].

Type of Line	**R [Ω/km]**	**[Ω/km]**	**R/X ratio**
Low voltage line	0.642	0.083	7.7
Medium voltage line	0.161	0.190	0.85
High voltage line	0.06	0.191	0.31

Electric Systems (CIGRÉ) presents a benchmark model with various types of lines eligible for use in microgrids. One of the line types listed by CIGRÉ is chosen as the line in this thesis due to its R/X ratio being close to 1. i.e., not dominantly resistive or inductive. The line is an overhead type with aluminium conductors, with a size of 4·50 mm^2. Per phase impedance values corresponding to 800 meter line of this type is given in Table 2.3, where R_{Line} and X_{Line} is the line resistance and inductance, respectively.

Table 2.3: Initial per phase line impedance values of the model microgrid.

R_{Line}**[Ω]**	R_{Line} **p.u.**	X_{Line}**[Ω]**	X_{Line} **p.u.**	**R/X ratio**
0.3176	0.1191	0.2232	0.0837	1.423

As stated in the objectives, the particular R/X ratio of the line is identified as one of the key points increasing the novelty in the results acquired in Chapter 5. Moreover, the line impedance affects the harmonic sharing to a great extent. When the line impedances in a microgrid are identical, the converters share the harmonic load equally. However, when this is not the case, and if no measures are implemented, the harmonic sharing will become uneven between the present converters. This scenario might lead to overstressing of the converter(s) providing the highest load, which in turn increases the chance of decreased lifetime or malfunction [14].

Uneven line impedances constitute the simulation base case described in Section 5.4. Hence, the line impedances connecting each converter to the PCC are chosen to be uneven. More explicitly, Z_{Line_2} is assigned the impedance values found in Table 2.3, while Z_{Line_1} *is chosen to be 1.5 times larger than* Z_{Line_2}. This results in the line impedance values found in Table 2.4.

Table 2.4: Per phase line impedance values of the line connecting converter 1 to the PCC.

R_{Line_1}**[Ω]**	R_{Line_1} **p.u.**	X_{Line_1}**[Ω]**	X_{Line_1} **p.u.**	**R/X ratio**
0.4764	0.1787	0.3348	0.1256	1.423

2.4.1 Line Impedance Effect on Stability

Through preliminary simulations, the system stability was observed to be dependant on the line impedance. The effect can be seen in Fig. 2.4, showing the p.u. voltage at the LCL filter output for one phase, v_{o_a}, when all other parameters are held constant. The system quickly becomes unstable when the line impedance corresponds to 600 meter line, as shown in Fig. 2.4a, while it is stable for the 800 meter line presented in the previous section, as shown in Fig. 2.4b. The reason for the instability is that when the line impedance decreases, both converters will try to control the PCC voltage.

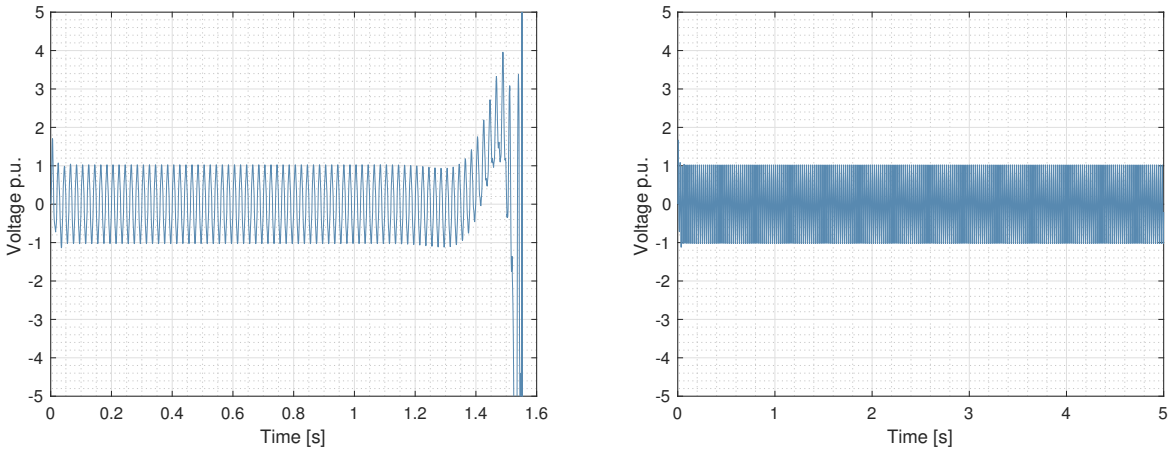

(a) v_{o_a} with Z_{line} corresponding to 600 meter line. (b) v_{o_a} with Z_{line} corresponding to 800 meter line.

Figure 2.4: A comparison of line impedances displaying stability sensitivity.

Two important consequences of the high line impedances are:

1. Increased voltage distortion at the PCC. The voltage distortion at the PCC is proportional to the size of the line impedance. This facilitates the interest to investigate the possiblity of compensating the PCC voltage instead of the capacitor voltage. This is investigated in case 2, which is founc in Section 5.6.

2. A substantial line voltage drop. The voltage drop across the line impedance is proportional to the line current and line impedance, according to Ohm's law. If both of these quantities are substantial, the voltage drop will also be substantial. This might result in a PCC voltage below its regulated limits of ±10% of RMS [22]. A way to compensate for this is to increase the voltage reference in the droop controller. This is implemented in the base case, Section 5.4, and used for all other cases.

2.5 Non-Linear Load

The non-linear load is a central part of the system setup, as it constitutes the source of the low-order harmonics penetrating the system. The load implemented in this thesis can be observed in Fig. 2.1. It consists of a three-phase, six-pulse, full bridge diode rectifier applying DC voltage to a load, represented by a resistor, R_L. A smoothing capacitor, C_L, is also present to decrease the ripple of the DC voltage delivered to the load. In addition, inductors, L_L, are installed between the rectifier and the PCC, which is a conventional practice to avoid direct connection between the load capacitor and the PCC [23]. The values of the load parameters are given in Table 2.5. Note that the value of L_L is found in [20], while the two other components are elaborated in the subsequent subsections.

Table 2.5: Load Parameters

Parameter	Symbol	Value
Load side inductor	L_L	120 μH
Load capacitor	C_L	1500 μC
Load resistance	R_L	2.92 Ω

The harmonic spectrum of the current corresponding to this kind of load contains harmonics of orders k = 6n $\pm$1, where n is a positive integer [24]. The current drawn by the load, together with its characteristic harmonic spectrum, can be seen in Fig. 2.5. It can be observed in Fig. 2.5a that the current waveform is indeed distorted, and that the harmonics present in Fig. 2.5b are of the orders expected. The 5th harmonic constitutes the most prominent order, with the other harmonics decreasing in amplitude as their order increases.

The THD of the load current is 23.1% and thus clearly distorted. This distorted current drawn from the non-linear load will lead to a distorted voltage waveform at the PCC. Furthermore, a distorted voltage at the PCC implies degraded power quality for auxiliary equipment connected to this point. Negative consequences for this equipment include overheating, malfunctioning, additional eddy current losses, communication system interference and tripping of sensitive equipment [25]. Hence, it is desireable to decrease the voltage distortion at the PCC as much as possible. Case 2 in Section 5.6 investigates if this is possible with the control system and model elaborated in this thesis.

2.5.1 Choosing the Value of the Load Capacitor

The value of the capacitance particularly affects two factors in the system:

1. The power factor. The charging of the capacitor represents a reactive power flow, worsening the power factor.

2. The peak-to-peak voltage ripple of the load voltage. Loads will tolerate different levels of voltage ripple, depending on their sensitivity.

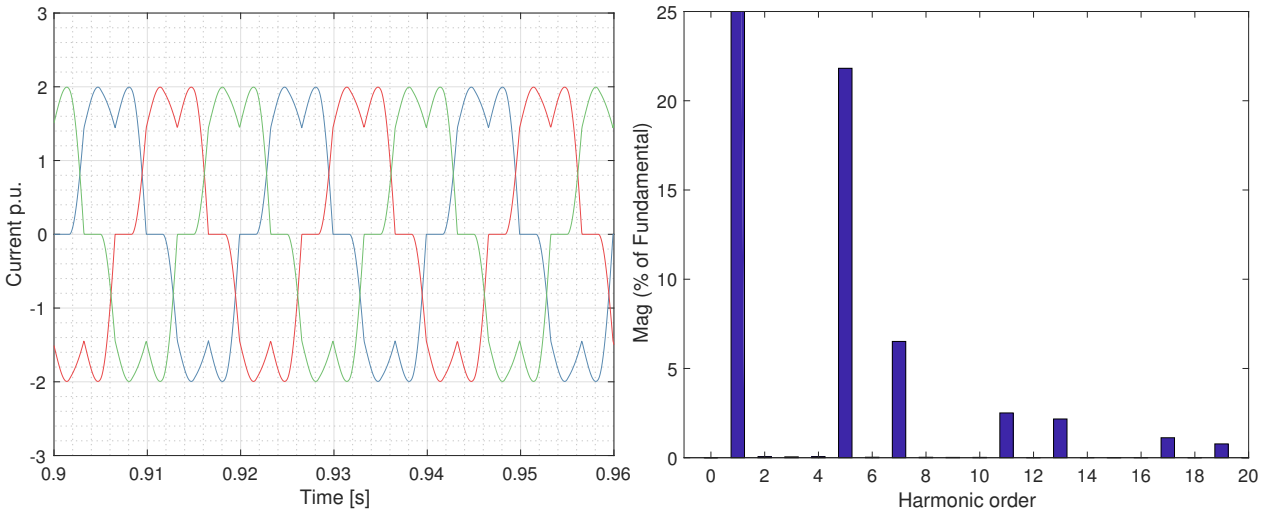

(a) The current drawn by the non-linear load.

(b) The harmonic spectrum of the load current.

Figure 2.5: The load current and its harmonic spectrum.

Power factor will worsen and voltage ripple will decrease as the capacitor value increases [17]. Hence, choosing the capacitor value is a trade-off between the two. In this thesis, the choice was made to focus on delivering sufficient voltage quality to the load, i.e. minimizing the voltage ripple to a certain extent. Thus, the effect on power factor is not quantified. Though investigating the effect of installing power factor correction measures would be interesting, it is considered outside the scope of this thesis.

The rectified voltage equation is gathered from [17] and shown in Eq. 2.3. In the equation, v_{DC} denotes the DC load voltage and v_{LL} is the line to line voltage of the AC side of the diode rectifier. In this case, this is the line to line PCC voltage.

$$v_{DC} = \frac{3}{\pi}\sqrt{2}v_{LL} \approx 1.35 v_{LL} = 540\ V \tag{2.3}$$

Limiting the peak-to-peak DC voltage ripple to 5%, i.e. 27 Volt, the capacitor value is found in Eq. 2.4. i_C is the time dependent capacitor current, I_c the RMS capacitor current, v_c the capacitor

voltage, and Δv_c is the voltage ripple allowed.

$$\begin{aligned} & i_c = C\frac{dv_c}{dt} \\ \implies & C = \frac{I_c t}{\Delta v_c}, \quad t = \frac{1}{50\,Hz \cdot 6}, \quad I_c \approx 12\,A \\ & C \approx 1500\,\mu F \end{aligned} \tag{2.4}$$

Note that I_c is approximated through visually inspecting the simulated capacitor current.

2.5.2 Modeling the Load Resistor in Simulink

Modeling the non-liner load of the microgrid is a non-trivial task. Most loads are sensitive to voltage, current and power fluctuations. Consequently, to keep fidelity, a goal is to decrease these fluctuations.

Through preliminary simulations, several resistor modelling alternatives were tested in Simulink to investigate their differences. These alternatives include constant power, constant current and constant impedance. However, none of these modelling alternatives contain any form of mechanism to maintain its input parameters. Hence, the final choice of the load is a purely resistive load modelled as a constant impedance, present in current literature [26, 27]. Specifically, it is a "series R load" Simulink block, given the settings which are shown in Eq. 2.5.

$$\begin{aligned} v_{DC} = 1.35 \cdot v_{LL} = 540\,V \\ P_{DC} = 100\,kW \end{aligned} \tag{2.5}$$

The Simulink block then calculates a constant resistance using the formula shown in Eq. 2.6. Thus, R_L denotes the load resistance equivalent to the values given in Eq. 2.5.

$$R_L = \frac{v_{DC}^2}{P_{DC}} = 2.92\,\Omega \tag{2.6}$$

Observing varying electrical load parameters during preliminary simulations results in an interest of monitoring these parameters in the case studies. A complete overview of the used key performance indicators are given in Section 5.2.

Chapter 3

Primary Control

In this chapter, the primary control of the converter is developed. Section 3.1 introduces the entire primary control structure, describing all components, while Section 3.2 provides essential background theory about the reference frame and controller utilized. Sections 3.3 and 3.4 elaborates the current and voltage control, and their design procedures, respectively. Lastly, Section 3.5 describes the droop control including the determination of its coefficients.

3.1 Introduction

The cascaded control structure of the primary control can be seen in Fig. 3.1. C_i, C_v and C_d denote the open loop transfer functions for current, voltage and droop control, respectively. Furthermore, i_i, v_c and i_o is the inverter input current, the capacitor voltage, and the converter output current, respectively. v_M is the modulator signal going into the VSC. e_c and e_v are the error inputs of the current and voltage control, respectively. P_1 and Q_1 represent the calculated fundamental active and reactive power, respectively, while v_c^* and ω_1 is the voltage and frequency references of the voltage control loop.

In general, the inverter input current, i_i, is controlled via the primary current control loop, while the outer voltage control loop controls the capacitor voltage, v_c. The frequency and voltage reference of the voltage control is received by the the droop control. From a control point of view the structure implies that the grid side inductor, L_2, is regarded as a part of the line impedance.

Note that the converters in the system are termed as voltage-controlled, allowing more direct voltage support, suitable for islanding microgrids [11]. Moreover, it is the voltage-controlled operation that enables the use of droop control for decentralized power sharing [27].

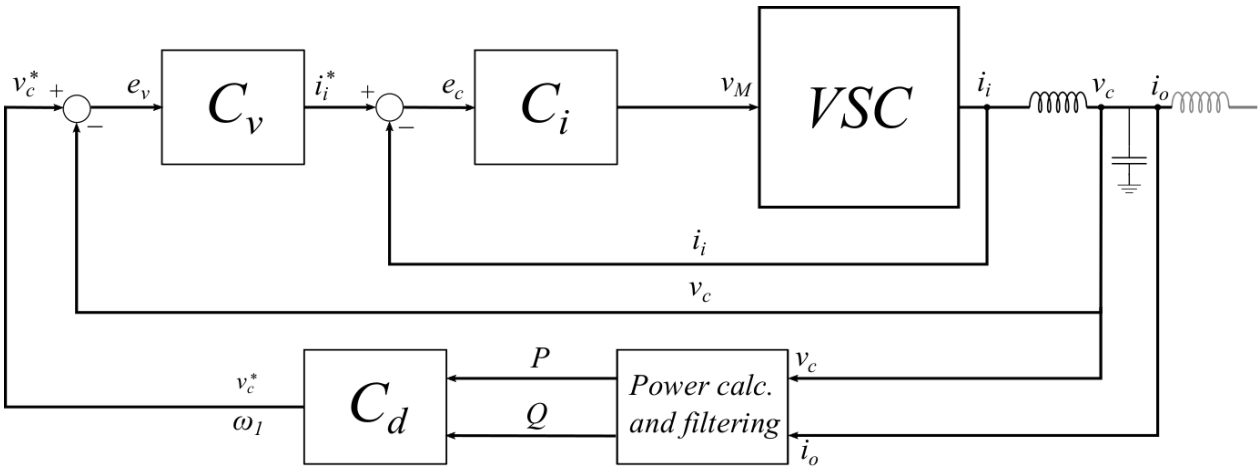

Figure 3.1: The cascaded control structure of the primary control loops.

3.2 Control in the Synchronous Reference Frame

This section provides essential background theory about the reference frame and controller used in the control system.

3.2.1 Reference Frames

Control of a three-phase VSC is usually done in either the stationary ($\alpha\beta$) or the synchronous (dq) reference frame [4], where both of them represent individual advantages and disadvantages. A visual comparison of the three reference frames is shown in Fig. 3.2, where the natural reference frame (abc) is included for comparison. It is observed that both reference frames have orthogonal axes, but the dq-frame rotates with a given angular velocity, ω.

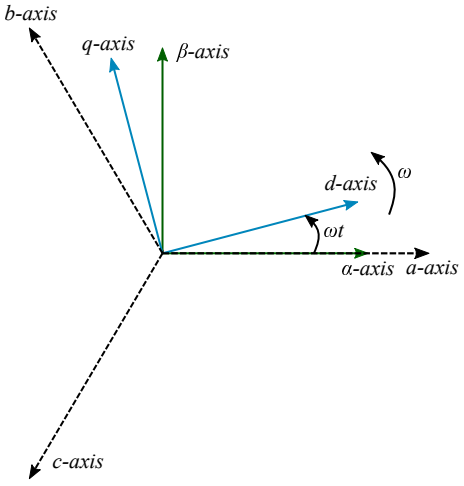

Figure 3.2: A comparison of the three conventional reference frames used for VSC control.

Mathematical transformations are used to achieve the adaptation between the reference frames, where the Park transformation is utilized to enable the transition between abc and dq [28]. The amplitude-invariant version of the Park transformation is shown in Eq. 3.1 :

$$\begin{bmatrix} d \\ q \\ 0 \end{bmatrix} = \underbrace{\frac{2}{3}\begin{bmatrix} cos(\theta) & cos(\theta - \frac{2\pi}{3} & cos(\theta + \frac{2\pi}{3} \\ -sin(\theta) & -sin(\theta - \frac{2\pi}{3}) & -sin(+\frac{2\pi}{3}) \\ \frac{1}{2} & \frac{1}{2} & \frac{1}{2} \end{bmatrix}}_{\text{Park transformation}} \begin{bmatrix} a \\ b \\ c \end{bmatrix} \tag{3.1}$$

In this thesis, the Park transformation and its inverse are used extensively, both in primary control, harmonic compensation and harmonic sharing. The essence of the transformation is that by rotating with the fundamental angular velocity of the natural reference frame, the fundamental d and q quantities of the synchronous reference frame become constant. Also, it is noted that the 0-component usually can be ignored for the configuration used in this thesis [29]. Furthermore, the constant nature of the d and q component enables several possibilities, e.g. the use of PI controllers, discussed in the next subection.

3.2.2 Proportional Integral Controllers

The linear proportional integral (PI) controller is widely used in industry and research to provide tracking of a given reference, often current or voltage. Two equivalent versions of its transfer function in the Laplace domain is shown in Eq. 3.2.

$$G_{PI}(s) = K_p \cdot \frac{1 + T_i s}{T_i s} = K_p + \frac{K_i}{s} \tag{3.2}$$

The proportional part (K_p) adjusts the amplitude of the frequency response, while the integral part provides an infinite gain at zero frequency. The latter characteristic enables the PI controller to yield suppression of steady-state errors for DC systems. This makes this controller suitable for use in conjunction with the synchronous reference frame.

However, when the reference signal deviates from a purely DC signal, steady-state errors are introduced. Moreover, the PI controller does not eliminate distortion. Nonetheless, PI control is widely used, and is also the controller used for both primary current and voltage control in this thesis, as well as in the harmonic compensation scheme elaborated in Chapter 4.

3.3 Primary Current Control

A single phase representation of the VSC and LCL filter can be seen in Fig. 3.3, where v_i^{abc} is the inverter output voltage, i_i^{abc} the inverter output current, and v_c^{abc} is the capacitor voltage.

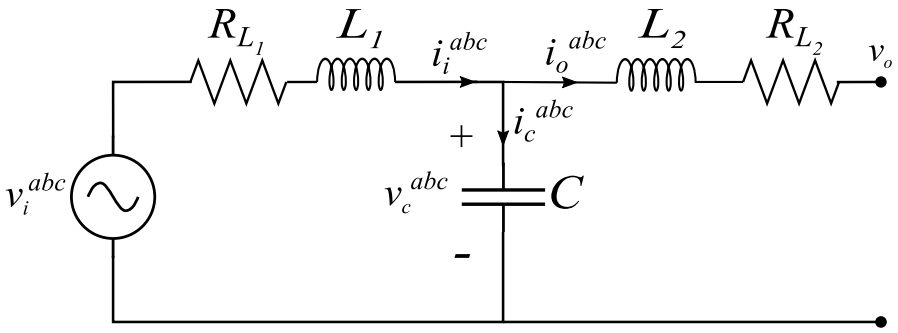

Figure 3.3: Single phase representation of voltage source and LCL filter.

Primary current control, also referred to as inner current control, regulates the current running through L_1 and R_{L_1}, namely i_i^{abc}. Inspecting Fig. 3.3, the following equation is deduced by applying Kirchoff's voltage law (KVL) :

$$\begin{aligned} v_i^{abc} &= v_{L_1}^{abc} + v_{R_{L_1}}^{abc} + v_c^{abc} \\ \implies v_i^{abc} &= L_1 \frac{d i_i^{abc}}{dt} + R_{L_1} i_i^{abc} + v_c^{abc} \end{aligned} \tag{3.3}$$

The Park transformation is then used to transform the equation from abc to dq quantities. A more elaborate explanation of the procedure is found in App. A.2. In addition, the parameters are transformed to their per unit equivalent according to App. B. These algorithms yield:

$$i_{i,pu}^d = \left(v_{i,pu}^d - v_{c,pu}^d + \omega_{pu} L_{1,pu} i_{i,pu}^q \right) \left(\frac{\frac{\omega_{Base}}{L_{1,pu}}}{s + \frac{R_{L1,pu}\omega_{Base}}{L_{1,pu}}} \right) \tag{3.4a}$$

$$i_{i,pu}^q = \left(v_{i,pu}^q - v_{c,pu}^q - \omega_{pu} L_{1,pu} i_{i,pu}^d \right) \left(\frac{\frac{\omega_{Base}}{L_{1,pu}}}{s + \frac{R_{L1,pu}\omega_{Base}}{L_{1,pu}}} \right) \tag{3.4b}$$

Inspecting Eq. 3.4a and b, the coupling between the d and q axis is evident. A way to mitigate this issue is implementing decoupling measures, which improves control performance in terms of dynamic response [30]. In addition, the converter represents a computational delay equating to [31]:

$$T_c = \frac{1}{2} T_{sw} \tag{3.5}$$

where T_{sw} is the switching time. A block diagram of the PI controller, decoupling measures, delay and the electrical system is depicted in Fig. 3.4.

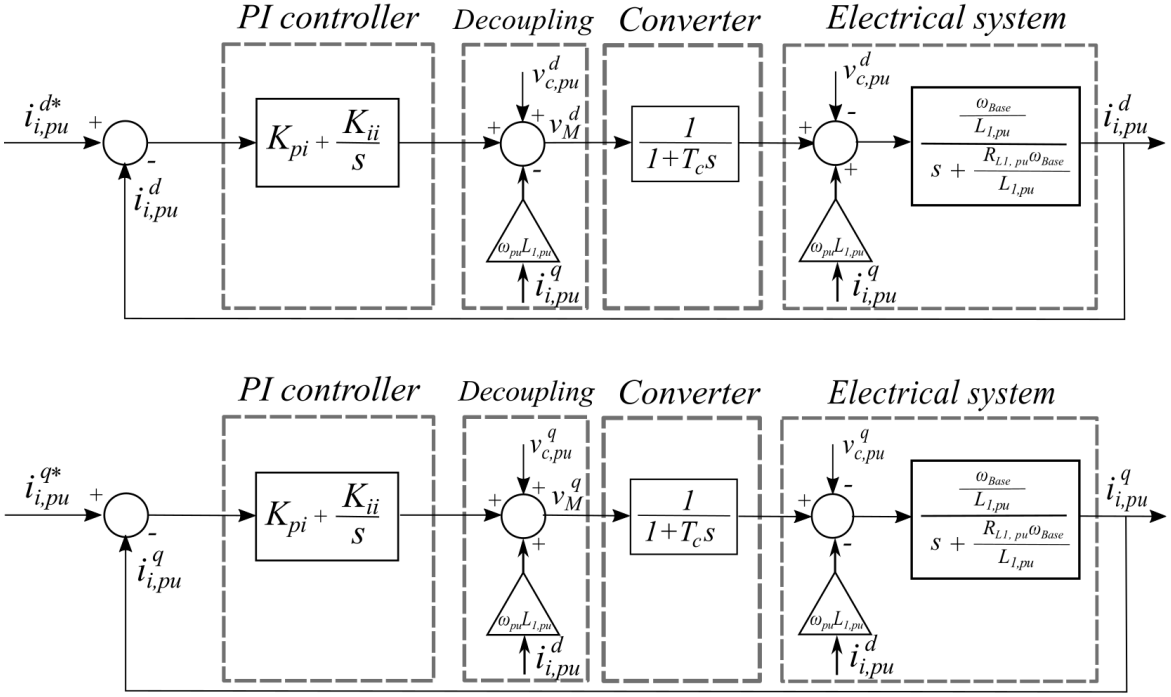

Figure 3.4: Block diagram of the primary current control.

Perfect decoupling is assumed. In addition, as the transfer function of the d and q axis are the same, there is no need to distinguish between them. A general open loop transfer function is thus:

$$G_{OL}(s) = \underbrace{\left(K_{pi} + \frac{K_{ii}}{s}\right)}_{\text{PI controller}} \cdot \underbrace{\frac{\frac{w_{Base}}{L_{1,pu}}}{s + \frac{R_{L1,pu}\omega_{Base}}{L_{1,pu}}}}_{\text{system}} \cdot \underbrace{\frac{1}{sT_c + 1}}_{\text{delay}} \tag{3.6}$$

Using Eq. 3.6, the tuning procedure can be elaborated in the following subsection.

3.3.1 Tuning of the Primary Current Control Parameters

The tuning of the control parameters of the primary current control is done via the method of pole placement, a conventional algorithm explained in [32]. An elaboration is given below.

The converter delay is omitted for tuning purposes, as it represents a very small time constant. An approximation of the system in the Laplace domain is then given by:

$$\begin{aligned} H_c(s) &= \frac{c}{s+a} = \frac{\frac{\omega_{Base}}{L_{pu}}}{s+\frac{R_{pu}\omega_{Base}}{L_{pu}}} \\ \implies c &= \frac{\omega_{Base}}{L_{pu}}, \quad a = \frac{R_{pu}\omega_{Base}}{L_{pu}} \end{aligned} \tag{3.7}$$

To acquire control parameter values, the standard second order characteristic polynomial equation is used, as given in Eq. 3.8.

$$D(s) = s^2 + 2\rho\omega_{oc}s + \omega_{oc} \tag{3.8}$$

where ρ determines the damping ratio and ω_{oc} determines the bandwidth. A conventional rule of thumb is to set this bandwidth a decade lower than the switching frequency. This allows a necessary bandwidth between the current controller and the switching frequency, as the response naturally cannot be faster than the physical switching. Still, having a high current control bandwidth is desireable to achieve the quickest response feasible. Furthermore, to determine the controller parameters, the closed loop response is developed as follows.

$$G_{OL_c}(s) = \left(K_{pi} + \frac{K_{ii}}{s}\right)\left(\frac{c}{s+a}\right), \quad G_{CL}(s) = \frac{G_{OL}(s)}{1+G_{OL}} \tag{3.9a}$$

$$\implies G_{CL_c}(s) = \frac{K_p c s + K_i c}{s^2 + s(a + K_p c) + K_i c} \tag{3.9b}$$

Comparing Eq. 3.8 and the denominator of Eq. 3.9b, K_{pi} and K_{ii} become:

$$\begin{aligned} K_{pi} &= \frac{2\rho\omega_{oc} - a}{c} \\ K_{ii} &= \frac{\omega_{oc}}{c} \end{aligned} \tag{3.10}$$

Choosing $\rho_i = 1.1$ to get a well damped response [32], $\omega_c = \frac{2\pi f_{sw}}{10}$, and inserting for the filter values found in Table 2.1, the current control parameters become:

$$\begin{aligned} K_{pi} &= 1.125 \\ K_{ii} &= 1930 \end{aligned} \tag{3.11}$$

The gain and phase margins of the open loop response are shown in Fig. 3.5 to verify the feasibility of the tuning. Note that the bode plot depicts the frequency response of the open loop

transfer function of Eq. 3.6, i.e. the delay is included. A rule of thumb for the margins is 6 dB and 45° for the gain and phase margin, respectively [33]. The gain margin is infinite, as the phase response is never below 180°. Furthermore, the phase margin is 45.6°. Hence, the rule of thumb for both margins are found to be satisfied with the given tuning.

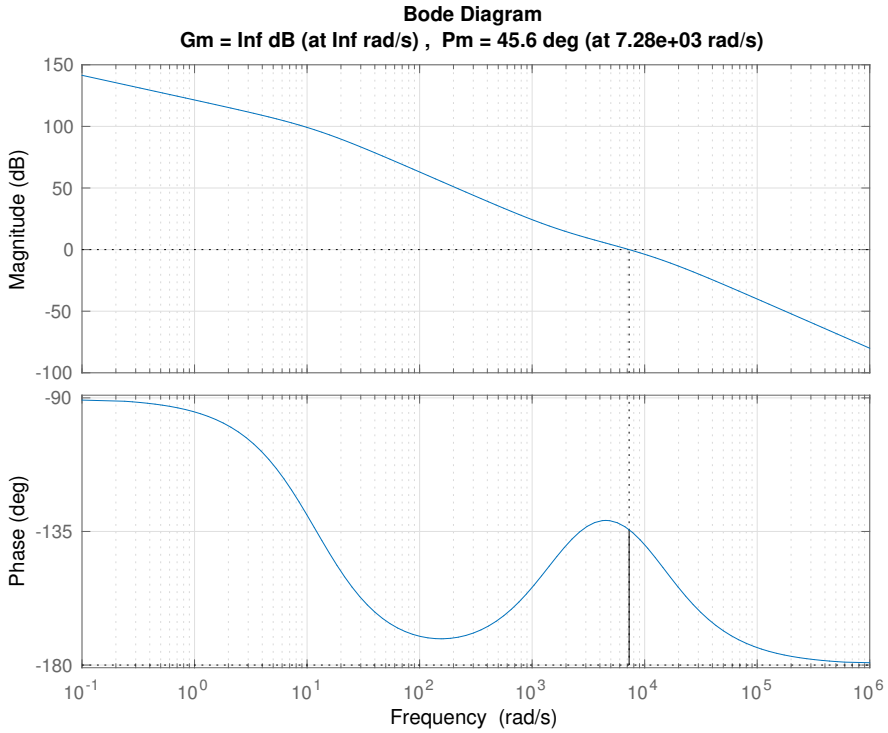

Figure 3.5: Gain margin (Gm) and phase margin (Pm) of the open loop current control response.

3.4 Primary Voltage Control

The primary voltage control of the converters aims to control the capacitor voltage, v_c, thereby establishing the voltage and frequency of the system. This control loop is slower than the current control, allowing the current control to respond to fast transients. This relieves the voltage of unnecessary voltage spikes. In addition, having a difference in response speed between the current and voltage control is necessary to decouple them.

By inspecting Fig. 3.3, Eq. 3.12 can be derived from Kirchoff's current law (KCL) :

$$i_i^{abc} = i_o^{abc} + i_c^{abc} \tag{3.12}$$

Similarly to what was done in primary current control, the Park transformation is used to trans-

form Eq. 3.12 from abc to dq. A more elaborate explanation of the procedure is found in App. A.3. In addition, the parameters are transformed to their per unit equivalent according to App. B. These algorithms yield:

$$v_{c,pu}^{d} = \left(i_{i,pu}^{d} - i_{o,pu}^{d} + v_{c,pu}^{q}\omega_{pu}C_{pu}\right)\left(\frac{\omega_{Base}}{sC_{pu}}\right) \tag{3.13a}$$

$$v_{c,pu}^{q} = \left(i_{i,pu}^{q} - i_{o,pu}^{q} - v_{c,pu}^{d}\omega_{pu}C_{pu}\right)\left(\frac{\omega_{Base}}{sC_{pu}}\right) \tag{3.13b}$$

In a similar manner as in primary current control, decoupling of the d and q axes is implemented. Moreover, the current control loop represents a delay for the voltage control. This delay can be approximated to a first order low-pass filter (LPF) with a time constant corresponding to the current control bandwidth:

$$T_{eq} = \frac{1}{\omega_{oc}} \tag{3.14}$$

Consequently, the primary voltage control, decoupling measures, delay and electrical system to be controlled are depicted in Fig. 3.6.

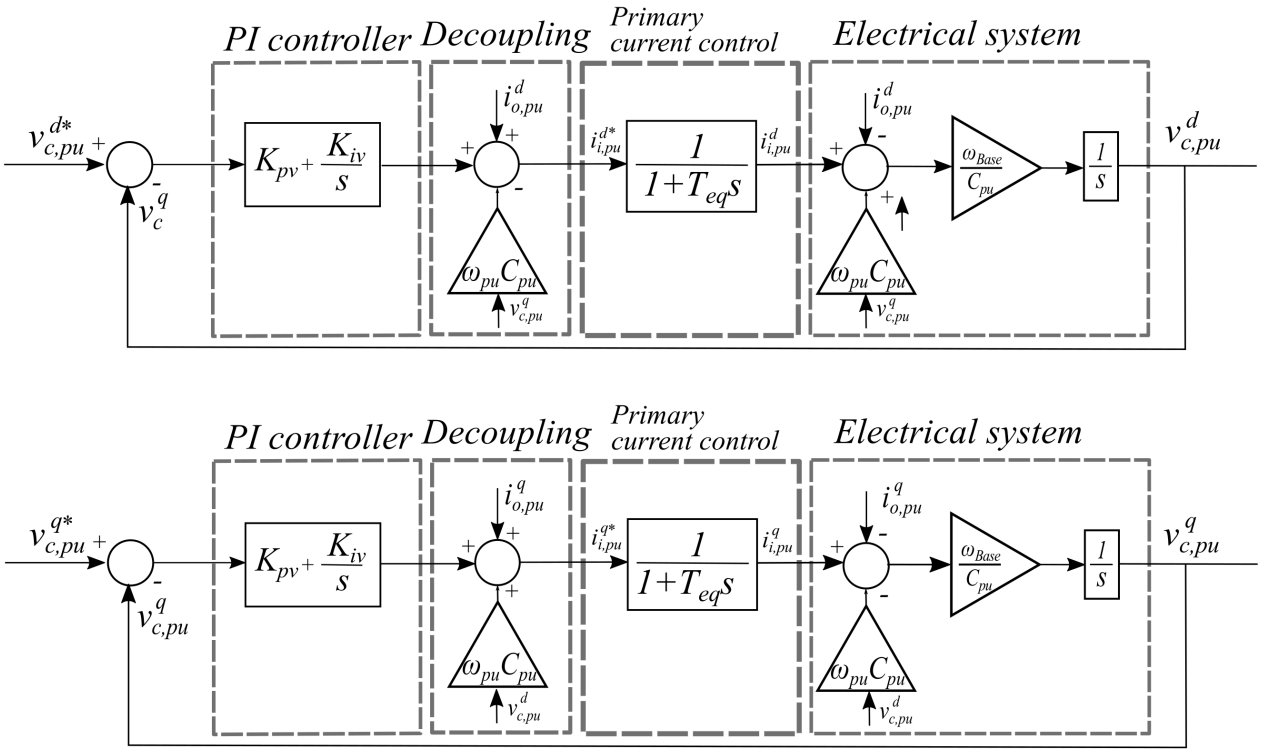

Figure 3.6: Block diagram of the primary voltage control.

Perfect decoupling is assumed. In addition, as the transfer function of the d and q axis are the same, there is no need to distinguish between them. A general open loop transfer function for the voltage control is thus:

$$G_{OL}(s) = \underbrace{\left(K_{pv} + \frac{K_{iv}}{s}\right)}_{\text{PI controller}} \cdot \underbrace{\frac{\omega_{Base}}{C_{pu}s}}_{\text{system}} \cdot \underbrace{\frac{1}{T_{eq}s+1}}_{\text{inner loop}} \tag{3.15}$$

Using Eq. 3.15, the tuning procedure can be elaborated in the following subsection.

3.4.1 Tuning of the Primary Voltage Control Parameters

The voltage controller parameters are tuned in an identical manner as the current controller, with the main difference between the two being the system transfer function. Moreover, the delay represented by the current control loop is omitted during tuning. This is due to T_{eq} being relatively small compared to the time constant of the voltage loop.

An approximation of the system in the Laplace domain becomes:

$$\begin{aligned} H_v(s) = \frac{b}{s} = \frac{1}{Cs} = \frac{1}{\frac{C_{pu}}{\omega_{Base}}s} \\ \implies b = \frac{\omega_{Base}}{C_{pu}} \end{aligned} \tag{3.16}$$

Developing the closed loop response:

$$G_{OL_v}(s) = \left(K_{pv} + \frac{K_{iv}}{s}\right)\left(\frac{b}{s}\right), \quad G_{CL}(s) = \frac{G_{OL}(s)}{1+G_{OL}} \tag{3.17a}$$

$$\implies G_{CL_v}(s) = \frac{sbK_{pv} + K_{iv}b}{s^2 + sbK_{pv} + K_{iv}b} \tag{3.17b}$$

Comparing Eq. 3.8 and the denominator of Eq. 3.17b, K_{pv} and K_{iv} become:

$$\begin{aligned} K_{pv} = \frac{2\rho\omega_{ov}}{b} \\ K_{iv} = \frac{\omega_{ov}}{b} \end{aligned} \tag{3.18}$$

The bandwidth of the voltage control is typically chosen a decade lower than the current control bandwidth. This is done to decouple the two control loops.

Hence, choosing $\omega_{ov} = \frac{\omega_{oc}}{10}$, $\rho_v = \rho_i = 1.1$, and inserting for filter values found in Table 2.1, the voltage control parameters become:

$$K_{pv} = 0.1388$$
$$K_{iv} = 26.16 \tag{3.19}$$

The gain and phase margins corresponding to the voltage control loop, including delay, can be seen in Fig. 3.7. The gain and phase margins are infinite and 64.7°, respectively. As for the current control, these margins are within the rule of thumb set by [33].

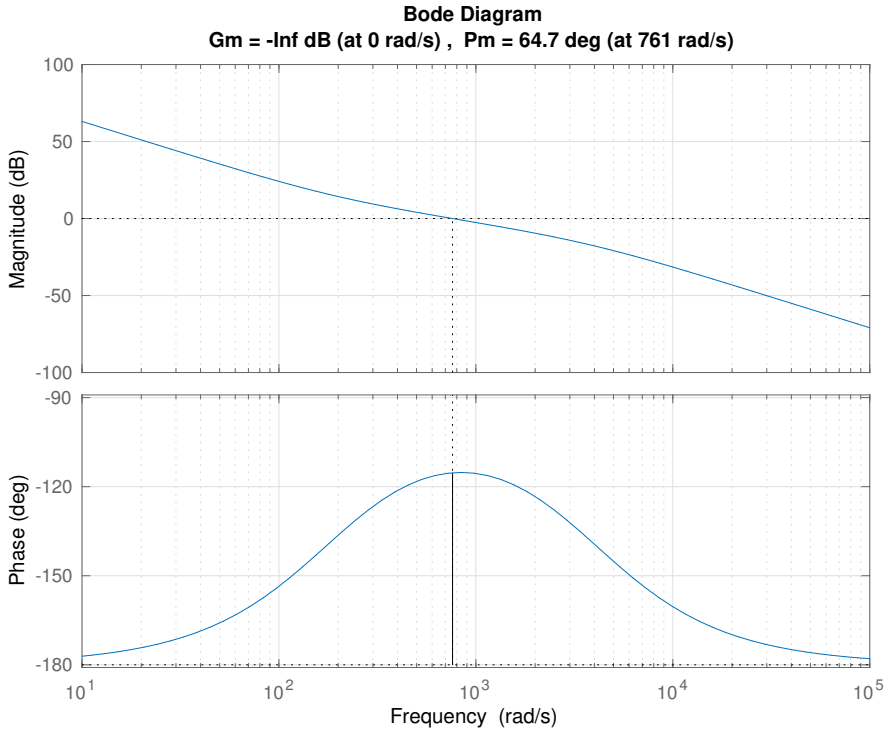

Figure 3.7: Gain margin (Gm) and phase margin (Pm) of the open loop voltage control response.

3.5 Droop Control

The Distributed Energy Resources (DERs), i.e. production units, of a microgrid need to be coordinated in a proper manner to establish optimal power sharing between them. This is conventionally done in either a centralized or decentralized manner. In short, the centralized approach involves close proximity of the inverters and high-bandwidth communication [4]. However, in a microgrid, generators and loads might be separated by several kilometers, indicating the increased aptitude of a decentralized approach.

The far most applied decentralized technique is based on droop control. This concept can

be viewed as virtual inertia, imitating the real inertia of the synchronous generators, which comprise the foundation of the conventional power system. The principle of the primary response of the conventional power system involves balancing power at the loss or gain of system frequency [10]. This characteristic also forms the basis of conventional droop control, which includes power-frequency (P-f) droop, and reactive power-voltage (Q-V) droop. The characteristic droop equations are given in Eq. 3.20, and illustrated in Fig. 3.8. For the P-f droop, ω and ω_{ref} are the system frequency and system frequency reference, respectively. m_i is the P-f droop coefficient, while P_1 and P_{ref} are the measured fundamental active power and active power reference, respectively. For the Q-V droop, V and V_{ref} are the capacitor voltage and capacitor voltage reference, respectively. n_i is the Q-V droop coefficient, while Q_1 and Q_{ref} are the measured fundamental reactive power and reactive power reference, respectively.

$$\begin{aligned} \omega &= \omega_{ref} - m_i(P_1 - P_{ref}) \\ V &= V_{ref} - n_i(Q_1 - Q_{ref}) \end{aligned} \tag{3.20}$$

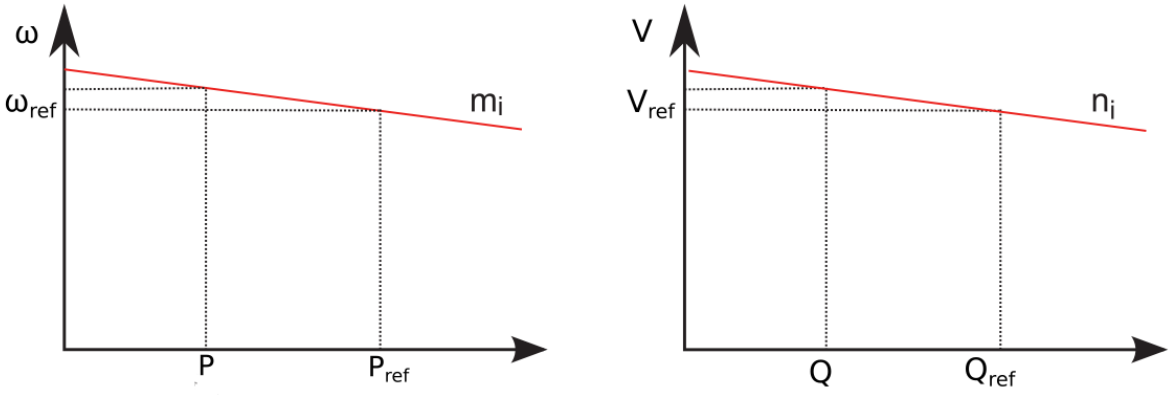

Figure 3.8: Characteristic graphs of conventional droop control, adapted from [3].

However, conventional droop is based on the fact that high voltage lines have a low R/X ratio, as was shown in Table 2.2 in Section 2.4. This characteristic gives the P-f and Q-V coupling. Low voltage grids, on the other hand, generally have high R/X ratio. A way to alter the droop control to be compatible with this type of grid is by use of "opposite droop", where the power-voltage (P-V) and reactive power-frequency (Q-f) couplings are utilized. This yields the following equations:

$$\begin{aligned} V &= V_{ref} - m_i(P_1 - P_{ref}) \\ \omega &= \omega_{ref} + n_i(Q_1 - Q_{ref}) \end{aligned} \tag{3.21}$$

Investigating how the opposite droop affects the performance of the harmonic sharing is of interest, as the R/X ratio of the line impedances used in simulations are 1.43. This was shown in Section 2.4. Hence, opposite droop is implemented in case 3 in Section 5.7.

Whether conventional or opposite droop is utilized, determining the variables of the droop equations is a significant task. The determination of the different variables is dealt with in the following subsections.

3.5.1 Power Calculations

The power delivered from the converters, P and Q, are calculated by using the measurements of i_o and v_c. However, these quantities contain harmonics. Therefore, the calculated power is low-pass-filtered to obtain the fundamental power components, P_1 and Q_1, used in the droop control. Fig. 3.9 shows the scheme.

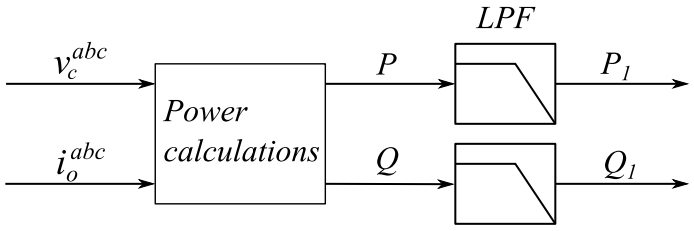

Figure 3.9: The power calculation and filtering scheme.

In order to decouple the droop control from the primary control loop, the low-pass-filters are tuned to be slower than the voltage loop. Simultaneously, the droop response cannot be too slow. Through simulations, a suitable bandwidth and corresponding time constant is found:

$$\omega_d = 10\,rad/s \tag{3.22a}$$

$$T_d = 0.1\,s \tag{3.22b}$$

3.5.2 Determining Active and Reactive Power References

Microgrid control is often divided into several control layers, namely primary, secondary and tertiary control [10]. This scheme is often referred to as hierarchical control. In this thesis, only issues related to primary control is considered. However, a task of the secondary control layer is to provide the active and reactive power references, P_{ref} and Q_{ref}, to the droop control. This is often done with the help of low bandwidth communication infrastructure [34].

P_{ref} and Q_{ref} would then be updated according to the power flow in the microgrid. When no secondary control layer is present, these references must be set manually. For the simulations performed in this thesis, the following procedure has been executed to set the references:

1. Adjust P_{ref} and Q_{ref} to a level where each converter approximately delivers its rated apparent power, 60 kVA.
2. Observe the system response.
3. If the system is stable and the converters approximately deliver their rated power, keep the power references. If not, adjust the references and repeat point 2.

This procedure resulted in the following power references:

$$\begin{aligned} P_{ref} &= 50\ kW \\ Q_{ref} &= 22\ kVAr \\ \implies S_{conv} &= \sqrt{P_{ref}^2 + Q_{ref}^2} \approx 59.2\ kVA \end{aligned} \tag{3.23}$$

3.5.3 Tuning of Droop Coefficiencts

The converters of a microgrid should be controlled to share the total load of the system in proportion to their respective power rating. This implies that the droop coefficients of converter i, n_i and m_i, are inversely proportional to the power rating of their respective converter [35]. Hence, the droop coefficients should satisfy:

$$n_1 S_1 = n_2 S_2 = ... = n_n S_n \tag{3.24a}$$

$$m_1 S_1 = m_2 S_2 = ... = m_n S_n \tag{3.24b}$$

Since the power ratings of the two converters are identical (60 kVA), the droop coefficients of the converters are also identical:

$$n_1 = n_2 = n \tag{3.25a}$$

$$m_1 = m_2 = m \tag{3.25b}$$

Nonetheless, determining the value of the droop coefficients, namely n and m, is a non-trivial task. The system's stability margin decreases with droop coefficient increase until instability

occurs [36]. To choose optimal droop coefficient values requires a dynamic model of the entire microgrid, which is a comprehensive task and defined as outside the scope of this thesis.

Hence, the droop coefficients have been chosen according to the following relation, found in e.g. [37]:

$$n = \frac{\omega_{max} - \omega_{min}}{P_{max}} = \frac{\Delta\omega}{P_{max}} \tag{3.26a}$$

$$m = \frac{V_{c,max} - V_{c,min}}{Q_{max}} = \frac{\Delta V_c}{Q_{max}} \tag{3.26b}$$

Allowing a deviation of 1% and 10% for frequency and voltage, respectively, yields the following coefficients:

$$n = \frac{\Delta\omega}{P_{max}} = \frac{0.01 \cdot \omega_1}{50000} = 6.28 \cdot 10^{-5} \tag{3.27a}$$

$$m = \frac{\Delta V_c}{Q_{max}} = \frac{0.1 \cdot V_{Base}}{30000} = 1.28 \cdot 10^{-3} \tag{3.27b}$$

The droop control elaboration ends the chapter of primary control. The control measures in this chapter do not compensate or share harmonics inherently. This gives the foundation for the next chapter, which elaborates the harmonic compensation and sharing scheme used in this thesis, together with the essential background theory.

Chapter 4

Harmonic Compensation and Sharing Schemes

This chapter explores the later utilized schemes of harmonic compensation and sharing. In particular, Section 4.1 sets the chosen schemes in perspective by comparing them with other methods in their respective fields. Furthermore, Section 4.2 presents background theory, including theory about harmonics, sequence characteristics, the harmonic extraction technique utilized and virtual impedance. In 4.3, the harmonic compensation scheme is elaborated, while 4.4 presents the harmonic sharing scheme. Finally, Section 4.5 concludes the chapter by providing an overview of the complete control structure used to obtain simulation results in Chapter 5.

4.1 Introduction

The traditional way to limit harmonics in a power system is by the use of passive or active filters [11]. However, these filters represent an additional cost for the utility. A cost-effective way to meet this challenge is by using the available power rating of the power electronic interfaces in the microgrid for harmonic compensation purposes [11].

Two common schemes for harmonic compensation are either by the use of PR controllers in the $\alpha\beta$-frame or PI controllers in the dq-frame [10]. In the PR-based scheme, PR controllers in the form of band-pass filters are tuned to the desired harmonic frequency to be mitigated [38]. In this way, all other frequencies are attenuated, allowing the tracking of the desired harmonic frequency to zero. In the PI-based scheme, the Park transformation together with low-pass filtering are exploited to extract the amplitude of the desired harmonic frequency. This frequency can then be tracked to zero by the use of PI controllers [39]. The latter method is used in this

thesis, and elaborated in Section 4.3.

If mismatched line impedances are present in the grid, the harmonic compensation load will be shared unevenly. A harmonic sharing mechanism must thus be implemented to allow the harmonic load to be shared evenly. The use of virtual impedance to achieve harmonic sharing is ubiquitous in the literature [16, 40, 14, 15, 41, 42, 13], as the virtual impedance allows shaping of the control output impedance. In this way, the line impedances can be compensated to be equal, resulting in even harmonic sharing. In the field of virtual impedance used for harmonic sharing, a variety of different solutions have been published in the literature. Among these are harmonic droop [14], adaptive virtual impedance [41], resistive-capacitive virtual impedance [13] and resistive-inductive virtual impedance [42]. The last method is implemented in this model, and hence elaborated in an individual section, namely Section 4.4.

4.2 Selected Background Theory

This section gives the basic concept to interprete harmonics, as well as introduce the sequence characteristics of harmonics. Furthermore, the utilized harmonic extraction technique is elaborated. Finally, the concept of virtual impedance is introduced and discussed.

4.2.1 Harmonics and Total Harmonic Distortion

A non-linear load will draw a distorted current waveform. Basic Fourier analysis states that a periodic nonsinusoidal waveform $f(t)$, such as distorted current, can be decomposed into its fundamental and harmonic components [17]:

$$i_s(t) = i_{s1}(t) + \sum_{h \neq 1} i_{sh}(t) \tag{4.1}$$

The total amount of distortion in the current or voltage waveform can be quantified by the index named total harmonic distortion (THD) [17]. Taking current as an example, the formula for THD is shown in Eq. 4.2:

$$THD = 100 \cdot \sqrt{\sum_{h \neq 1} \left(\frac{I_{sh}}{I_{s1}} \right)^2} \tag{4.2}$$

Eq. 4.2 implies that a THD of zero means a waveform only consisting of the fundamental harmonic, while a non-zero value of THD implies the presence of additional harmonic components in the waveform. Thus, the definition allows the THD value to exceed 100%. Note that THD will

be the primary measurement of harmonic distortion throughout this thesis.

4.2.2 Sequence Characteristics of Harmonics

The sequence characteristics of harmonics is not a conspicuous feature, but is of eminent nature for the schemes of both harmonic compensation and sharing used in this thesis. Therefore, an overview of the phenomenon follows.

Imbalance in a three-phase system can be represented by a combination of positive, negative and zero sequence components. Similarly, the different harmonic orders can be categorized in sequences by their rotation relative to the fundamental component's rotation [23]. A selection of harmonics, their sequence and their rotation relative to the fundamental component is given in Table 4.1.

Table 4.1: Sequence and rotation characteristics for a selection of harmonic orders.

Type of sequence	**Harmonic order**			**Rotation**
Positive	1st	7th	13th	With fundamental
Negative	5th	11th	17th	Against fundamental
Zero	3rd	9th	15th	No rotation

Recall that the 5th and 7th harmonic are the harmonic orders to be compensated and shared in this work. Furthermore, it is observed that these harmonics have different sequence characteristics. This is taken into account in the harmonic extraction technique elaborated in the next subsection.

4.2.3 Multiple Synchronous Reference Frames

Multiple synchronous reference frames (MSRFs) are used to extract the amplitude of a selected harmonic component in a given electrical quantity, e.g. current or voltage [40]. The scheme goes by several other names, e.g. harmonic synchronous reference frames [29] and multiple reference frames [39]. Similarly to what is done for the fundamental component, the Park transformation is utilized. The difference in an MSRF-context is that the angle input to the transformation corresponds to one specific harmonic order. Hence the name of the method, which indicates the use of several synchronous reference frames, namely one for each harmonic order. A more thorough explanation of the harmonic extraction procedure, based on [43], is given below.

In a balanced three-phase system, the periodically varying phase values can be represented by a single rotating vector, as shown in Fig. 4.1.

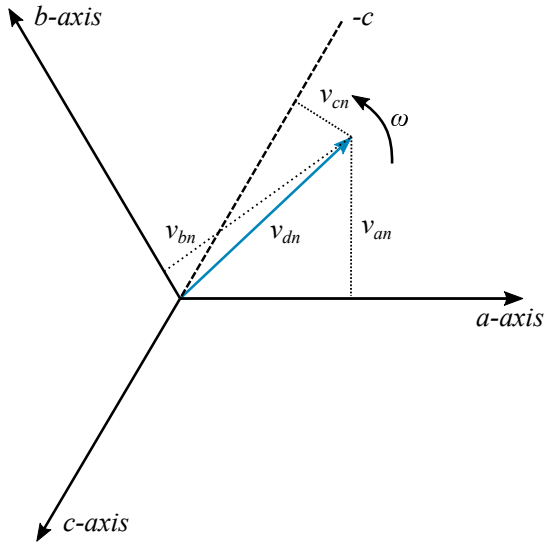

Figure 4.1: A single rotating vector representing the periodically varying phase values

The instantaneous harmonic voltage vector of arbitrary order n can be represented identically:

$$v_{dn} = k \cdot \left[v_{an} \cdot sin\Big(n\alpha\Big) + v_{bn} \cdot sin\Big(n\alpha - \frac{2n\pi}{3}\Big) + v_{cn} \cdot sin\Big(n\alpha + \frac{2n\pi}{3}\Big) \right] \tag{4.3}$$

where the explanations of the various parameters of Eq. 4.3 are presented in Table 4.2.

Table 4.2: Explanation of parameters in Eq. 4.3.

Parameter (s)	**Explanation**
v_{dn}	Instantaneous vector constructed by 3-phase harmonic voltages
v_{an}, v_{bn}, v_{cn}	Instantaneous harmonic phase voltages
k	Transformation constant
α	Phase angle of v_{abc} (in radians)
n	harmonic order (integer multiple of fundamental harmonic)

It follows from the nature of the transformation that the instantaneous vector will be 3/2 times the amplitude of the individual phase voltages [44]. Hence, the transformation constant, k, is chosen to be 2/3. This yields:

$$v_{dn} = V_{pkn} \cdot cos(n\omega t - n\alpha) \tag{4.4}$$

where V_{pkn} is the n^{th} order peak harmonic voltage (V_{pk}/n), and $n\omega t$ is the angle of n^{th} order harmonic in radians. Inspecting Eq. 4.4 it is shown that setting $\omega t = \alpha$ results in the instanta-

neous voltage vector, v_{dn}, becoming a DC quantity, namely V_{pkn}. Thus, a method for measuring the presence of an individual harmonic has been shown, more explicitly the measurement of its peak value.

As v_{dn} now is a DC component, all other components with their individual frequencies will rotate with a motion relative to the frequency of v_{dn}. In addition, the sequence characteristics of harmonics must be taken into account. Taking n=5 as an example, this implies the fundamental frequency components appearing at a rotational speed of $\omega_1 + \omega_5 = \omega_6$. Hence, in this case, the fundamental frequency component will appear as a ripple waveform on top of the non-alternating value of the 5th harmonic, together with all other frequency components. Fig. 4.2 depicts how a selection of harmonic frequencies is relative to the 5th harmonic when using a MSRF for the 5th harmonic. [43].

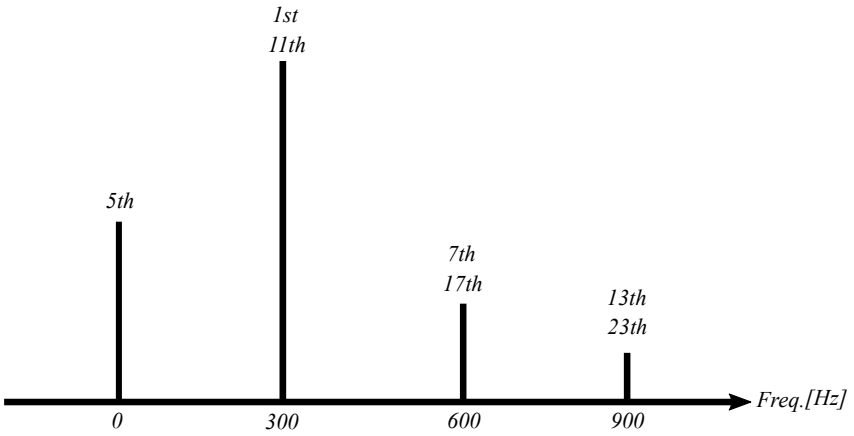

Figure 4.2: Relative frequency of a selection of other harmonics when extracting the 5th harmonic.

In order to filter away the ripple components, the signal is sent through a low-pass filter. Optimally, after filtering, the remaining signal which is to be processed is the DC peak value of the particular harmonic quantity. A complete illustration of the elaborated harmonic detection mechanism for an arbitrary harmonic of order, h, can be observed in Fig. 4.3. Starting from the left in the figure, a sinusoidal voltage is transformed to the synchronous reference frame of order h. As elaborated, this results in the hth harmonic order becoming a DC quantity, $v_{h,pu}^{dq}$, and the other harmonic components appearing as ripple in the form of $\sum_{n \neq h} v_{n,pu}^{dq}$. These components are then filtered through a low-pass filter, resulting in only the voltage of the desired individual harmonic order, namely $v_{h,pu}^{dq}$.

Another frequently used harmonic extraction alternative is using individually tuned band-pass filters. This is regularly done in the $\alpha\beta$-frame, due to its simple implementation. Furthermore, operating in the $\alpha\beta$-frame relieves the control system of the additional computational

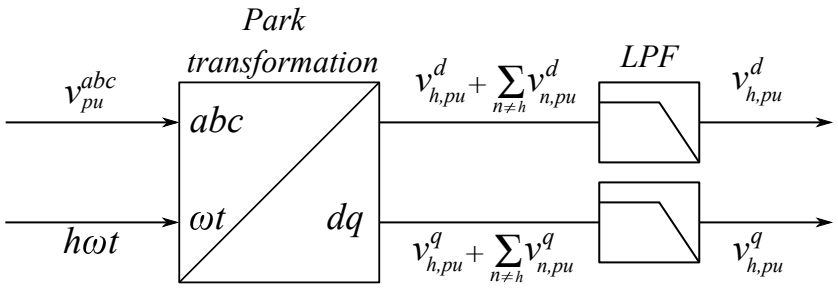

Figure 4.3: An illustration of the harmonic detection mechanism elaborated in this section.

burden involved in the trigonometric calculations of the Park transformation. However, the individual tuning of the band-pass filters are prone to lowered efficiency in a system with frequency changes [38], such as the droop-based microgrid investigated in this thesis. Moreover, delay issues are more prominent when using band-pass filters [24]. These two arguments make the use of MSRFs viable, and legitimizes their presence in the control system of this microgrid.

4.2.4 Virtual Impedance

Virtual impedance is frequently used to alter the output impedance of converters [12]. Conventionally, the concept of virtual impedance can be divided into two structures [16]:

1. Inner virtual impedance, where the virtual impedance is added directly to the modulator signal coming from the primary current control.

2. Outer virtual impedance, where the voltage control reference coming from the droop controller is modified.

With reference to Fig. 3.1 in Section 3.1, the two virtual impedance structures are illustrated in Fig. 4.4. In this figure, output current has been used as an example, although several alternatives exist [16]. The structures depicted are also the ones used in the harmonic sharing scheme in this thesis. In the figures, v_{VI} is the voltage corresponding to the output current, i_o, and the virtual impedance, Z_{VI}.

Virtual impedances have numerous applications, where [16] lists four main categories:

1. Active stabilization.

2. Power flow control.

3. Fault ride-through.

4. Harmonic/unbalance compensation.

The work in this thesis belongs to the last category. More specifically, virtual impedances are used to share the harmonic load evenly between several converters. An elaboration displaying the principle follows.

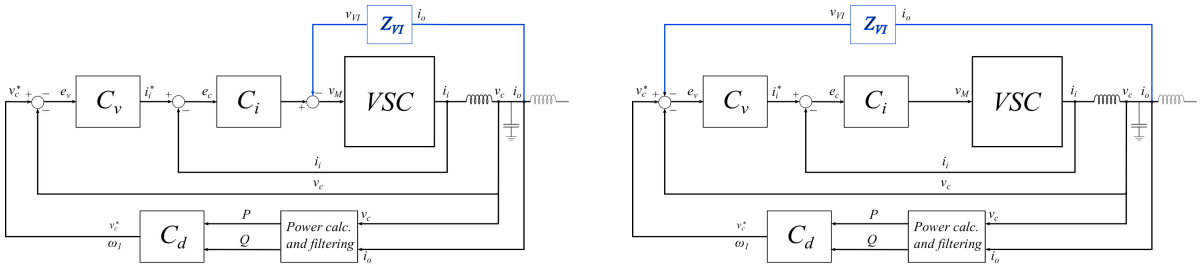

(a) Inner virtual impedance scheme.

(b) Outer virtual impedance scheme.

Figure 4.4: Illustration of inner and outer virtual impedance loops.

Let Fig. 4.5 be a simplified equivalent circuit of the two-DER microgrid, at harmonic frequencies. Z_{Inv_1} and Z_{Inv_2} represent the output impedance of converters 1 and 2, respectively, where both of them consist of the converter output inductance, X_{L_1}, and the virtual impedance of the particular converter, Z_{VI}. Moreover, Z_{Line_1} and Z_{Line_2} represent the line impedance between the filter capacitor point of each converter and the PCC. Recall that X_{L_2} is also regarded as a part of Z_{Line}, as stated in Section 2.4. Lastly, i_h is the harmonic currents injected by the non-linear load.

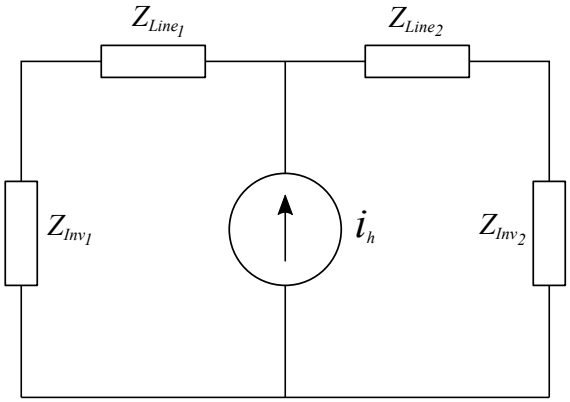

Figure 4.5: A simplified equivalent circuit of the microgrid at a harmonic frequency of order h.

From Fig. 4.5 it can be deduced that the harmonic load current will be equally shared among the converters if the following equation is fulfilled [14]:

$$\begin{aligned} Z_{Inv_1} + Z_{Line_1} &= Z_{Inv_2} + Z_{Line_2} \\ \implies X_{L_1} + Z_{VI_1} + Z_{Line_1} &= X_{L_1} + Z_{VI_2} + Z_{Line_2} \end{aligned} \tag{4.5}$$

Moreover, when the DGs have the same rated power, a term coined harmonic ratio can be used [12] to describe the ratio between them:

$$R_h = \frac{Z_{Inv_1} + Z_{Line_1}}{Z_{Inv_2} + Z_{Line_2}} \tag{4.6}$$

Naturally, when $R_h = 1$, the harmonic load will be shared evenly.

4.3 Harmonic Compensation Scheme

The harmonic compensation scheme utilized in this thesis can be termed selective harmonic compensation, referring to the scheme's individual treatment of harmonics. The scheme is categorized as harmonic *voltage* compensation, as the harmonic presence in the voltage is the parameter which is compensated. Furthermore, in this thesis, the 5th and 7th harmonics are the specific orders compensated, and they are implemented in parallel.

Fig. 4.6 depicts an overview of the general compensation procedure for a harmonic order, h. It is based on using MSRFs, elaborated in Section 4.2.3 to extract the harmonic voltage amplitude of a specific harmonic, $v^{dq}_{h,pu}$. This voltage is then tracked to zero by the use of PI controllers. The controller gain is then transformed inversely, multiplied by its base value, thus becoming $v^{abc}_{h,comp}$. It is then added to the modulator signal coming from the primary current control, namely v^{abc}_{M}. This results in v^{abc}_{conv} being sent to the VSC to be synthesized by the PWM scheme.

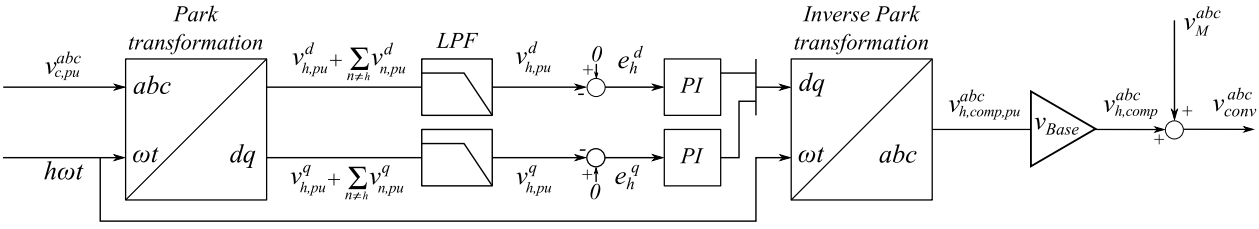

Figure 4.6: An overview of the harmonic compensation scheme.

The bandwidth of the low-pass filters, together with the PI controllers, determine the response speed of the compensation. For the tuning of the LPFs, two factors have been taken into account when determining the bandwidth:

1. Too high bandwidth will make the harmonic controllers interact with the primary voltage and/or current control, leading to instability.

2. Too low bandwidth will lead to a slow response and the need for high controller gains.

According to these factors, the filter bandwidth of the harmonic compensation has been set to the same value as the low-pass filter in the droop control, such that:

$$\omega_{hc} = 10\ rad/s \implies T_{hc} = 0.1\ s \tag{4.7}$$

This is done for all low-pass filters used for both harmonic orders, i.e. the 5th and 7th, in the harmonic compensation scheme. Moreover, the gains for the PI controllers are found in a perturb-and-observe manner. They are equal for both the 5th and 7th harmonic compensation:

$$\begin{aligned} K_{p5} &= K_{p7} = 150 \\ K_{i5} &= K_{i7} = 10 \end{aligned} \tag{4.8}$$

With the harmonic compensation scheme elaborated, it is suitable to present the harmonic sharing scheme. This is done in the following section.

4.4 Harmonic Sharing Scheme

In this thesis, harmonic sharing is defined as the sharing of the harmonic currents between the converters of the system. In this control system, only the converter facing the lowest line impedance, namely converter 2, implements the harmonic sharing scheme. This is because the virtual impedances are based on the difference between the line impedances. Thus, the addition of the line impedance difference to converter 2 will result in even harmonic sharing. Most often, the line impedance difference is not known, thus this assumption represents a simplification. Furthermore, the harmonic sharing is implemented for the 1st, 5th and 7th harmonic.

Referring to the two virtual impedance structures explained in Section 4.2.4, the harmonic sharing scheme in this thesis utilizes both inner and outer virtual impedances. The sharing of the fundamental current component is done with an outer virtual impedance loop, while the sharing of the 5th and 7th harmonic components is done with an inner virtual impedance loop. The reason for this is to avoid the extra measure needed if the 5th and 7th harmonic virtual impedance would be injected in a similar manner as for fundamental virtual impedance. This measure is summarized in a bullet point below.

- Compensation matrices must be utilized to transform the 5th and 7th harmonic into fundamental frequency quantities [29, 39]. These matrices take both the plant and the main controllers (droop, voltage and current) into account. Transfer functions mapping the dynamics between droop, voltage and current control, as well as the plant, have not been

developed in this thesis, representing a challenge in terms of determining the compensation matrices. Thus, instead, the harmonic virtual impedances have been implemented in inner virtual impedance loops, which does not require compensation matrices.

However, both the inner and outer virtual impedance loop use the same virtual impedance structure. As shown in Fig. 4.4 of Section 4.2.4, this structure is dependent on the output current measurement. In addition, to be able to share the harmonic current selectively, the selected harmonic order of the current must be extracted. This is done identically to the harmonic compensation scheme using MSRFs.

The structure of the utilized virtual impedance scheme is illustrated in Fig. 4.7. Starting from the left, the output current, $i^{abc}_{o,pu}$, is transformed into the DC magnitude of a particular harmonic order, h, by the use of MSRFs, elaborated in Section 4.2.3. Then, the extracted DC value, $i^{dq}_{h,pu}$, is multiplied with the virtual impedance. In addition, decoupling is included in the form of $i^{dq}_{o,pu}\frac{h\omega_1}{\omega_{Base}}L_{VI,pu}$. Similar decoupling is done while elaborating current control in Section 3.3. The voltages corresponding to the virtual impedance, $v^{dq}_{VI,h,pu}$, are then transformed to abc quantities by the use of an inverse Park transformation, resulting in $v^{dq}_{VI,h,pu}$. The equations corresponding to the scheme are given in Eq. 4.9.

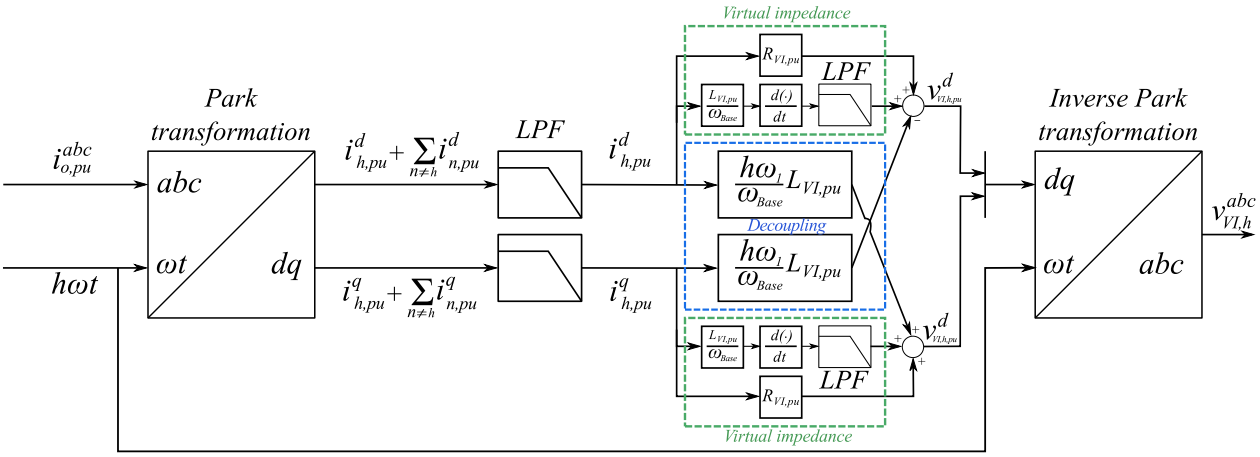

Figure 4.7: An illustration of the harmonic sharing scheme for an individual harmonic order, h.

$$
\begin{aligned}
v^{d}_{VI,h,pu} &= i^{d}_{h,pu}R_{VI,pu} + \frac{L_{VI,pu}}{\omega_{Base}}\frac{di^{d}_{h,pu}}{dt} - \frac{n\omega}{\omega_{Base}}L_{VI,pu}i^{q}_{h,pu} \\
v^{q}_{VI,h,pu} &= i^{q}_{h,pu}R_{VI,pu} + \frac{L_{VI,pu}}{\omega_{Base}}\frac{di^{q}_{h,pu}}{dt} + \frac{h\omega}{\omega_{Base}}L_{VI,pu}i^{d}_{h,pu}
\end{aligned}
\tag{4.9}
$$

Note that the extracted current will not be completely ripple-free, as the low-pass filter only attenuates the harmonics above the cut-off frequency, they do not mitigate them entirely. In

reality, the signal will also contain noise, which the derivative action will amplify. Hence, several techniques to work around this issue have been developed. One of them is inserting a low-pass filter after the derivative controller, filtering out the majority of the noise [16]. As seen in Fig. 4.7, this is done for this scheme, as its implementation is fairly simple. However, this method may introduce high voltage spikes in systems consisting of non-linear loads with a high slew rate [45].

Moreover, the extensive use of transformations in both the harmonic compensation and sharing scheme is computationally demanding, which is a significant drawback. A way to address this challenge is by use of efficient multiple reference frames (EMRFs), utilized in [29, 39]. The implementation of EMRF for this control system is outside of the scope of this thesis and is thus not applied. However, it is included in the recommendations for further work in Chapter 7.

4.4.1 Calculation of Virtual Impedance

Since the filter inductances are equal for both converters, and converter 2 is where the virtual impedance is implemented, Eq. 4.5 becomes:

$$\begin{aligned} Z_{Line_1} &= Z_{Line_2} + Z_{VI_2} \\ \implies Z_{VI_2} &= Z_{Line_2} - Z_{Line_1} \end{aligned} \tag{4.10}$$

Recalling that the virtual impedance scheme utilized is based on the knowledge of the line impedance, the following calculation of $R_{VI,pu}$ and $L_{VI,pu}$ in Eq. 4.10 results in the virtual impedance values shown in Eq. 4.11.

$$\begin{aligned} R_{VI,pu} &= R_{2,pu} - R_{1,pu} = 0.0595\ p.u. = 0.1588\ \Omega \\ L_{VI,pu} &= L_{2,pu} - L_{1,pu} = 0.0419\ p.u. = 0.1116\ \Omega \end{aligned} \tag{4.11}$$

4.4.2 Trade-off Between Sharing and THD

Adding a virtual impedance to the control loop of a converter leads to an increase in THD [35, 40, 46, 42]. Hence, there is a tradeoff between harmonic compensation and voltage distortion. This trade-off is kept in mind when evaluating the efficiency of both the harmonic compensation and the harmonic sharing implemented in the case studies found in the next chapter.

4.5 Complete Control Structure

The implemented control measures, both in this chapter and the previous one, have been elaborated more or less isolated. To give an overview, a complete control structure, consisting of all control measures, is depicted in Fig. 4.8. Red denotes the primary control structure, green the harmonic compensation, and blue the harmonic sharing. As mentioned earlier, i_i, v_c, i_o are the inverter output current, capacitor voltage and output current, respectively. As seen in the figure, these are the three measured quantities. Furthermore, P_1 and Q_1 are the fundamental active and reactive power, respectively, allowing the voltage reference, v_c^*, and frequency reference, ω_1 to be synthesized in the droop control, C_d. C_i and C_v denotes the primary current and voltage control open loop transfer functions, respectively.

Moreover, the inner virtual impedance loops are represented by $Z_{VI_{5,7}}$, while the outer virtual impedance loop is represented by Z_{VI_1}. These two loops produce their respective voltage, v_{VI}, corresponding to the virtual impedance of their harmonic order. C_{hc} is the harmonic compensation scheme, adding its output to the current control output, resulting in the modulator signal sent to the converter, v_{conv}.

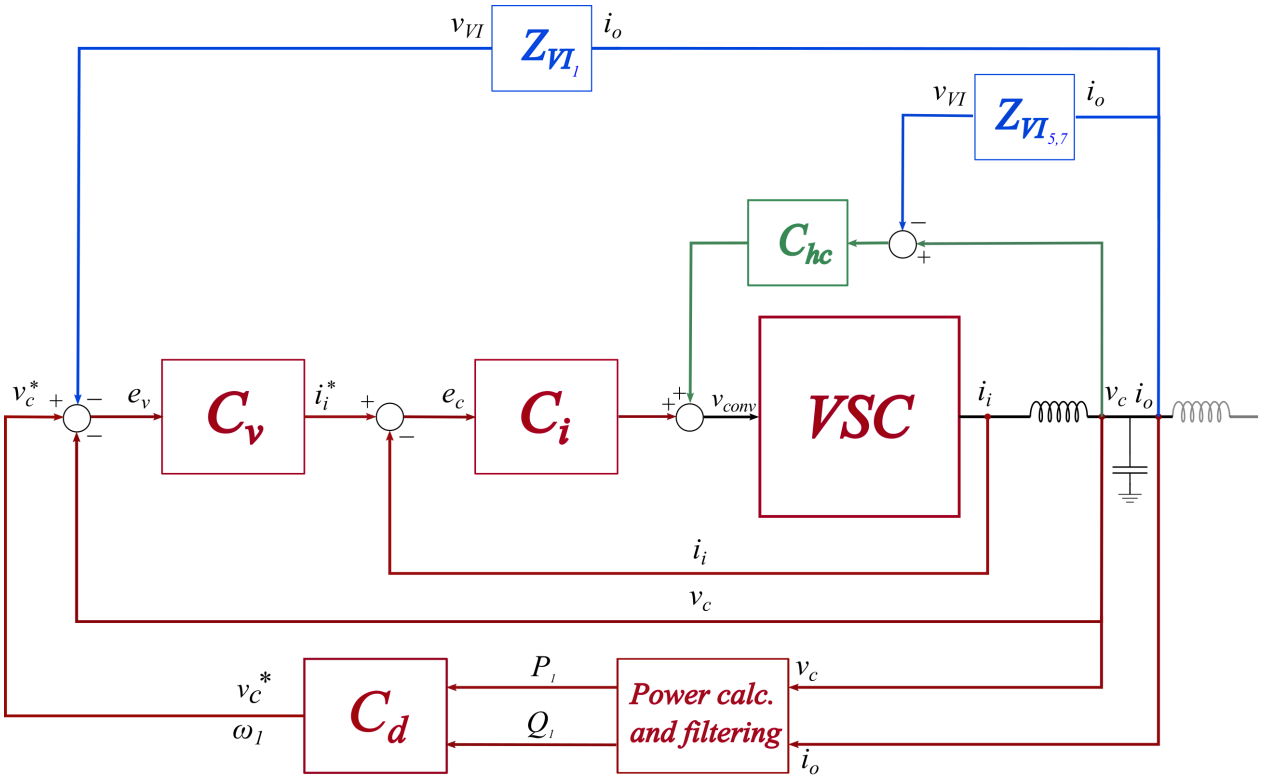

Figure 4.8: The complete structure of the control system, including primary control, harmonic compensation and harmonic sharing.

Chapter 5

Case Studies

This chapter displays the different cases investigated, along with simulation results and discussion. The chapter starts by briefly introducing the investigated cases. Then, key performance indicators are presented in Section 5.2, while Section 5.3 presents all simulation model parameters in a table. Moreover, the base case and the 4 additional cases are presented in Sections 5.4 to 5.8.

5.1 Introduction of the Case Studies

The base case introduces the system without harmonic sharing in order to display the uneven sharing of the harmonic currents. In addition, the voltage reference is increased to compensate for the voltage drop across the line impedance, and thus supply the desired voltage amplitude at the PCC.

In case 1, the harmonic sharing schemes for the three selected harmonic orders (1st, 5th and 7th), are enabled one by one to evaluate the efficiency of their independent harmonic sharing scheme. The KPI responses of case 1 is subsequently used as the basis for comparison for the other cases.

Case 2 aims to compensate the harmonics at the PCC instead of the capacitor voltage. The THD of the PCC voltage is observed to be high, resulting in the interest for this case. First, harmonic compensation is enabled to see if compensation is achieveable. Furthermore, the harmonic sharing schemes are enabled one by one to see how they affect the KPIs.

Case 3 implements opposite droop instead of conventional droop, particularly to investigate the difference in fundamental current sharing between the two droop schemes.

Case 4 adds a linear load between two phases in order to see how this affects the KPIs, and

especially to check whether the values of the load parameters are acceptable.

As can be seen, a single system alteration has been done in each of the cases 2-4. Limiting the number of alterations in each case to one is done to evaluate the effect of the particular alteration. In addition, key takeaways are included in a case summary at the end of each case to provide an overview of the results.

5.2 Key Performance Indicators

Key performance indicators (KPIs) are defined to be able to quantify and compare the results obtained in the different simulation cases. The KPIs and the rationale behind them are summarized below.

1. **Apparent powers: S_1 and S_2.** The apparent powers of the converters reflect how much they are supplying, compared to their rated power. The apparent powers are calculated using filtered active and reactive power. Thus, this KPI will only be able to quantify the apparent power supply affiliated with the fundamental harmonic component. Hence, studying the apparent power is not suitable for evaluating the effect of current sharing for harmonic components other than the first order.

2. **THD of compensated voltage.** The trade-off between harmonic sharing and THD is explained in Section 4.4.2. Hence it is interesting to see how the sharing measures affect the THD. It should also be noted that only one of the phases is inspected, as the THDs of the phases are approximately equal. When this is not the case, the difference in THD between the phases is investigated.

3. **Harmonic current differences: i_{2n}-i_{1n}.** This denotes the difference in harmonic current, of order n, between the two converters, i.e. $i_{2n} - i_{1n}$. It quantifies how well the harmonic sharing is working for a particular harmonic current component. If this value is zero, the converters are sharing the harmonic current of this order perfectly.

   In the current literature, different parameters have been used to quantify harmonic sharing. Among these are harmonic power [47, 14], harmonic reactive power [48] and harmonic currents [11, 26]. The latter is chosen for its simplicity. However, the harmonic currents extracted for comparison are subject to low-pass filtering. The filter does not attenuate the high-frequency harmonics completely, resulting in ripple in the output signal of the filter. This ripple will lead to a weak coupling to other harmonics, representing

a disadvantage. Nonetheless, using harmonic or reactive power would lead to the same disadvantage, as their calculation is also subject to low-pass filtering [14, 48].

4. **Load parameters: v_{DC}, i_{DC} and P_{DC}.** The load parameters are monitored to see how large impact the harmonic sharing has on the load, as well as how the alterations made in the other cases affect the load. As discussed in Section 2.5, a focus is to limit the ripple seen by the load. Recall that the capacitor was designed to limit the ripple to 27 V. Furthermore, the load should be supplied with its designated voltage and power, namely 540 V and 100 kW, respectively.

5.3 System Parameters

One of the objectives of this thesis is to acquire simulation results which can later be used for comparison with laboratory results. To ease reproduction of the simulated microgrid and its control system, all parameters elaborated up to this point are collected in Table 5.1.

Table 5.1: System parameters.

Model parameters			**Control parameters**		
Parameter	Symbol	Value	Parameter	Symbol	Value
AC-side inverter voltage	V_{LL}	400 V	Proportional gain of the current PI controller	K_{pi}	1.125
System frequency	f_1	50 Hz	Integral gain of the voltage PI controller	K_{ii}	1930
DC-side inverter voltage	V_{DC}	750 V	Proportional gain of the voltage PI controller	K_{pv}	0.1388
Rated power	S_N	60 kVA	Integral gain of the voltage PI controller	K_{iv}	26.16
Rated RMS output current	I_N	100 A	P/f droop coefficient	m	$6.28 \cdot 10^{-5}$
Switching frequency	f_{sw}	6 kHz	Q/V droop coefficient	n	$1.28 \cdot 10^{-3}$
Inverter side filter inductance	L_1	500 μH	Bandwidth of all low pass filters	ω_n	0.1 rad/s
L_1 parasitic resistance	R_{L_1}	6 mΩ	Proportional gain of the harmonic PI controllers	$K_{p5,7}$	150
Filter capacitance	C	50 μF	Integral gain of the harmonic PI controllers	$K_{i5,7}$	10
Grid side filter inductance	L_2	200 μH	Resistive virtual impedance	R_{VI}	0.1588 Ω
L_2 parasitic resistance	R_{L_2}	0.8 mΩ	Inductive virtual impedance	L_{VI}	0.1118 Ω
Line resistance between converter 1 and the PCC	R_{Line_1}	0.4764 Ω			
Line reactance between converter 1 and the PCC	X_{Line_1}	0.3348 Ω			
Line resistance between converter 2 and the PCC	R_{Line_1}	0.3176 Ω			
Line reactance between converter 2 and the PCC	X_{Line_1}	0.2232 Ω			
Load side inductor	L_L	120 μH			
Load capacitance	C_L	1500 μF			
Load voltage	V_{DC}	540 V			
Power set to be drawn from the load	P_{DC}	100 kW			

5.4 Base Case: No Harmonic Sharing

The purpose of the base case is to introduce the initial system where primary control and harmonic compensation is implemented, but harmonic sharing is not yet enabled. This way, the demand for harmonic sharing is displayed. However, during preliminary simulations, the converters were seen to supply far below their rated power, Moreover, the DC load voltage was observed to be far below its rated value of 540 V. Hence, the voltage reference of the converters is increased from 400 to 470. The exact value of this increase was found through observing the load voltage while increasing the reference voltage step-wise.

The enabling of harmonic compensation and voltage reference increase are according to Table 5.2.

Table 5.2: Enabling specifications for the base case.

t = 0 s	**t = 0.5 s**	**t = 1.0 s**
Only primary control implemented	Harmonic compensation enabled	Voltage reference adjusted

Apparent Powers

Fig. 5.1 shows the apparent powers of the two converters. The system is seen to be stable and responsive. At t = 0 s, neither the harmonic compensation nor the voltage adjustment are enabled. The converters supply well below their rated power of 60 kVA, as stated earlier. Furthermore, converter 2 supplies more power than converter 1, as it is connected to the lowest line impedance.

At t = 0.5 s, when the harmonic compensation is enabled, the apparent power of both converters are observed to rise marginally. As elaborated when presenting this KPI, this rise has to do with the fundamental components coupling to the other harmonics. Moreover, the responses are observed to be relatively slow, due to the low pass filters affiliated with apparent power calculation.

At t = 1 s, the voltage reference is adjusted, and the power supplied rises substantially for both converters. At this point, converter 1 is still operating below its rated power, while converter 2 supplies more than its rating allows. This scenario illustrates the main unwanted consequence of uneven harmonic sharing; one converter is now operating above its capability, while the other is not. However, converter 2 is only operating 1.25 kVA above its rating. One could argue whether this is substantial enough to have a quantifiable effect on the converter. Nonetheless, the issue of uneven sharing is displayed, allowing the harmonic sharing enabling in case 1 to be assessed.

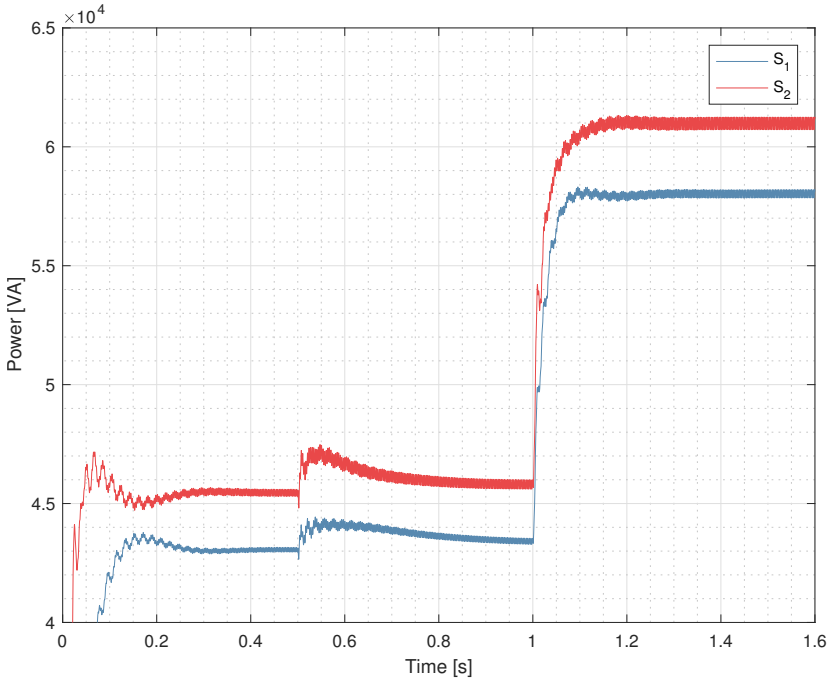

Figure 5.1: Apparent powers of both converters for the base case.

THD

Fig. 5.2 depicts the THD response of the capacitor voltage for the converters in the microgrid. At t = 0 s, harmonic compensation is disabled, resulting in a certain harmonic distortion in the capacitor voltage. The value is, however, still below the Norwegian grid code limit of 5% [22]. Hence, the demand for harmonic compensation of the capacitor voltage is not really present. This is because the distortion of the capacitor voltage is only due to the current running through the converter side inductor, which is relatively small. A far larger distortion is present at the PCC voltage, due to the line impedance, which is the rationale for case 2.

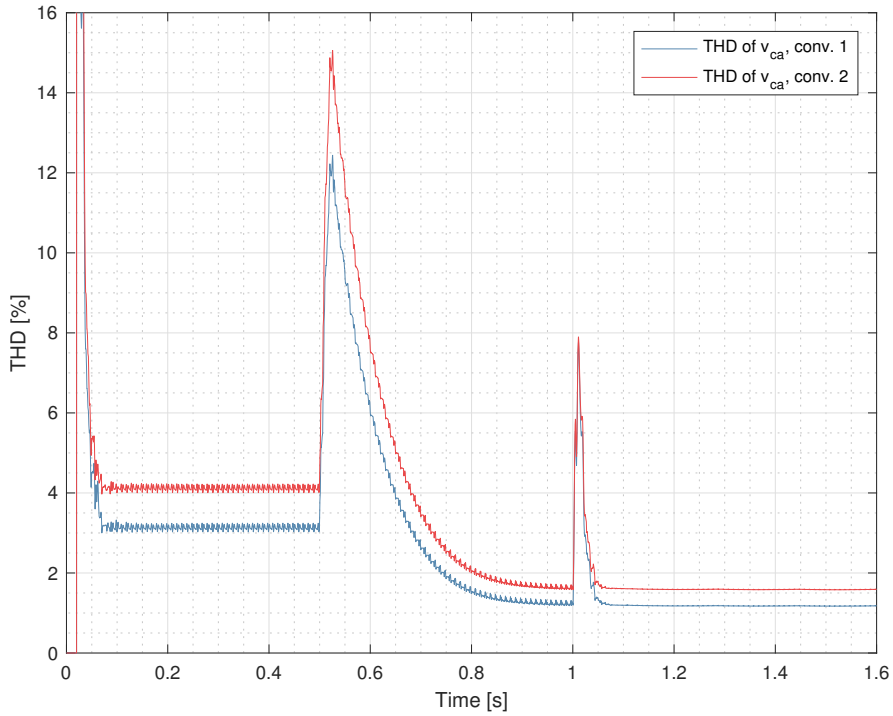

Figure 5.2: Base case capacitor voltage THD of phase a for both converters.

At t = 0.5 s, the harmonic compensation measures are implemented. The efficiency of the harmonic compensation scheme is depicted, as the THD levels clearly decrease. Taking converter 1 as an example, the THD is observed to decrease from 3.49% to 1.28%.

However, a high transient spike in the THD occurs at the moment of enabling. This is suboptimal, as it might harm connecting loads. On the other hand, if the harmonic compensation is assumed to always be on in an operating system, this would not be an issue. The spike is due to the integral part of the PI controllers. Fig. 5.3 shows the PI controller output for the 5th harmonic compensation loop for converter 1. From t = 0 to t = 0.5, the extracted harmonic voltage component is accumulated, resulting in a high PI gain when the harmonic compensation is enabled. This indicates that the harmonic compensation measures should be enabled before any

loads are connected, or that the integral part of the controllers should be reset at the moment of enabling.

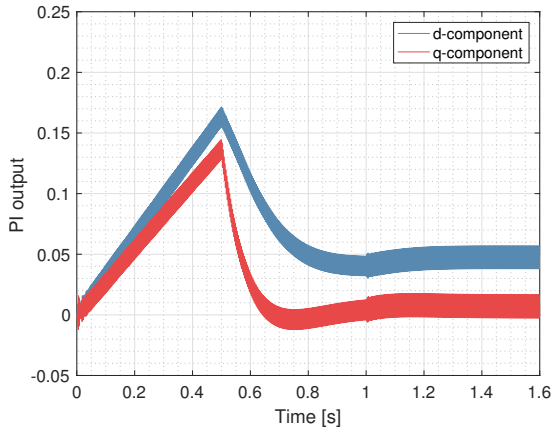

Figure 5.3: PI controller output of converter 1 for the 5th harmonic component.

When the voltage reference is changed at t = 1 s, another transient spike occurs in the THD. This is however due to the rise in current. Nevertheless, steady-state conditions show that the voltage reference rise does not affect the THD much. Furthermore, to evaluate the harmonic compensation in a more detailed manner, FFT analysis results are presented in Fig. 5.4. It is observed that the compensated harmonics of the 5th and 7th order are almost entirely mitigated. In addition, it is noted that some harmonic orders other than the expected ones are present, such as the 4th and 6th harmonic in Fig. 5.4b. This is due to the FFT analysis being based on a fundamental frequency. This frequency is regularly changed by the droop control, resulting in the issue of determining the exact value of it. Hence, these low value harmonics are disregarded in the evaluation.

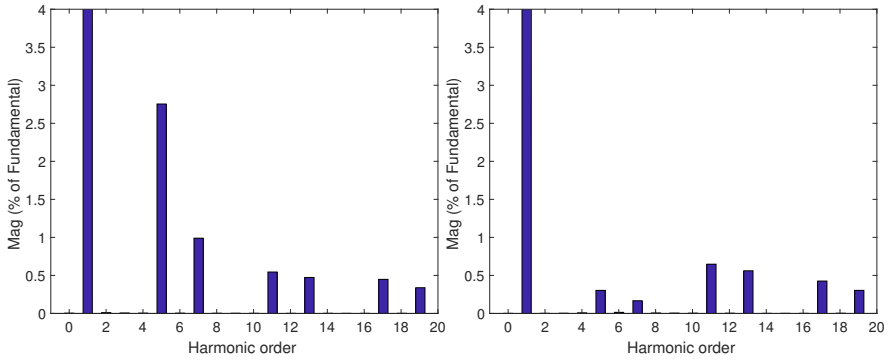

(a) Harmonic sprectrum at t = 0.4 s. (b) Harmonic spectrum at t = 0.9 s.

Figure 5.4: Harmonic spectrum of capacitor voltage before and after harmonic compensation.

Harmonic Current Differences

Harmonic current differences for this case are shown in Fig. 5.5. At t = 0 s, when only the primary control is active, the uneven sharing is evident for all the three displayed harmonic orders (1, 5, 7). The situation is worsened for the 5th and 7th harmonics when their compensation scheme is implemented at t = 0.5. This displays how the harmonic compensation deteriorates the current sharing of these harmonics between the converters. Furthermore, it allows the harmonic sharing scheme enabled in the next case to display its efficiency.

Moreover, the voltage rise at t = 1 s is observed to exacerbate the current sharing for all three displayed harmonics. This is due to the increased power supplied by the converters, which implies higher current, and hence, a slight increase in the current differences.

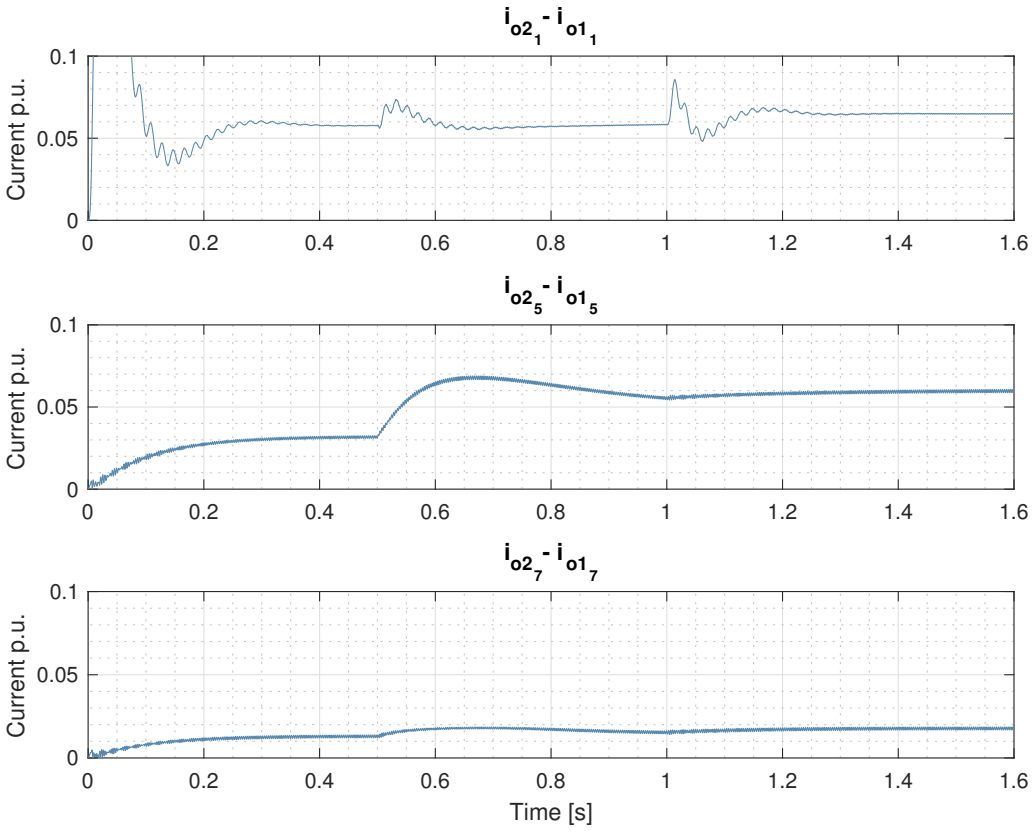

Figure 5.5: Base case difference in converter output current for the 1st, 5th and 7th current component.

Load Parameters

Fig. 5.6 depicts the load parameters for this case. At t = 0 s, voltage and power are observed to be be below their preferred values of 540 V and 100 kW, respectively.

When harmonic compensation is enabled at t = 0.5 s, the values are approximately constant, but the ripple increases considerably. However, the voltage ripple is still only measured to be 15 V, well within the set limit of 27 V.

Increasing the voltage reference at t = 1 s increases the ripple slightly, and manages to deliver the desired output parameters to the load.

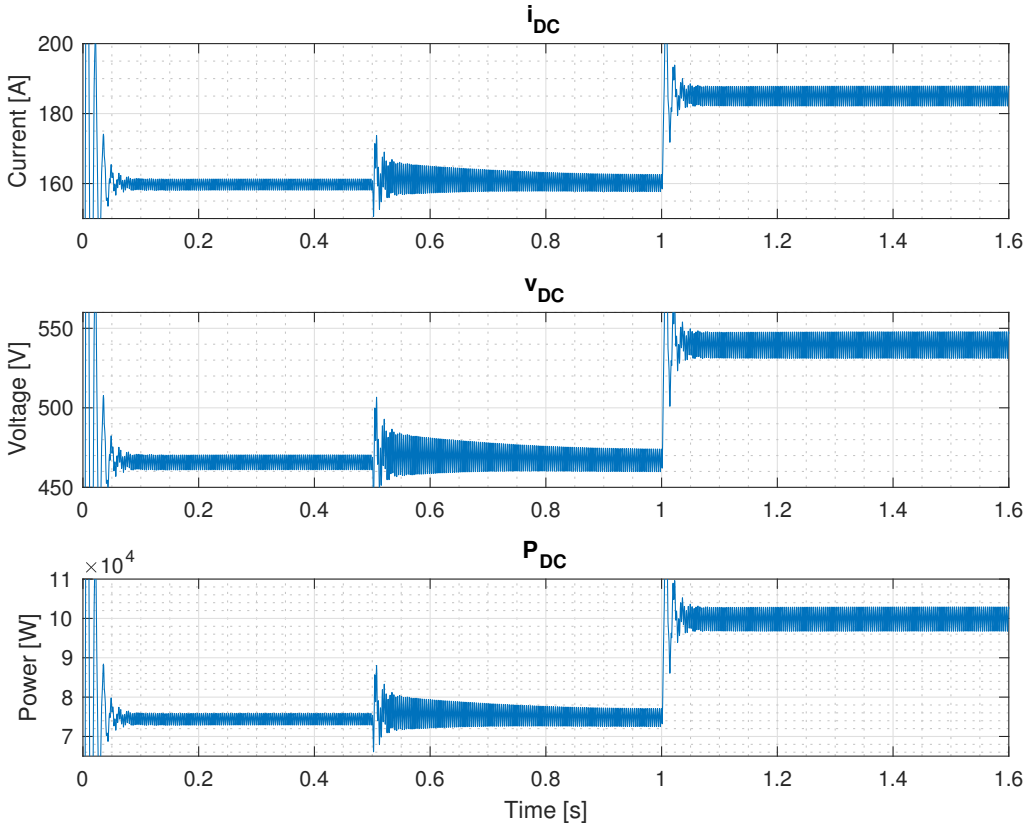

Figure 5.6: Load parameters for the base case.

Case Summary

- This case displays the initial system where primary control and harmonic compensation is implemented, but before the harmonic sharing scheme is enabled.
- Apparent powers behave as expected, resulting in a final steady-state showing the unwanted consequence of uneven harmonic sharing, where converter 2 is supplying 1.25 kVA above its rated power.
- THD is seen to decrease from 3.49% to 1.28% when the harmonic compensation scheme is enabled, which proves the feasibility of the scheme.
- Harmonic current differences are observed for all three selected harmonic orders, displaying uneven harmonic sharing. The individual current differences at the final steady-state are 0.065, 0.060 and 0.018 for the 1st, 5th and 7th harmonic current, respectively.
- After the voltage reference increase at t = 1 s, v_{DC} and P_{DC} obtain their intended values of 540 V and 100 kW, respectively, at steady-state. This allows evaluation of the effect of harmonic sharing in the next case. In addition, the voltage ripple values is observed to be 15 V, well within its designed limit of 27 V.

5.5 Case 1: Harmonic Sharing

This case represents a central objective of the thesis, namely to present simulation results verifying the applicability of the elaborated control system to achieve harmonic sharing. The virtual impedance loops for the different harmonic components are enabled according to Table 5.3.

Table 5.3: Enabling specifications for case 1.

t = 0 s	**t = 1.0 s**	**t = 2.0 s**	**t = 3.0 s**
Harmonic compensation enabled, no harmonic sharing enabled	Harmonic sharing for the fundamental current component initiated	Harmonic sharing for the 5th harmonic current component initiated	Harmonic sharing for the 7th harmonic current component initiated

Note that the steady state condition observed after the voltage reference rise in the previous case is a suitable basis to assess the harmonic sharing scheme. This is due to the following reasons:

1. One converter is supplying above its rated power, comprising the demand for harmonic sharing.
2. Harmonic compensation is working, allowing an evaluation of the dynamics between this scheme and harmonic sharing.
3. The uneven harmonic sharing for all three assessed harmonic orders are present, displaying the main issue investigated in this thesis clearly.
4. The load has adequate parameters, which allows for an investigation into whether the harmonic sharing worsens the situation or not.

In the base case the voltage reference rise was done by adding 70 V to the base voltage in the Simulink model, not updating the base voltage itself. However, in this case, the voltage base value itself is changed, and the remaining system parameters change slightly due to this. This leads to marginally altered KPI values, but all trends are the same, thus not affecting the evaluation done in the base case and this chapter.

Apparent Powers

The period of t = 0 s to t = 1 s in Fig. 5.7 represents the steady-state acquired in the base case, where the difference in supplied power is measured to be 2,6 kVA. Then, when the fundamental harmonic sharing is applied at t = 1 s, the supplied power of both converters is observed to drop. Simultaneously, the difference between them decreases, and converter 1 starts to supply slightly more of the load, resulting in a supply difference of 0.4 VA. This implies that the fundamental harmonic sharing has worked to a certain extent: It is able to decrease the difference, but not perfectly. Furthermore, the total power delivered has decreased substantially, reflected in the response of the load parameters discussed later in this section. A way to mitigate this issue could be to once again raise the voltage reference, as was shown to work in the base case.

The initiation of the current sharing for the 5th and 7th harmonic, at t = 2 s and t = 3 s, respectively, does not affect the apparent powers much. A slight decrease is observed in the supplied power from both converters, but the difference between them is practically unchanged. As discussed earlier, this is due to the calculation of the apparent power being based on filtered active and reactive power.

In addition, it is noted that a similar limited enhancement of reactive power sharing is reported in [49], where it is also indicated that a secondary control layer is needed to update the droop control power references in order to achieve perfect reactive power sharing. This is transferable to this result, as apparent power is a product of reactive power. Moreover, as mentioned in Section 3.5, only control at the primary layer is implemented in this thesis. Hence, adding a secondary control system is part of further work listed in Chapter 7.

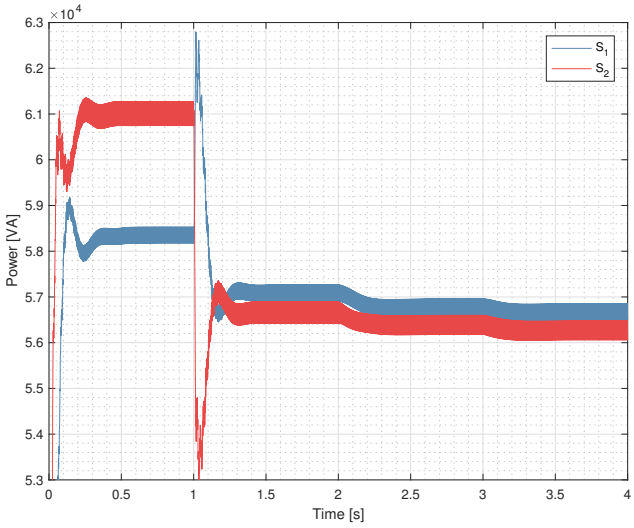

Figure 5.7: Apparent powers of both converters for case 1.

THD

Fig. 5.8 shows the THD response as the harmonic sharing schemes for the different harmonic orders are activated. At t = 1 s, when the fundamental current sharing is enabled, no persistent effect is observed. This is due to the fact that the outer virtual impedance loop used for the fundamental current sharing only alters the voltage reference with a fundamental voltage. Hence, the THD is relatively unaffected.

However, when the harmonic sharing is enabled for 5th and 7th harmonic order, at t = 1 s and t = 2 s, respectively, the THD of converter 2 rises. This is sensible, as the harmonic sharing scheme is implemented for converter 2. Furthermore, the THD rise shows the trade-off between THD and harmonic sharing, explained in Section 4.4.2.

The steady state THD measured at t = 3.9 s is 1.29% for v_{ca} of converter 1, and 3.97% for v_{ca} of converter 2. Hence, no THD is above 5%, i.e. the THD levels are according to regulations. As the harmonic sharing schemes only lead to a minor rise, they are evaluated as successful in terms of having a limited aggravating effect on the THD.

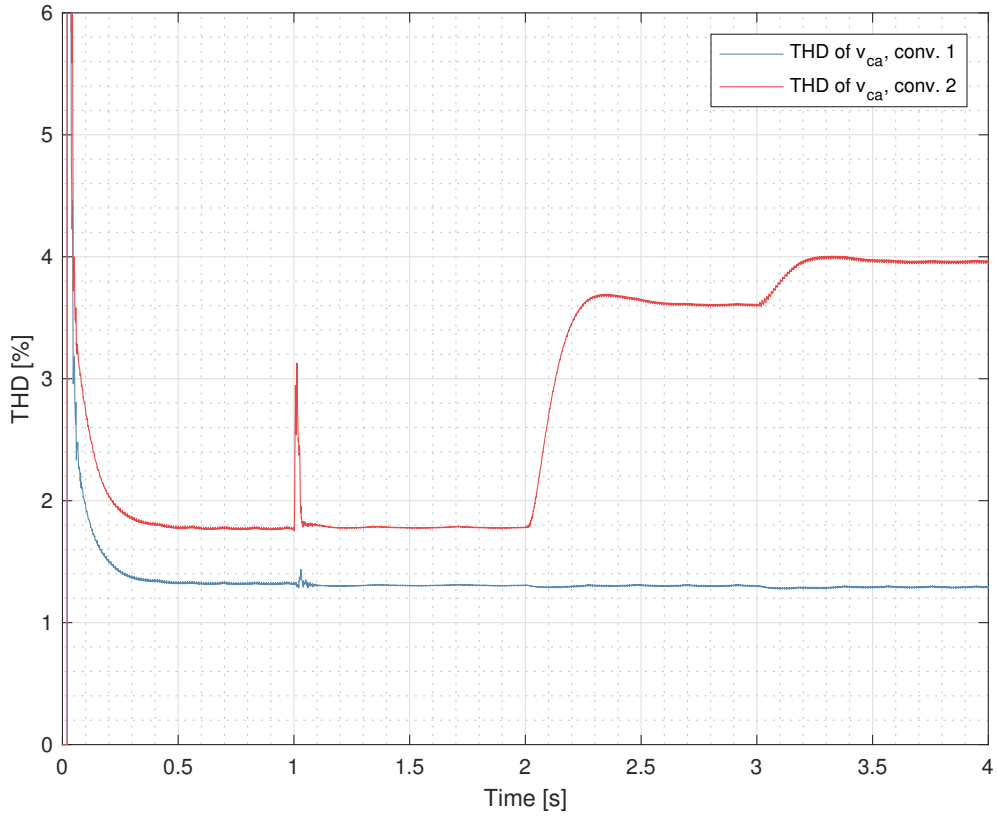

Figure 5.8: Case 1 capacitor voltage THD of phase a for both converters.

Harmonic Current Differences

Fig. 5.9 verifies the capability of the implemented harmonic sharing scheme. The sharing scheme for the fundamental harmonic current component, enabled at t = 1 s, improves the sharing, but only to a certain extent. The difference is reduced from 0.072 p.u. to 0.033 p.u., i.e. there is room for improvement. One reason for the suboptimal performance is the droop scheme. Recall that in this case, conventional droop is used on a system where line impedances are mostly resistive. This implies a partly successful power sharing, which is what is shown here, as well as in the apparent power response. This line of thought builds the interest in looking at the system response when opposite droop is implemented. Hence, case 3 investigates the effect of using an opposite droop configuration instead of the conventional one used in the other cases. In addition, as mentioned when discussing the apparent power response of this case, a secondary control layer to update the droop should be present in order to achieve perfect fundamental current sharing. Thus, case 3 will investigate if opposite droop improves the sharing, but it is not expected to achieve perfect sharing, due to the lack of a secondary control layer.

However, it is observed that the sharing of the 5th current component component is almost perfect, while the sharing of the 7th current component is completely achieved. These results are in compliance with the limited success of the fundamental current sharing. The reason for this is that the sharing of the 5th and 7th harmonic current component is only weakly coupled with the droop control (due to the low pass filtering), while the fundamental current and apparent power sharing is directly dependant on droop control. Hence, the lack of secondary control layer does not affect the sharing of the 5th and 7th harmonic current much.

The results achieved here corresponds to a central objective of the thesis, namely to present simulation results verifying the applicability of the elaborated control system to achieve harmonic sharing.

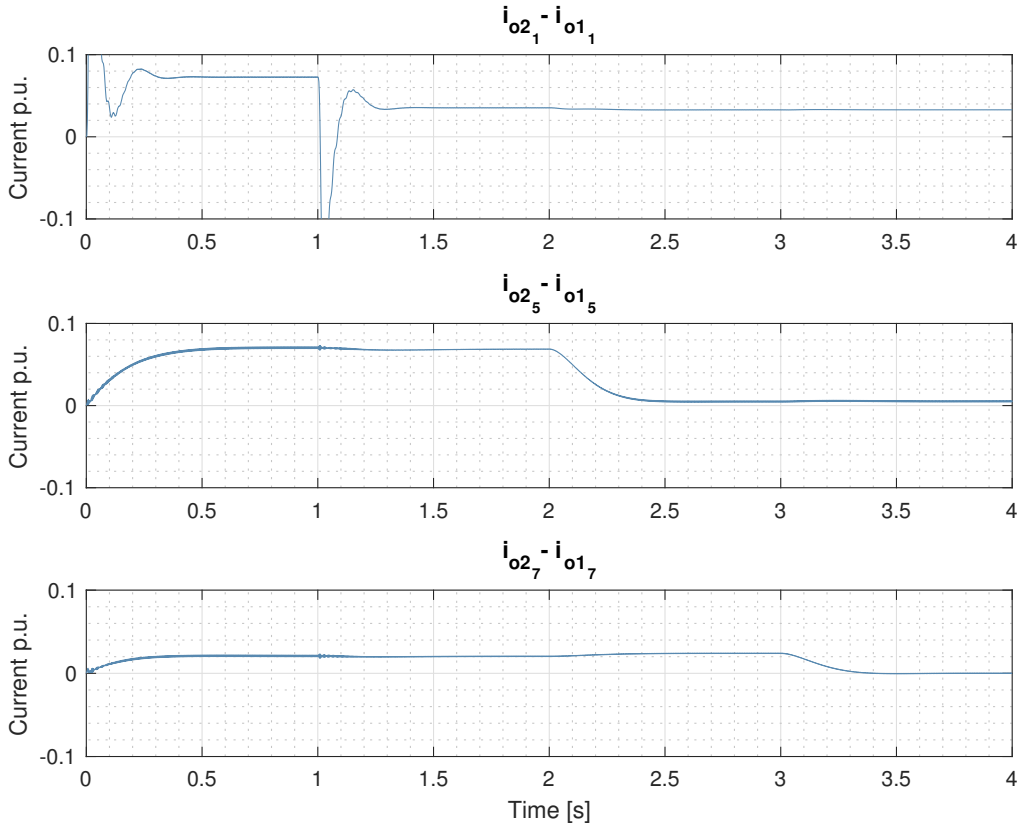

Figure 5.9: Case 1 difference in converter output current for the 1st, 5th and 7th current component.

Load Parameters

Fig. 5.10 shows a similar trend for the load parameters as for the apparent powers. During the interval of t = 0 s to t = 1 s, the parameters are at their desired values of 540 average value and 100 kW, as mentioned in the previous case. Moreover the voltage ripple is only 15 V, well below the set threshold of 27 V.

Then, at t = 1 s, when the fundamental harmonic sharing is enabled, all three load parameters drop. Specifically, the voltage and power is observed to drop to the average values of approximately 530 V and 95 kW, respectively. This is because the voltage corresponding to the fundamental harmonic sharing scheme is subtracted from the initial voltage reference. Hence, the new voltage reference is lower, and an offset from the preferred conditions of 540 V and 100 kW is observed. However, the offset is not substantial, and as discussed when presenting the apparent power response, a voltage reference rise could mitigate this issue. Moreover, the ripples of the parameters are observed to be fairly constant, maintaining acceptable ripple values.

The other harmonic sharing schemes, initiated at t = 2 s and t = 3 s, marginally exacerbate the load parameters. Hence, as a whole, the harmonic sharing scheme implementation preserve the desired conditions for the load parameters in a satisfying manner.

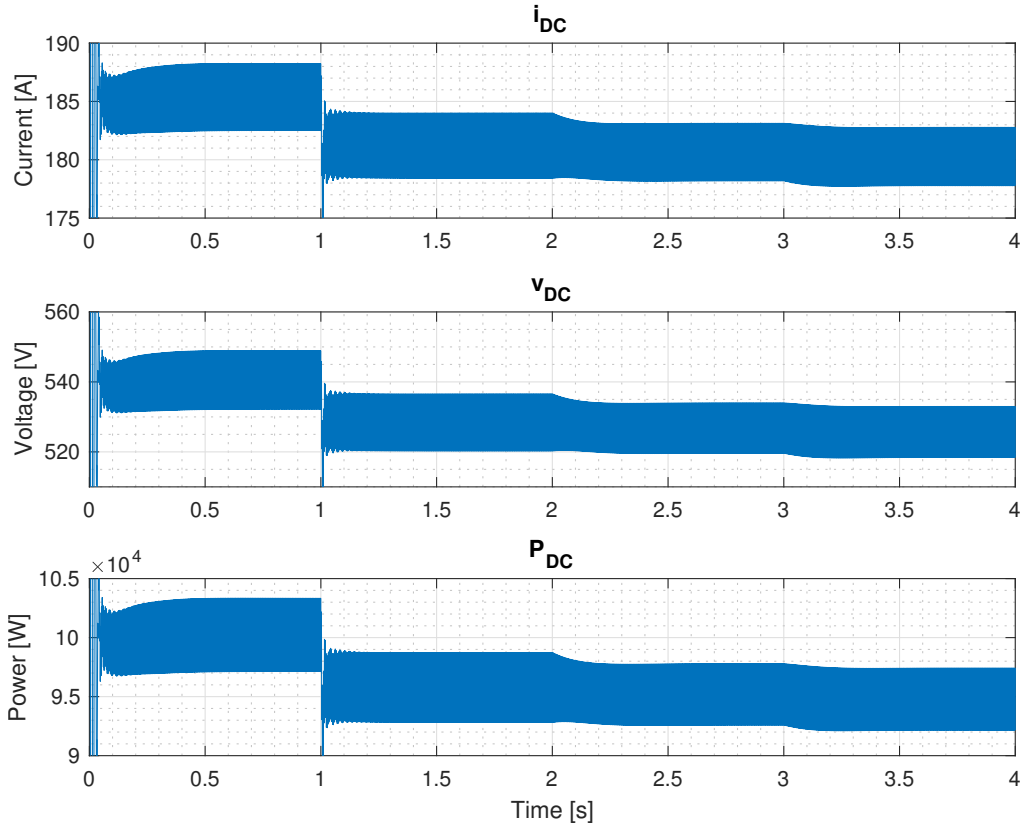

Figure 5.10: Load parameters for case 1.

Although the harmonic compensation and sharing schemes are working, it is important to note that the PCC voltage is heavily distorted. This can be observed by investigating the THD of the PCC voltage, depicted in Fig. 5.11a. At t = 3.5 s, when all harmonic sharing measures are enabled, the THD of the PCC voltage is measured to be 15.65%. The FFT analysis of Fig. 5.11b enlightens the issue further, depicting the same pattern seen earlier, but with a higher presence of all harmonics.

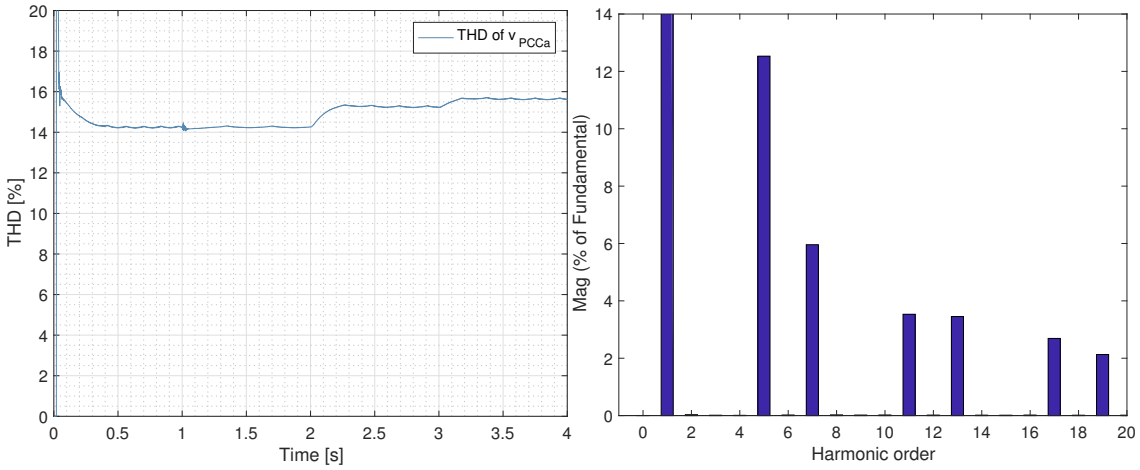

(a) THD of the PCC voltage

(b) Harmonic spectrum at t = 3.5 s.

Figure 5.11: THD of PCC voltage and harmonic spectrum of PCC voltage.

The heavy distortion of the PCC voltage represents a suboptimal situation for auxiliary equipment connecting to the PCC. Hence, it is of interest to investigate if it possible to compensate the PCC voltage with the current model and control system. This is done in the following case, namely case 2.

Case Summary

- This case displays the applicability of the harmonic sharing schemes, assessing the harmonic orders shared individually.
- The apparent powers show an initial difference for 2.6 kVA, being reduced to 400 VA after the enabling of fundamental current sharing. In addition, the power supplied by both converters drop at the time of enabling for all three harmonic orders, where the fundamental current sharing enabling leads to the most substantial drop.
- The THD of converter 2, where the virtual impedance is implemented, is observed to rise when the current sharing of the 5th and 7th harmonic is enabled. The THD is 3.97% at the final steady-state, still below the regulated limit of 5%.
- All three harmonic current differences decrease, veryfying the applicability of the harmonic sharing scheme. However, the fundamental current sharing goes from 0.072 to 0.033, indicating successful scheme with a certain room for improvement.
- The load parameters are observed to drop at the enabling of all three sharing schemes, where the fundamental current sharing scheme leads to the most substantial drop. However, the values are still regarded as acceptable for the load to function properly.

5.6 Case 2: Harmonic Sharing and PCC Voltage Harmonic Compensation

As stated in Section 2.5, having a distorted PCC voltage results in several substantial disadvantages for auxiliary loads connecting to the PCC. This issue forms the basis for the interest in this case, where the harmonic compensation is allocated to the PCC voltage. The goal of the case is to investigate if the THD of the PCC voltage can be improved by this simple reallocation, but also to see how the other KPIs react to this control system change.

The reallocation of harmonic compensation is done by simply injecting a measurement of the PCC voltage to the harmonic compensation scheme, instead of the capacitor voltage measurement done in the other cases. The scheme will then try to track the 5th and 7th harmonic component of the PCC voltage to zero.

A clear disadvantage of this scheme is the dependence of a PCC voltage measurement. In a real-life microgrid, this type of measurement is not necessarily present or easy to obtain, due to the following reasons:

1. The PCC can be far away from the converter and its control system, representing the need for communication infrastructure to transfer the measurement signal.

2. Measuring PCC voltage represents an extra measurement, i.e. extra measuring equipment, and thereby increased cost.

Alternatively, the PCC voltage can be calculated when the line impedances are known. However, as the line impedances will change with time due to aging, weather, etc., the line impedance values need to be updated to provide the correct calculation of the PCC voltage.

During preliminary simulations, the time for steady-state to occur increased in this case. This resulted in a different enabling specification scheme, found in Table 5.4.

Table 5.4: Enabling specifications for case 2.

t = 0.5 s	**t = 4 s**	**t = 7 s**	**t = 10 s**
Harmonic compensation initiated	Harmonic sharing for the fundamental current component initiated	Harmonic sharing for the 5th harmonic current component initiated	Harmonic sharing for the 7th harmonic current component initiated

Apparent Powers

Fig. 5.12 shows a clear increase in apparent power for both converters when the harmonic compensation is enabled at t = 0.5 s. Both converters start operating above their rating of 60 kVA, a scenario which can not persist if the converters are to avoid deterioration. In a real life microgrid with installed protection mechanisms, the converter would probably be decoupled from the system to avoid damage. In addition, the ripples of the converters are approximately 5 kVA, and therefore substantially larger than the corresponding ripple value of approximately 0.5 kVA shown in case 1. The ripple delimits the evaluation of harmonic sharing, but by investigating the numbers constituting the graph, the difference is observed to be the same as in the previous case. That is, approximately 2.6 kVA.

At t = 4 s, when the fundamental harmonic sharing is enabled, the response is similar to the ones observed in the previous cases: The power of both converters drop, and the sharing improves. However, in this case, both converters are still operating above their rated power.

The current sharing for the 5th harmonic component is enabled at t = 7 s. This results in a major increase of approximately 20 kVA in supply for both converters. Simultaneously the ripple of S_1 increases, while the ripple of S_2 decreases, indicating a peculiar dynamic in the system. This dynamic is also present when the sharing scheme of the 7th harmonic is initiated at t = 10 s. This enabling, however, leads to a drop in power supplied.

The results observed are not satisfying. The converters are constantly operating above their rated power, and show a behave differently compared to case 1, where the apparent power response is deemed adequate. Moreover, the harmonic sharing schemes of the 5th and 7th harmonic are clearly affecting the system in undesireable ways. This dynamic is also illustrated in the following KPI evaluations.

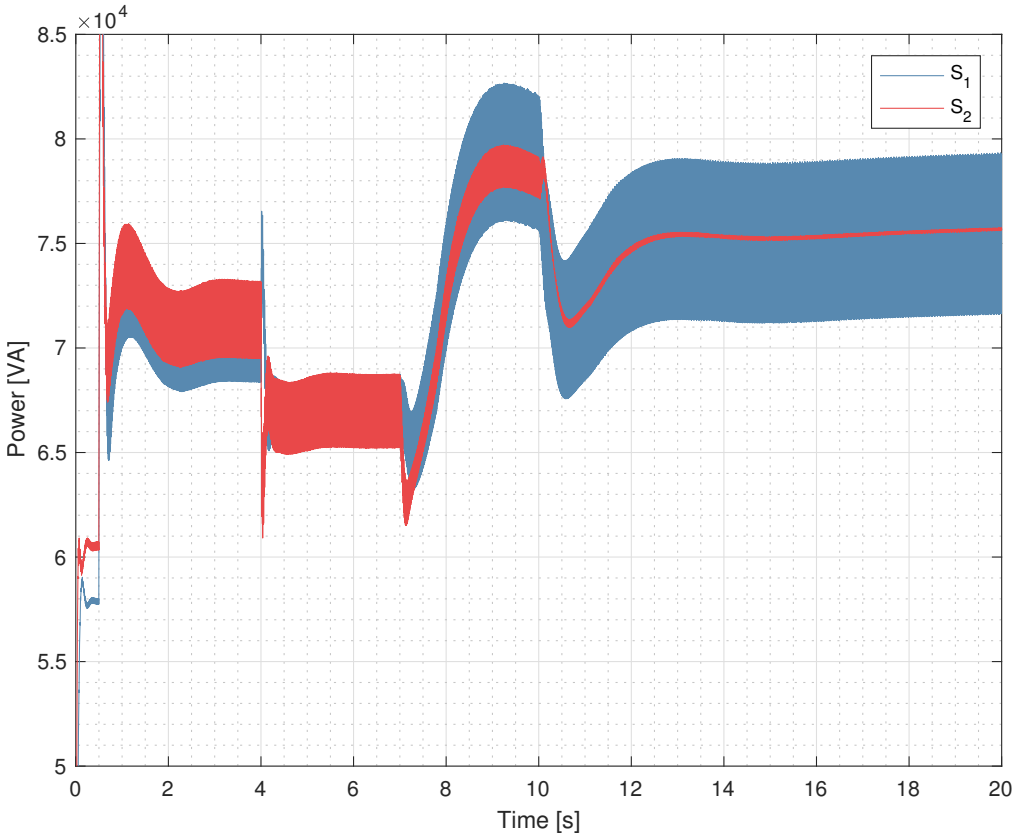

Figure 5.12: Apparent powers of both converters for case 2.

THD

Fig. 5.13 depicts the THD response of the capacitor voltage of the converters, as well as for the PCC voltage. The compensated voltage, i.e. the PCC voltage, is the main focus, but the other responses are also worth noting. Hence, they are included.

At t = 0.5 s, harmonic compensation is enabled, and the THD of the PCC voltage drops from 16.2% at t = 0.4 to 8.20% at t = 3 s. Simultaneously, the THD of the respective capacitor voltage rise to approximately 40%.

The effect is not substantially changed when the fundamental harmonic current sharing is enabled at t = 4 s. However, when the 5th harmonic current sharing is initiated at t = 7 s, a clear difference in the THD response of the capacitor voltages of the converters is observed. The THD of converter 1 increases, while the THD of converter 2 decreases. The effect is exacerbated when the 7th harmonic current sharing is enabled at t = 10 s. The final THD of these voltages is not important in this case, as the focus is on the THD of the PCC voltage. However, their response strengthens the impression made from the other KPIs, namely that the inner virtual impedance loops are not working according as intended.

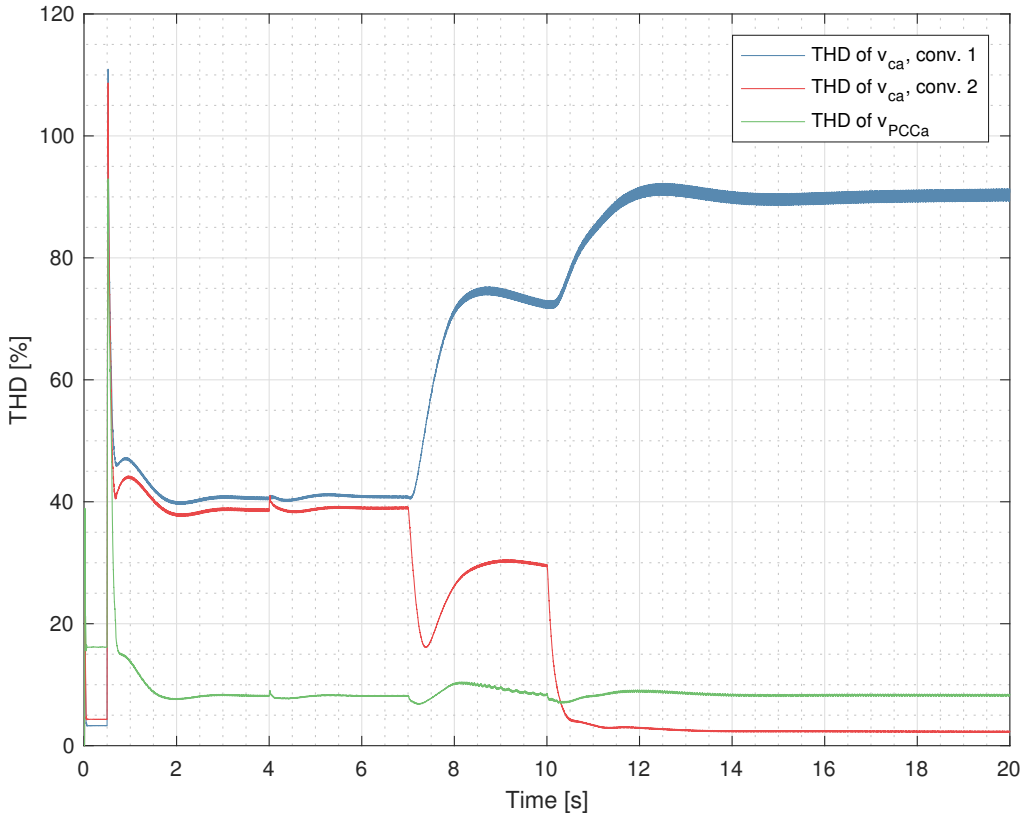

Figure 5.13: Case 2 capacitor and PCC voltage THD for both converters.

Harmonic Current Differences

Fig. 5.14 shows a clear difference in the response between the fundamental harmonic sharing and the other two. The former sharing scheme, enabled at t = 4 s, works to an extent similarly to the one observed in the two previous cases: The current sharing is improved, but not perfect. However, when the current sharing of the 5th harmonic is enabled at t = 7 s, the harmonic sharing for all three harmonic orders are aggravated. The current sharing of the 5th harmonic deteriorates the most, going from 0.2 p.u to -1.3 p.u. To clarify, this means the harmonic current supplied by converter 1 is 1.3 p.u. larger than the harmonic current supplied by converter 2. This clearly shows that the harmonic sharing for the 5th harmonic is not working.

Furthermore, approximately the same response is observed at t = 10 s, when the current sharing of the 7th harmonic component is initiated. The difference is that this initiation improves the 5th harmonic current sharing slightly.

An important aspect to notice in this result is that the harmonic sharing based on an outer virtual impedance scheme, namely the fundamental current sharing, works. It is the inner virtual impedance loops which are not compatible with the harmonic compensation of the PCC voltage, resulting in entirely undesired responses of the 5th and 7th harmonic current sharing.

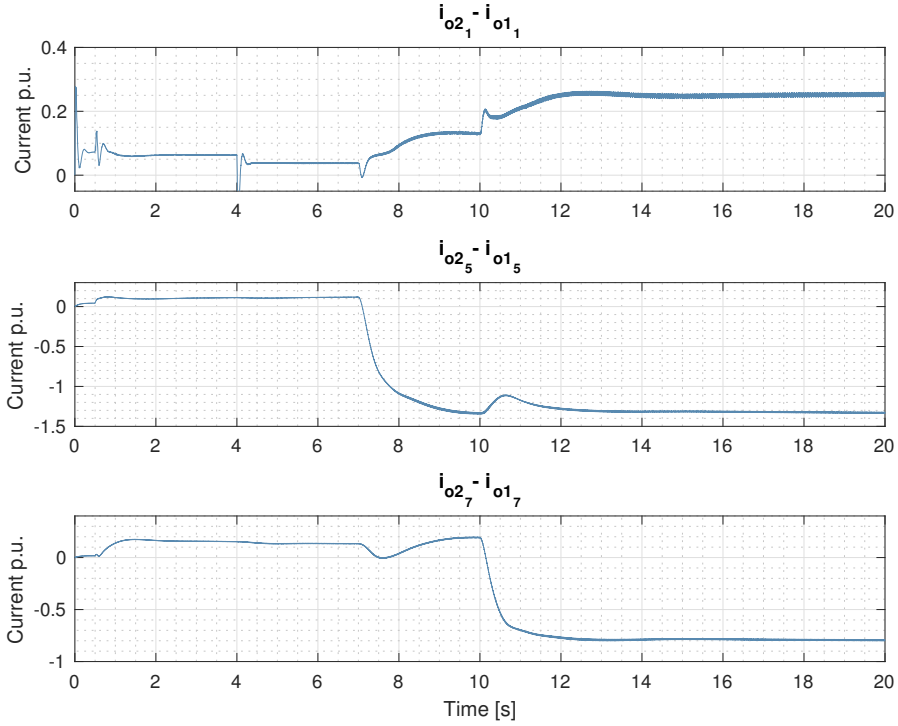

Figure 5.14: Case 2 difference in converter output current for the 1st, 5th and 7th current component.

Load Parameters

Fig. 5.10 shows a clearly unacceptable loading situation from the second the harmonic compensation is enabled at t = 0.5 s. The ripples of all three load parameters increase substantially, representing a clear operational risk to the load. Specifically, at t = 19 (steady-state), the current ripple is measured to be approximately 48.1 A, the voltage ripple is 137 V and the power ripple is 54.5 kW. Moreover, the average voltage and power is 578 V and 116 kW, respectively.

This loading situation is inadequate, and helps deduce the conclusion that moving the harmonic compensation to the PCC voltage is not possible with the current control system; measures must clearly be taken to simultaneously reduce the ripple of the load parameters.

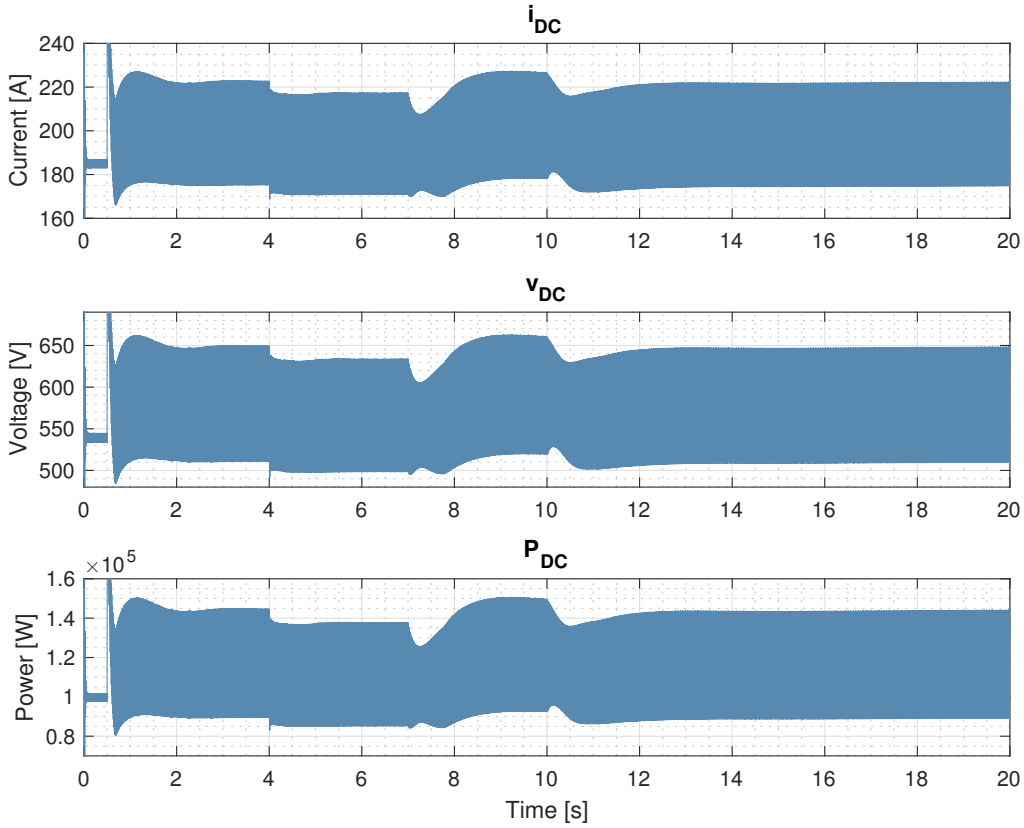

Figure 5.15: Load parameters for case 2.

Case Summary

- This case moves the harmonic compensation scheme to the PCC voltage in an effort to evaluate if this is feasible without making any additional system changes.
- The apparent powers are observed to constantly operate above their rated power, as well as containing increase ripple compared to case 1. The fundamental current sharing leads to a drop in power supplied, while the 5th and 7th harmonic sharing schemes lead to increase and decrease in the power supplied, respectively. Hence, the outer virtual impedance loop responsible for the fundamental harmonic current sharing is compatible with the system alteration, while the inner loops for the 5th and 7th current sharing are not compatible with the change.
- THD of the PCC voltage is observed to decrease from 16.2% to 8.20%. Isolated this indicates a successful implementation of PCC voltage, but as observed in the other KPIs, the system as a whole is not compatible with the alteration.
- The harmonic current differences follow the same trend as for the apparent power: The fundamental current sharing leads to better performance, while the 5th and 7th current sharing schemes exacerbate the performance, further emphasizing the incompatibility of the inner loop virtual impedance scheme with this control system alteration.
- The load parameters show the clearest signs of incompatibility with the system alteration done in this case. The voltage and power ripples are measured to be 137 V and 54.5 kW, respectively. This loading situation is inadequate, and must be improved if the system is to be compatible with PCC voltage harmonic compensation.

5.7 Case 3: Harmonic Sharing and Opposite Droop

This case investigates how an opposite droop scheme affects the performance of the harmonic sharing. A specific point to evaluate is if the opposite droop improves the fundamental harmonic sharing. In theory it should marginally improve the sharing, as explained in Section 3.5, due to the line impedance being of a mostly resistive nature. However, as stated in case 1, to achieve perfect apparent power and fundamental current sharing, a secondary control layer should be present to adjust the power references. As no such control layer is utilized in this thesis, perfect sharing is not expected for the opposite droop either.

To be able to evaluate opposite droop, it has been implemented in the simulation model according to Eq. 3.21. In addition, the droop coefficients have been tuned according to Eq. 5.1. No additional alterations have been done.

$$n = \frac{\Delta\omega}{Q_{max}} = \frac{0.01 \cdot \omega_1}{30000} = 1.04 \cdot 10^{-4} \tag{5.1a}$$

$$m = \frac{\Delta V_c}{P_{max}} = \frac{0.1 \cdot V_{Base}}{50000} = 7.68 \cdot 10^{-4} \tag{5.1b}$$

The enabling specifications are identical to the ones in case 1, shown in Table 5.3.

Apparent Powers

As observed in Fig. 5.16, the opposite droop scheme leads to a stable and responsive system. From t = 0 s to t = 1 s, only the harmonic compensation is enabled in addition to primary control. The difference between the supplied apparent power is measured to be 11.3 kVA in this time interval, substantially higher than the difference observed for the same time interval in case 1, namely 2.6 kVA. Hence, the opposite droop is more affected by uneven line impedances in terms of obtaining adequate apparent power sharing. In addition, converter 2 is measured to operate 3.75 kVA above its rating, which is more than 1.25 kVA measured in case 1.

Furthermore, when the fundamental current sharing is enabled at t = 1 s, the difference is reduced to 2.1 kVA. This is also considerably more than for case 1, where the corresponding number is approximately 0.4 VA. Thus, the opposite droop scheme has a higher need for a secondary control system eliminating this offset, than the conventional droop.

The current sharing schemes of the 5th and 7th component are initiated at t = 2 s and t = 3 s, respectively. They show a similar effect as in case 1: Decreasing the power output of both converters slightly.

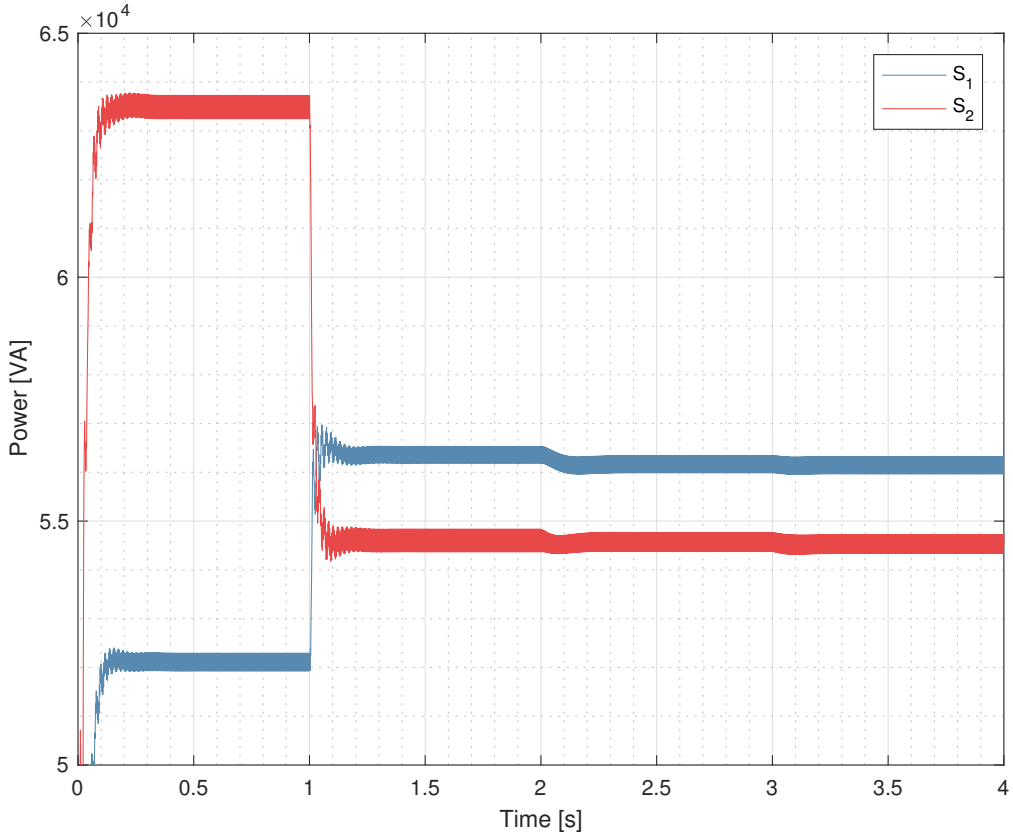

Figure 5.16: Apparent powers of both converters for case 3.

THD

THD dynamics are displayed in Fig. 5.17, showing a very similar response compared to case 1. Specifically, that the effect on the THD is marginal when the fundamental harmonic sharing is enabled at t = 1 s, but the THD of converter 2 rises when the 5th and 7th harmonic current sharing is enabled at t = 2 s and t = 3 s, respectively. Again, this is according to theory, as discussed in Section 4.4.2.

The steady state THD measured at t = 3.9 s is 1.32% for v_{ca} of converter 1, and 3.77% for v_{ca} of converter 2. These values are very similar to the corresponding numbers of case 1. That is, 1.29% and 3.97%. This quantifies the similarity to case 1, leading to the same conclusion: The THD response of the opposite droop is acceptable.

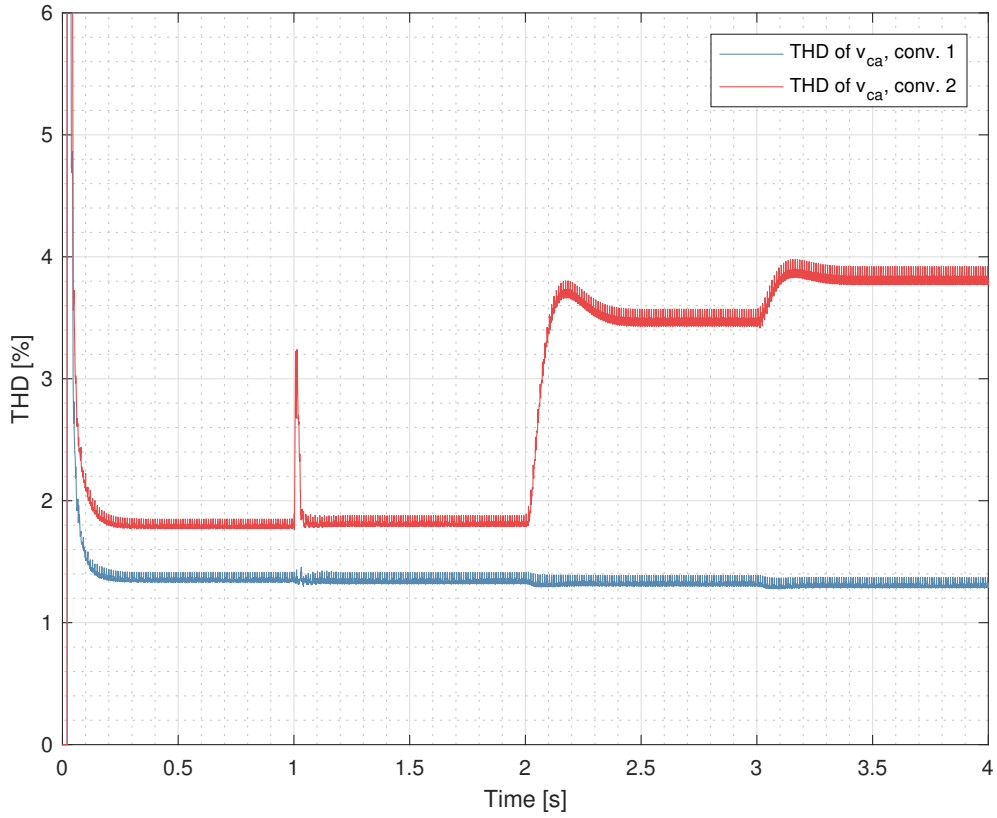

Figure 5.17: Case 3 capacitor voltage THD of phase a for both converters.

Harmonic Current Differences.

Inspecting Fig. 5.18, the harmonic current sharing responses in this case show several similarities with case 1. Nonetheless, a difference is observed in the fundamental current sharing.

During the interval of t = 0 s to t = 1 s, when only the harmonic compensation is enabled, converter 2 supplies 0.21 p.u. more than converter 1. This is considerably more than the corresponding number of 0.08 observed in case 1. When the fundamental sharing is enabled at t = 1 s, the number falls from 0.21 to. 0.013 p.u.. This number is less than the equivalent number of 0.033 p.u. in case 1, indicating that the control system acquires better fundamental harmonic sharing when implementing opposite droop rather than conventional droop. And, as mentioned, a secondary control system would help achieve perfect fundamental current sharing.

Furthermore, the 5th and 7th harmonic current sharing enabled at t = 2 s and t = 3 s, respectively, responds more or less identically with case 1: The sharing obtained is almost perfect.

Summarizing, opposite droop leads to worse fundamental current sharing than conventional droop, but the fundamental harmonic sharing scheme is also more effective. With regards to the sharing of the 5th and 7th current component, the two droops schemes show a very similar and desired response.

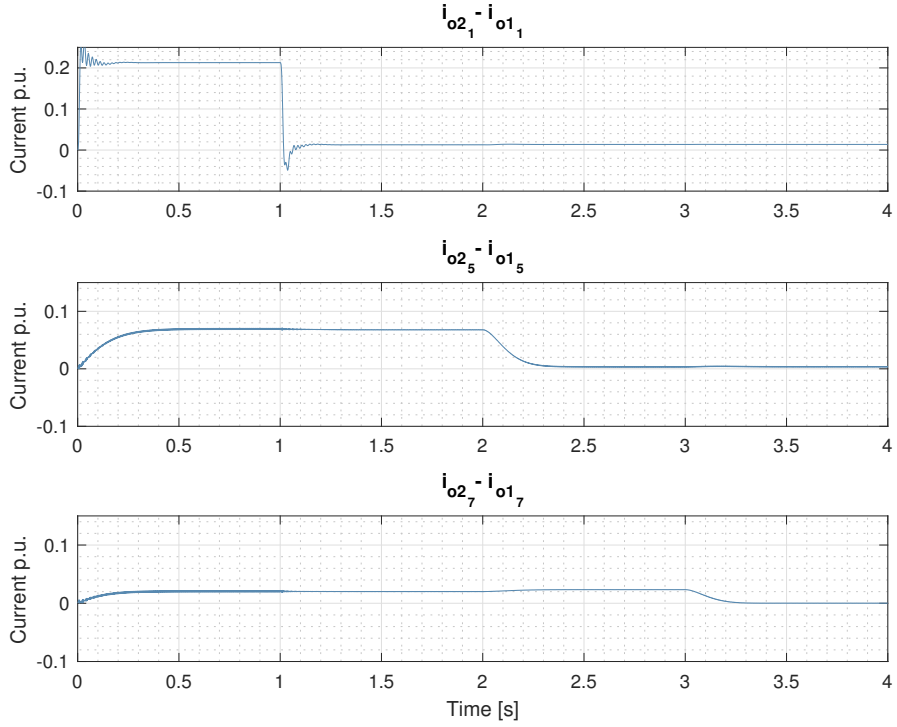

Figure 5.18: Case 3 difference in converter output current for the 1st, 5th and 7th current component.

Load Parameters.

The load parameter response of this case, shown in Fig. 5.19, also show a very similar to the results in case 1. However, some differences are present.

In the interval of t = 0 s to t = 1 s, it is observed that the voltage and power are not at their desired values of 540 V and 100 kW, respectively. Specifically, their average values are measured to be 533 V and 97.8 kW. This implies that the voltage reference would have to be adjusted slightly. The need for an adjustment is not unexpected, as the droop is now based on a P-V coupling, compared to P-f in conventional droop.

Furthermore, the voltage and power ripples are similar to the ones in case 1, namely approximately 15 V and 5 kW, respectively. They are observed to reduce slightly as the 5th and 7th harmonic sharing schemes are enabled at t = 2 s and t = 3 s, respectively, but the effect is marginal.

The assessment of the load parameter condition becomes the same as for case 1: The harmonic sharing scheme implementation preserves the desired conditions for the load parameters in a satisfying manner, also when utilizing opposite droop.

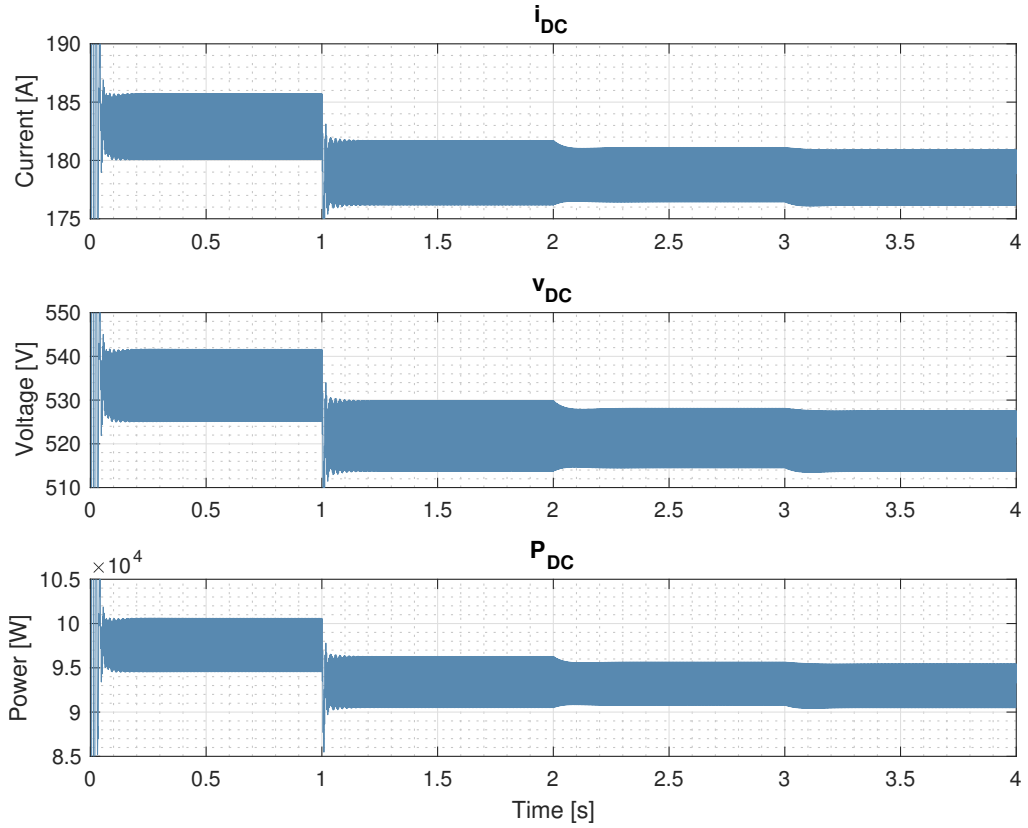

Figure 5.19: Load parameters for case 3.

Case Summary

- This case investigates how an opposite droop scheme affects the performance of harmonic sharing, and how the scheme performs compared to the conventional droop used in the other cases.

- The difference between the apparent powers is seemingly greater before any sharing is enabled, than in case 1. That is, 11.3 kVA in this case compared to 2.6 kVA. Furthermore, converter 2 operates 3.75 kVA above its rating at this point, 2.5 kVA more than in case 1, posing a larger risk to the converter in terms of overheating/damage.

  When fundamental current sharing is enabled, the sharing is improved, leading to a supply difference of 2.1 kVA. This is also more than in case 1, where the corresponding number is 0.4 kVA. The enabling of the 5th and 7th sharing decreases the supplied power from both converters marginally, similarly to what was observed for case 1.

- The THD shows a more or less identical result as case 1, where the THD was observed to rise to 3.97% for converter 2. In this case, the rise is measured to be 3.77%. Hence, only a marginal difference between the two cases.

- Harmonic current differences of the 5th and 7th harmonic are observed to be equal to case 1, while the fundamental current sharing response is different. In this case, this current difference is seen to drop from 0.21 to 0.013 p.u., compared to the corresponding numbers of 0.072 and 0.033 in case 1. Hence, the harmonic compensation leads to a worse fundamental current difference for this case than case 1, but the fundamental current scheme also shows higher efficiency than case 1.

- The load parameters are slightly below their designated values before the enabling of the harmonic sharing schemes. Furthermore, the enabling results in the same trends as observed in case 1: The fundamental current sharing leads to a higher drop in values than the 5th and 7th sharing schemes. However, the drop is not substantial, resulting in acceptable load parameter values also for this case.

5.8 Case 4: Harmonic Sharing With Additional Single-Phase Linear Load

This case studies the effect of adding a single-phase linear load between phase a and phase b. The alterations to the simulation model comprise of:

1. Reducing the power drawn by the non-linear load from 100 kW to 70 kW.
2. Adding a purely resistive load between phase a and b, set to draw 30 kW.

Hence, the total load of the system is still 100 kW, providing a suitable basis for comparison with case 1. The enabling specifications of this case can be found in Table 5.5.

Table 5.5: Enabling specifications for case 4.

t = 1 s	**t = 2 s**
Harmonic sharing schemes for all three harmonics enabled	Additional load added

Note that the droop scheme is once again of a conventional type. This makes this case identical to case 1, apart from the change in load situation.

Apparent Powers

Fig. 5.20 shows the apparent power response of this case. From t = 0 s to t = 1 s, a scenario similar to the steady-state of case 1 is observed, apart from the converters supplying less. This is expected, as the non-linear load is only drawing 70 kW at this point. The difference between their supply is measured to 2.0 kVA, less than the corresponding number in case 1, which is 2.6 kVA.

Furthermore, all harmonic sharing schemes are enabled at t = 2 s. This also leads to a similar response as seen in case 1: The sharing of the apparent power is improved, but not perfect, where the difference in sharing is measured to be approximately 0.2 kVA at t = 1.9 s.

The major change from case 1 occurs when the additional load is added at t = 3 s. In steady state, at t = 2.9 s, the average values of S_1 and S_2 are measured to be 58.5 kVA and 58.2 kVA, respectively. This yields a difference of 0.3 kVA, which means the additional load has not affected the apparent power sharing to a great extent.

However, the ripple of the apparent power of both converters are observed to increase considerably. At t = 3.9 s, the ripple of the apparent powers supplied by converter 1 and 2 are 2.3 kVA and 2.7 kVA, respectively. This indicates that the auxiliary linear load is affecting the system in a suboptimal way, as evident from the assessment of the subsequent KPIs.

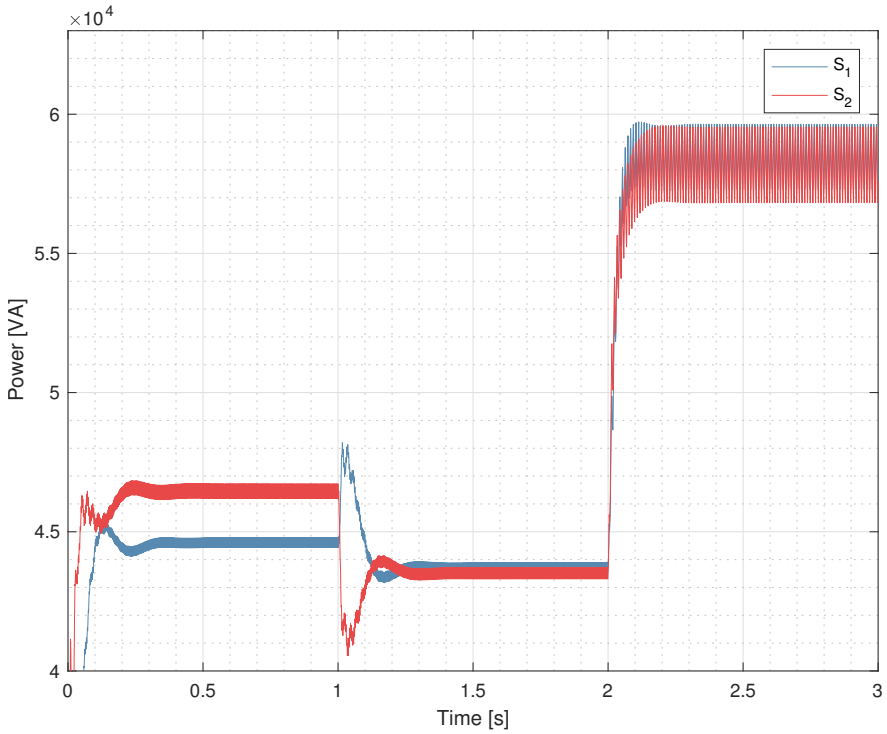

Figure 5.20: Apparent powers of both converters for case 4.

THD

The THD of the capacitor voltage is generally lower for this case, as seen in Fig. 5.21. This is expected, as the harmonic current drawn from the non-linear load now is 70 kW, compared to 100 kW in the other cases. Nonetheless, for the time interval of t = 0 s to t = 2 s, the response is similar to cases 1 and 3. The THD of converter 1 is higher than the THD of converter 2 due to the virtual impedance scheme in converter 1. That is, the trade-off between harmonic sharing and THD is evident.

At t = 2 s, when the linear load is added, the THD of converter 1 rises while the THD of converter 2 falls. Simultaneously, their ripple is reduced. Note that this is the THD of phase a, which is one of the two phases the linear load is connected between. Hence, a change is expected, and is observed in this response. The change is limited, and the overall THD response is thus regarded as acceptable, also when the linear load is added.

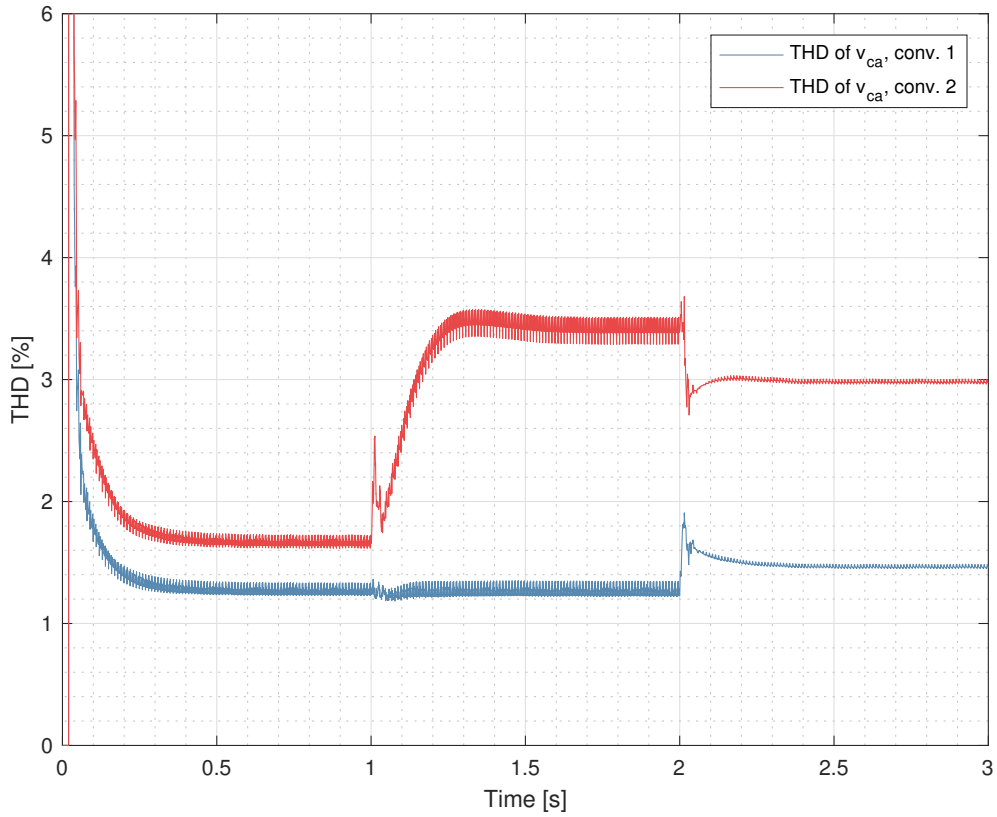

Figure 5.21: Case 4 capacitor voltage THD of phase a for both converters.

Harmonic Current Differences

Inspecting, Fig. 5.22, several trends are evident. In the interval of t = 0 s to t = 1 s, only harmonic compensation is enabled, displaying the need for harmonic sharing. At t = 1 s, the harmonic compensation is enabled, and the type of response seen in case 1-3 is again observed: The sharing of the fundamental current component is improved, but still has a constant offset from zero. Furthermore, the sharing of the 5th and 7th harmonic current component is close to perfect (zero), with a slight constant offset for the 5th. The sharing of these two components are almost entirely unaffected when the linear load is added at t = 2 s.

However, the fundamental current sharing rises when the linear load is added. As seen in the apparent power response, the power supplied by the converters rises at this point. This is equivalent to higher current drawn from the converters, which increases the impact of the uneven line impedances. That is, the converter facing the lowest line impedance, i.e. converter 1, will supply most of the linear load. Moreover, this leads to a strengthened trend of uneven fundamental current sharing, and that is what is observed when steady state conditions are acquired after t = 2 s.

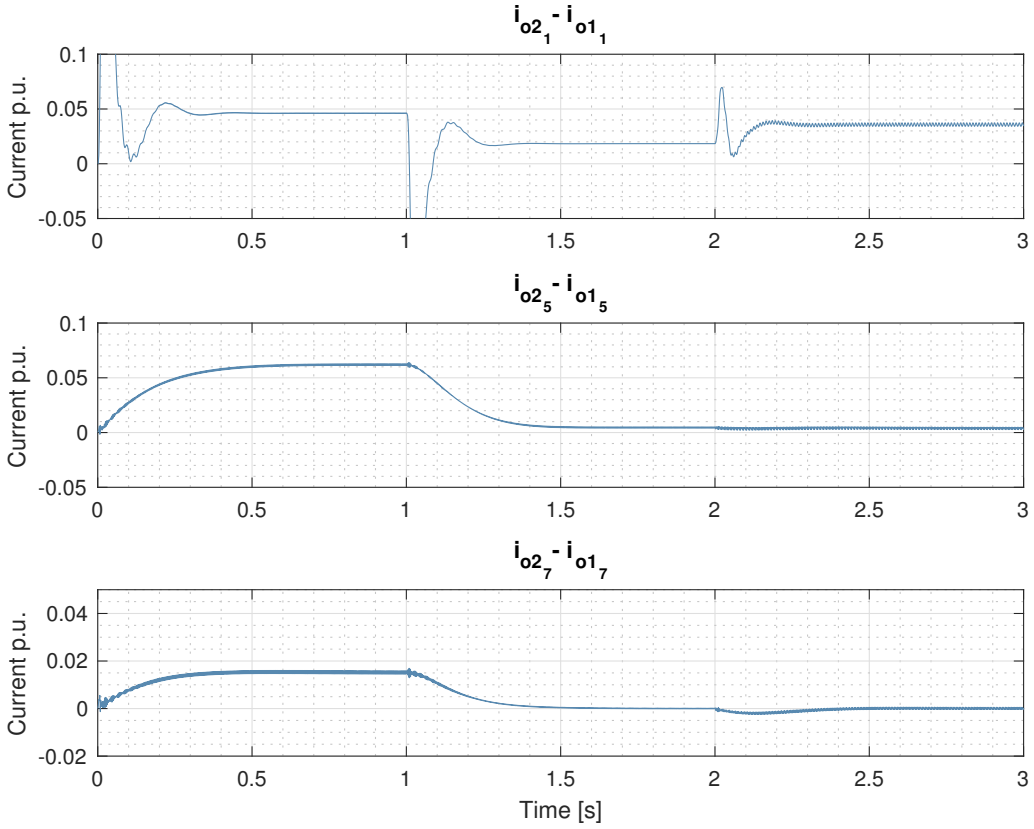

Figure 5.22: Case 4 difference in converter output current for the 1st, 5th and 7th current component.

Load Parameters

The load parameters of this case are observed in Fig. 5.23. Remark that these load parameters are still the ones of the non-linear load. During the interval of t = 0 s to t = 1 s, when only the harmonic compensation scheme is enabled, the voltage and power is measured to be 577 V and 78 kW, respectively. This is a deviation from their intended values of 540 V and 70 kW. As in the other cases, a voltage reference adjustment could mitigate this issue.

At t = 1, when the harmonic sharing is implemented, the value of all load parameters drop. As this scenario is identical to the one observed after t = 3 in case 1, observing an equal response is expected.

Moreover, when the linear load is added at t = 2 s, the ripple of all load parameters increase substantially. The ripples are measured to be 31.2 A, 131 V and 34.6 kW for the current, voltage and power respectively. This scenario is unacceptable for the load, and will lead to decreased lifetime or malfunctioning.

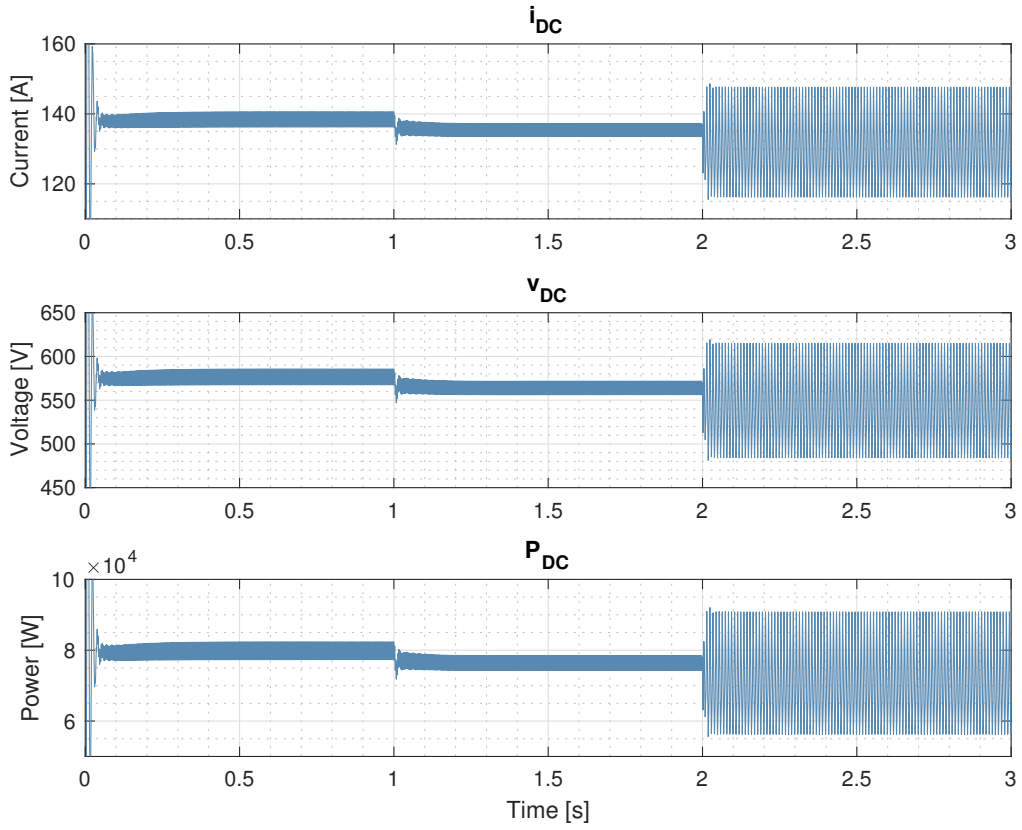

Figure 5.23: Load parameters for case 4.

Investigating the PCC voltage

To further shed light on the effect of the linear load, the PCC voltage is investigated. Fig. 5.24a shows the clear deterioration of the voltage amplitude of phases a and b, while Fig. 5.24b depicts the difference in THD that occurs when the linear load is connected at t = 2 s.

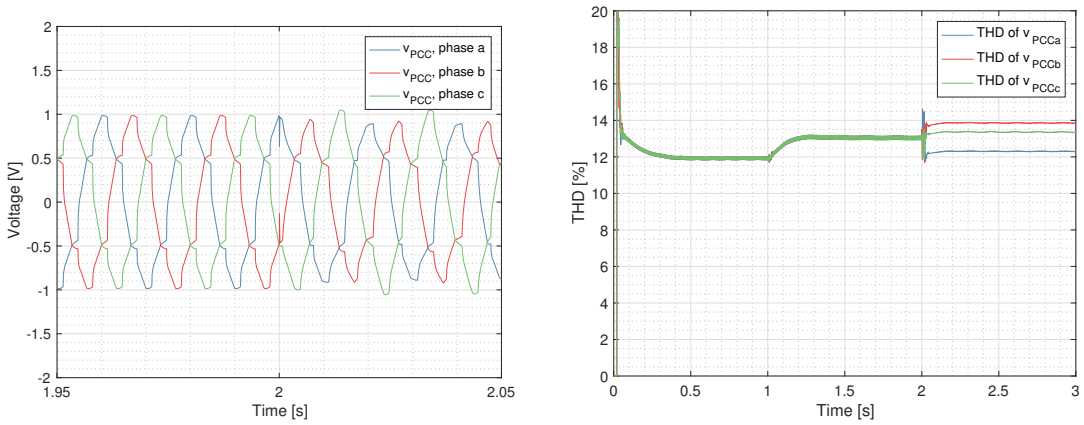

(a) PCC voltage for all three phases.

(b) THD of PCC voltage for all three phases.

Figure 5.24: The PCC voltage waveform and THD for case 4.

Moreover, investigating the FFT analysis of the PCC voltage is of interest. The harmonic spectrum before and after the addition of the linear load can be observed in Fig. 5.25. According to theory, the unbalance between the phases leads to the presence of triplen harmonics [13]. To mitigate and share the most prominent harmonic of a triplen character, namely the 3rd, an additional harmonic compensation and sharing loop could be implemented. A similar design as used for the 5th and 7th would suffice.

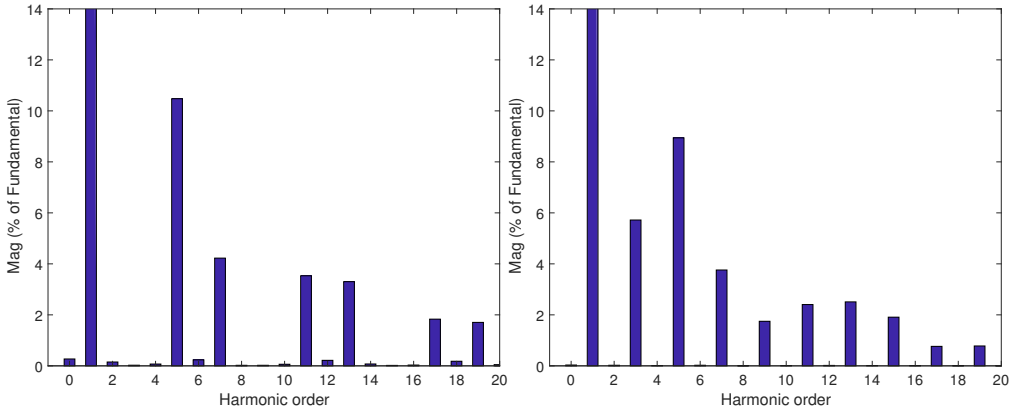

(a) Harmonic spectrum at t = 1.9 s.

(b) Harmonic spectrum at t = 2.9 s.

Figure 5.25: Harmonic spectrum of PCC voltage before and after addition of linear load.

Case Summary

- This case studies the effect of adding a single-phase linear load between phases a and b.
- The ripples of the apparent powers become 2.3 kVA and 2.7 kVA for the two converters when the linear load is added. This represents a considerable increase compared to the corresponding numbers of 0.6 and 0.4 kVA in case 1.
- The THD changes marginally when the linear load is added, and the THD response is thus regarded as acceptable for this case.
- The sharing of the 5th and 7th harmonic component is practically unaffected by the additional load, but the fundamental current sharing is slightly exacerbated. This is expected, as the fundamental current drawn increases at this point, and the impact of the uneven impedances is hence strengthened.
- The load parameters experience a considerable rise in ripple because of the addition of the linear load. The individual ripple values for the current, voltage and power are measured to be 31.2 A, 131 V and 34.6 kW, respectively. This loading situation represents an inadequate scenario for the load, resulting in the system as a whole being uncompatible with the addition of a linear load. Furthermore, the presence of a substantial third harmonic in the voltage is identified, due to unbalance of the phases. The scenario implies the demand for harmonic compensation and sharing of this harmonic if the system is to be resilient to phase imbalance.

Chapter 6

Conclusion

Harmonic distortion is a typical power quality issue in microgrids, but the inherent ability of its power electronic converters represent a cost-effective approach to mitigate the issue. However, if the line impedances of the microgrid are uneven, the converters will share the harmonic load unevenly, constituting a demand for a harmonic sharing scheme in the converter control system(s).

This master's thesis has approached this challenge by first modeling and developing a microgrid model together with the control system of its two converters. Then, the control system feasibility and its harmonic sharing scheme has been evaluated by the use of simulation results obtained in the MATLAB/Simulink environment. Furthermore, three additional cases have been explored, each one representing a distinct system alteration.

Evaluating the harmonic sharing scheme in case 1 clearly illustrated a functional scheme, able to improve all three harmonic orders evaluated. All four KPIs were satisfied, verifying the applicability of the scheme. However, the fundamental harmonic component was observed to keep a constant offset, indicating the need for a secondary control layer. Furthermore, case 2 explored harmonic compensation of the PCC voltage. The THD was found to decrease remarkably, showing a successful harmonic compensation. Nonetheless, the three remaining KPIs were not satisfied, resulting in evaluating the system as a whole to be incompatible with this system alteration. This highlights the relevance of assessing all the proposed KPIs. Case 3 investigated the use of opposite droop instead of the conventional droop utilized in the other cases. It was found that the initial difference in supplied power was worse with opposite droop, but that the fundamental current sharing proved to be more effective for this scheme. Morever, all KPIs proved to be satisfied, resulting in the control system to be deemed compatible with an opposite droop implementation. Case 4 looked at the implementation of a linear load between phases a and b at the PCC. The system's KPIs were acceptable, apart from the load parameters, where the rip-

ple increased substantially. Hence, the system as a whole was deemed uncompatible with the connection of an additional linear load at the PCC.

The obtained simulation results lead to the conclusion that the harmonic sharing scheme modeled and developed provides satisfactory responses. However, the system reduces its efficiency when substantial system alterations are implemented. Hence, improvement of the control system robustness is one of several recommendations for further work listed in the next chapter.

Chapter 7

Recommendations for Further Work

The microgrid model and its control parameters have been displayed explicitly to allow easy reproduction of the system and its results. Furthermore, several recommendations for further work has been mentioned throughout the thesis. The complete list of recommendations is given below.

1. Carrying out real-time hardware-in-the-loop simulations with the simulation model, to prove/disprove its feasibility and stability [50] in an environment representing additional fidelity [51].

2. Developing a state space model for the entire control system. This would allow a finer tuning of the harmonic compensation and ease investigation of the dynamics between the different control layers. In addition, it would allow investigating the stability boundaries of the system, in turn enriching the analysis.

3. Testing the system with only inner virtual impedance loops or only outer virtual impedance loops, and investigating the performance of the different schemes. As discussed in Sec. 4.4, transformations of the extracted harmonic values are needed to accomplish an outer virtual impedance scheme for all three harmonics, but the implementation would save computational effort and make the system more compatible with PCC voltage harmonic compensation.

4. Expanding the microgrid with more converters and more loads to evaluate interoperability. Furthermore, testing the system for fallouts of both source and load to study how resilient its system stability is in this kind of scenario.

5. Using converters with different ratings to test robustness of the droop scheme.

6. Testing the control system with different virtual impedance configurations. E.g. capacitive or negative virtual impedance, or a harmonic droop scheme [14].

7. Including a secondary layer control system. As many cases show demand for frequent voltage reference adjustment, updating the power references and/or the voltage reference by the use of a secondary control system is an area of interest. In addition the secondary control layer will help achieve better apparent power and fundamental current sharing [49].

8. Implementing harmonic compensation and sharing for the 3rd harmonic, making the system more robust against phase unbalance.

9. Testing the system when the non-linear load has an individual control system, ensuring adequate input to it, to see if the system is compatible with this type of load.

Bibliography

[1] IEA. World Energy Outlook 2017. Technical report, OECD Publishing, Paris, 2017.

[2] Ruben Buchmann. *Converter Control for Harmonic Compensation in Microgrid Applications*. Specialization project, Norwegian University of Science and Technology, 2017.

[3] Estefanía Planas, Asier Gil-de muro, Jon Andreu, Kortabarria, Inigo, and Inigo Martinez de Alegria. General aspects , hierarchical controls and droop methods in microgrids : A review. *Renewable and Sustainable Energy Reviews*, 17:147–159, 2013.

[4] Joan Rocabert, Alvaro Luna, Frede Blaabjerg, and Pedro Rodriguez. Control of Power Converters in AC Microgrids. *IEEE Transactions on Power Electronics*, 27(11):4734–4749, 2012.

[5] Chris Marnay, Spyros Chatzivasileiadis, Chad Abbey, Reza Iravani, Geza Joos, Pio Lombardi, Pierluigi Mancarella, and Jan Von Appen. Microgrid evolution roadmap. *Proceedings - 2015 International Symposium on Smart Electric Distribution Systems and Technologies, EDST 2015*, pages 139–144, 2015.

[6] Mariya Soshinskaya, Wina H.J. Crijns-Graus, Josep M. Guerrero, and Juan C. Vasquez. Microgrids: Experiences, barriers and success factors. *Renewable and Sustainable Energy Reviews*, 40:659–672, 2014.

[7] Sina Parhizi, Hossein Lotfi, Amin Khodaei, and Shay Bahramirad. State of the art in research on microgrids: A review. *IEEE Access*, 3:890–925, 2015.

[8] Farid Katiraei, Reza Iravani, Nikos Hatziargyriou, and Aris Dimeas. Microgrids Management. *IEEE Power and Energy Magazine*, 6(3):54–65, 2008.

[9] Jackson John Justo, Francis Mwasilu, Ju Lee, and Jin-Woo Jung. AC-microgrids versus DC-microgrids with distributed energy resources: A review. *Renewable and Sustainable Energy Reviews*, 24:387–405, 2013.

[10] Daniel E. Olivares, Ali Mehrizi-Sani, Amir H Etemadi, Claudio A Cañizares, Reza Iravani, Mehrdad Kazerani, Amir H Hajimiragha, Oriol Gomis-Bellmunt, Maryam Saeedifard, Rodrigo Palma-Behnke, Guillermo A. Jiménez-Estévez, and Nikos D Hatziargyriou. Trends in microgrid control. *IEEE Transactions on Smart Grid*, 5(4):1905–1919, 2014.

[11] Yun Wei Li and Jinwei He. Distribution system harmonic compensation methods: An overview of DG-interfacing inverters. *IEEE Industrial Electronics Magazine*, 8(4):18–31, 2014.

[12] Javier Roldan-Perez, Milan Prodanovic, Josep M. Guerrero, and A. Garcia-Cerrada. Finite-Gain-Current Repetitive Controller for Synchronverters with Harmonic-Sharing Capabilities. In *18th IEEE International Conference on Harmonics and Quality of Power (ICHQP)*, Ljubljana, 2018.

[13] Mehdi Savaghebi, Juan Carlos Vasquez, Alireza Jalilian, Josep M. Guerrero, and Tzung-Lin Lee. Selective Harmonic Virtual Impedance for Voltage Source Inverters with LCL filter in Microgrids. In *Energy Conversion Congress and Exposition (ECCE)*, pages 1960–1965, Raleigh, NC, USA, 2012. IEEE.

[14] Preetha Sreekumar and Vinod Khadkikar. A New Virtual Harmonic Impedance Scheme for Harmonic Power Sharing in an Islanded Microgrid. *IEEE Transactions on Power Delivery*, 31(3):936–945, 2016.

[15] Preetha Sreekumar and Vinod Khadkikar. Direct control of the inverter impedance to achieve controllable harmonic sharing in the Islanded Microgrid. *IEEE Transactions on Industrial Electronics*, 64(1):827–837, 2017.

[16] Xiongfei Wang, Yun Wei Li, Frede Blaabjerg, and Poh Chiang Loh. Virtual-impedance-based control for voltage-source and current-source converters. *IEEE Transactions on Power Electronics*, 30(12):7019–7037, 2015.

[17] Ned Mohan, Tore Marvin Undeland, and William P. Robbins. Power electronics: converters, applications, and design. chapter 8. Wiley, 3rd edition, 2003.

[18] Arkadiusz Kulka. *Sensorless Digital Control of Grid Connected Three Phase Converters for Renewable Sources*. PhD thesis, Norwegian University of Science and Technology, 2009.

[19] Anca Maria Julean. *Active Damping of LCL Filter Resonance in Grid Connected Applications*. Master thesis, Aalborg University, 2009.

[20] Block-trafo.de. Data Sheet of Line reactor LR3 (3-phase). URL: https://docs-emea.rs-online.com/webdocs/0fc4/0900766b80fc4f47.pdf. Date accessed: 2018-05-18.

[21] Stavros Papathanassiou, Hatziargyriou Nikos, and Strunz Kai. A benchmark low voltage microgrid network. *Proceedings of the CIGRE symposium: power systems with dispersed generation*, (April):1–8, 2005.

[22] Ministry of Petroleum and Energy. Forskrift om leveringskvalitet i kraftsystemet, 2004.

[23] Ewald F. Fuchs. The Roles of Filters in Power Systems. In *Power Quality in Power Systems and Electrical Machines*, chapter 9, pages 359–395. Elsevier, 2008.

[24] Dionisio Ramirez, Luis Carlos Herrero, Santiago De Pablo, and Fernando Martinez. STATCOM Control Strategies. In *Static Compensators (STATCOMs) in Power Systems*, chapter 5, pages 147–186. Springer, 2015.

[25] H. P. A. P. W. Amarajeewa, L. H. P. N. Gunawardena, B. C. Harshani, M. A. S. N. Madurawala, and D. P. Chandima. Effective Current Harmonics Mitigation at Point of Common Coupling Using Multilevel Active Front End Converter. In *Information and Automation for Sustainability (ICIAfS)*, pages 1–6, Colombo, 2014.

[26] Mehdi Savaghebi, Josep M. Guerrero, Alireza Jalilian, and Juan C. Vasquez. Mitigation of voltage and current harmonics in grid-connected microgrids. *IEEE International Symposium on Industrial Electronics*, pages 1610–1615, 2012.

[27] Juan C. Vasquez, Josep M. Guerrero, Mehdi Savaghebi, Joaquin Eloy-Garcia, and Remus Teodorescu. Modeling , Analysis , and Design of Parallel Three-Phase Voltage Source Inverters. *IEEE Transactions on Industrial Electronics*, 60(4):1271–1280, 2013.

[28] R. H. PARK. Two-Reaction Theory of Synchronous Machines: Generalized Method of Analysis-Part I. *Transactions of the American Institute of Electrical Engineers*, 48(3):716–727, 1929.

[29] Miguel Ochoa-Giménez, Javier Roldán-Pérez, Aurelio García-Cerrada, and Juan Luis Zamora-Macho. Space-vector-based controller for current-harmonic suppression with a shunt active power filter. *EPE Journal (European Power Electronics and Drives Journal)*, 24(2):50–58, 2014.

[30] Adrian Timbus, Marco Liserre, Remus Teodorescu, Pedro Rodriguez, and Frede Blaabjerg. Evaluation of Current Controllers for Distributed Power Generation Systems. *IEEE Transactions on Power Electronics*, 24(3):654–664, 2009.

[31] Roy Nilsen. Controllers and Filtering. In *TET4120 Electric Drives Compendium*, chapter 3, page 105. Department of Electric Power Engineering, Norwegian University of Science and Technology, 2018.

[32] Santiago Sanchez, Gilbert Bergna, and Elisabetta Tedeschi. Tuning of control loops for grid-connected Modular Multilevel Converters under a simplified port representation for large system studies. *2017 12th International Conference on Ecological Vehicles and Renewable Energies, EVER 2017*, (3), 2017.

[33] Jens Balchen, Bjarne A. Foss, and Trond Andresen. *Reguleringsteknikk*. Institutt for teknisk kybernetikk, Trondheim, 5th edition, 2003.

[34] Josep M. Guerrero, Poh Chiang Loh, Tzung Lin Lee, and Mukul Chandorkar. Advanced control architectures for intelligent microgrids; Part II: Power quality, energy storage, and AC/DC microgrids. *IEEE Transactions on Industrial Electronics*, 60(4):1263–1270, 2013.

[35] A. Tuladhar, H. Jin, T. Unger, and K. Mauch. Parallel operation of single phase inverter modules with no control interconnections. *Proceedings of APEC 97 - Applied Power Electronics Conference*, 1:94–100, 1997.

[36] Shivkumar V. Iyer, Madhu N. Belur, and Mukul C. Chandorkar. A generalized computational method to determine stability of a multi-inverter microgrid. *IEEE Transactions on Power Electronics*, 25(9):2420–2432, 2010.

[37] Nagaraju Pogaku, Milan Prodanović, and Timothy C. Green. Modeling, analysis and testing of autonomous operation of an inverter-based microgrid. *IEEE Transactions on Power Electronics*, 22(2):613–625, 2007.

[38] R Teodorescu, F Blaabjerg, M Liserre, and P C Loh. Proportional-resonant controllers and filters for grid-connected voltage-source converters. *IEE Proceedings - Electric Power Applications*, 153(5), 2006.

[39] Salvatore D'Arco, Miguel Ochoa-Gimenez, Luigi Piegari, and Pietro Tricoli. Harmonics and interharmonics compensation with active front-end converters based only on local voltage measurements. *IEEE Transactions on Industrial Electronics*, 64(1):796–805, 2017.

[40] Xiongfei Wang, Frede Blaabjerg, and Zhe Chen. Autonomous Control of Inverter - Interfaced Distributed Generation Units for Harmonic Current Filtering and Resonance Damping in an Islanded Microgrid. *IEEE Transactions on Industry Applications*, 50(1):452–461, 2014.

[41] Jinwei He, Yun Wei Li, and Frede Blaabjerg. An Enhanced Islanding Microgrid Reactive Power, Imbalance Power, and Harmonic Power Sharing Scheme. *IEEE Transactions on Power Electronics*, 30(6):3389–3401, 2015.

[42] Josep M Guerrero, José Matas, Luis García De Vicuña, Miguel Castilla, and Jaume Miret. Wireless-Control Strategy for Parallel Operation of Distributed-Generation Inverters. *IEEE Transactions on Industrial Electronics*, 53(5):1461–1470, 2006.

[43] C. H. Ng, L. Ran, G. A. Putrus, and K. Busawan. A new approach to real time individual harmonic extraction. In *Proceedings of the International Conference on Power Electronics and Drive Systems*, volume 1, pages 825–829, 2003.

[44] Ned Mohan. *Advanced Electric Drives: Analysis, Control and Modeling using Simulink*. MNPERE, Minneapolis, Minesota, year 2001 edition, 2001.

[45] José Matas, Miguel Castilla, Luis García de Vicuña, Jaume Miret, and Juan Carlos Vasquez. Virtual Impedance Loop for Droop-Controlled Single-Phase Parallel Inverters Using a Second-Order General-Integrator Scheme. *IEEE Transactions on Power Electronics*, 25(12):2993–3002, 2010.

[46] Mehdi Savaghebi, Alireza Jalilian, Juan C Vasquez, and Josep M Guerrero. Secondary Control for Voltage Quality Enhancement in Microgrids. *IEEE Transactions on Smart Grid*, 3(4):4799, 2012.

[47] Edson H. Watanabe, Richard M. Stephan, and Mauricio Aredes. New concepts of instantaneous active and reactive powers in electrical systems with generic loads. *IEEE Transactions on Power Delivery*, 8(2):697–703, 1993.

[48] Jianguo Zhou, Sunghyok Kim, Huaguang Zhang, Qiuye Sun, and Renke Han. Consensus-based Distributed Control for Accurate Reactive, Harmonic and Imbalance Power Sharing in Microgrids. *IEEE Transactions on Smart Grid*, XX(XX):1–1, 2016.

[49] Yang Han, Hong Li, Pan Shen, Ernane Antônio Alves Coelho, and Josep M. Guerrero. Review of Active and Reactive Power Sharing Strategies in Hierarchical Controlled Microgrids, mar 2017.

[50] J M Guerrero, M Chandorkar, T Lee, and P C Loh. Advanced Control Architectures for Intelligent Microgrids; Part I: Decentralized and Hierarchical Control. *Industrial Electronics, IEEE Transactions on*, 60(4):1254–1262, 2013.

[51] R P Rekha and E R Limpaecher. Development of a Real-Time Hardware- in-the-Loop Power Systems Simulation Platform to Evaluate Commercial Microgrid Controllers. (February), 2016.

Appendix A

Supporting Material

A.1 Filter Transfer Functions

The transfer functions for the L, LC and LCL filter are given in this section.

A.1.1 L Filter

$$G_L(s) = \frac{i_o}{v_{in}} = \frac{1}{sL_1 + R} \tag{A.1}$$

A.1.2 LC Filter

Note that the capacitor parasitic resistance is omitted.

$$G_{LC}(s) = \frac{v_c}{v_{in}} = \frac{1}{s^2LC + sCR + 1} \tag{A.2}$$

A.1.3 LCL Filter

$$G_{LCL}(s) = \frac{i_o}{v_{in}} = \frac{1}{s^3L_1L_2C + s^2C(L_2R_{L1} + L_1R_{L2} + s(L_1 + L_2 + CR_{L1}R_{L2} + R_{L1} + R_{L2}) + R_{L1} + R_{L2}} \tag{A.3}$$

A.2 Primary Current Transformation

Using KVL on Fig. 3.3, the starting equation is:

$$\vec{v}_i^{abc} = L_1\frac{d\vec{i}_i^{abc}}{dt} + \vec{i}_i^{abc}R_{L_1} + \vec{v}_c^{abc} \tag{A.4}$$

Equation A.4 is identical in the $\alpha\beta$-frame:

$$\vec{v}_i^{\alpha\beta} = L_1 \frac{d\vec{i}_i^{\alpha\beta}}{dt} + \vec{i}_i^{\alpha\beta} R_{L_1} + \vec{v}_c^{\alpha\beta} \tag{A.5}$$

The relation between $\alpha\beta$ and dq is:

$$x^{\alpha\beta} = x^{dq} e^{-j\omega x} \tag{A.6}$$

Concequently, using the chain rule, Eq. A.4 in the SRF is:

$$\vec{v}_i^{dq} = L_1 \frac{d\vec{i}_i^{dq}}{dt} + \vec{i}_i^{dq} R_{L_1} - j\omega L \vec{i}_i^{dq} + \vec{v}_c^{dq} \tag{A.7}$$

Transforming to per unit quantities and treating both axes separately, yields:

$$\vec{v}_{i,pu}^{d} = \frac{L_{1,pu}}{\omega_{Base}} \frac{d\vec{i}_{i,pu}^{d}}{dt} + \vec{i}_{i,pu}^{d} R_{L_1,pu} - \omega_{pu} L_{1,pu} \vec{i}_{i,pu}^{q} + \vec{v}_{c,pu}^{d} \tag{A.8a}$$

$$\vec{v}_{i}^{q,pu} = \frac{L_{1,pu}}{\omega_{Base}} \frac{d\vec{i}_{i,pu}^{q}}{dt} + \vec{i}_{i,pu}^{q} R_{L_1,pu} + \omega_{pu} L1, pu \vec{i}_{i,pu}^{d} + \vec{v}_{c,pu}^{q} \tag{A.8b}$$

Subsequently transforming into the Laplace domain and rearranging gives the form illustrated in Fig. 3.4:

$$\vec{i}_{i,pu}^{d} = \left(\vec{v}_{i,pu}^{d} - \vec{v}_{c,pu}^{d} + \omega_{pu} L_{1,pu} \vec{i}_{i,pu}^{q} \right) \left(\frac{\frac{w_{Base}}{L_{1,pu}}}{s + \frac{R_{L1,pu}\omega_{Base}}{L_{1,pu}}} \right) \tag{A.9a}$$

$$\vec{i}_{i,pu}^{q} = \left(\vec{v}_{i,pu}^{q} - \vec{v}_{c,pu}^{q} - \omega_{pu} L_{1,pu} \vec{i}_{i,pu}^{d} \right) \left(\frac{\frac{w_{Base}}{L_{1,pu}}}{s + \frac{R_{L1,pu}\omega_{Base}}{L_{1,pu}}} \right) \tag{A.9b}$$

A.3 Primary Voltage Transformation

Using KCL on Fig. 3.3, the starting equation is:

$$\vec{i}_i^{abc} = \vec{i}_o^{abc} + \vec{i}_c^{abc} \tag{A.10}$$

Equation A.10 is identical in the $\alpha\beta$-frame:

$$C\frac{d\vec{v}_c^{\alpha\beta}}{dt} = \vec{i}_i^{\alpha\beta} + \vec{i}_o^{\alpha\beta} \tag{A.11}$$

The relation between $\alpha\beta$ and dq is:

$$x^{\alpha\beta} = x^{dq}e^{-j\omega x} \tag{A.12}$$

Concequently, using the chain rule, Eq. A.10 in the SRF is:

$$C\frac{d\vec{v}_c^{dq}}{dt} - j\omega C\vec{v}_c^{dq} = \vec{i}_o^{dq} + \vec{i}_c^{dq} \tag{A.13}$$

Transforming to per unit quantities and treating both axes separately, yields:

$$C\frac{d\vec{v}_c^{d}}{dt} - \omega C\vec{v}_c^{q} = \vec{i}_o^{d} + \vec{i}_c^{d} \tag{A.14a}$$

$$C\frac{d\vec{v}_c^{q}}{dt} + \omega C\vec{v}_c^{d} = \vec{i}_o^{q} + \vec{i}_c^{q} \tag{A.14b}$$

Subsequently transforming into the Laplace domain and rearranging gives the form illustrated in Fig. 3.6:

$$\vec{v}_{c,pu}^{d} = \left(\vec{i}_{i,pu}^{d} - \vec{i}_{o,pu}^{d} + \vec{v}_{c,pu}^{q}\omega_{pu}C_{pu}\right)\left(\frac{\omega_{Base}}{sC_{pu}}\right) \tag{A.15a}$$

$$\vec{v}_{c,pu}^{q} = \left(\vec{i}_{i,pu}^{q} - \vec{i}_{o,pu}^{q} + \vec{v}_{c,pu}^{d}\omega_{pu}C_{pu}\right)\left(\frac{\omega_{Base}}{sC_{pu}}\right) \tag{A.15b}$$

Appendix B

Per Unit System

It is practical to convert the system parameters into per unit values. This is done using the following base quantities:

$$V_{Base} = \frac{\sqrt{2}}{\sqrt{3}} V_{LL}, \quad I_{Base} = \sqrt{2} I_N, \quad Z_{Base} = \frac{V_{Base}}{I_{Base}}, \quad S_{Base} = \frac{3}{2} V_{Base} I_{Base} \tag{B.1}$$

Note that I_N is the nominal RMS current and V_{LL} is the line-to-line voltage. The given impedance quantity also implies frequency dependence, as shown in Eq. B.2.

$$L_{Base} = \frac{Z_{Base}}{\omega_{Base}}, \quad C_{Base} = \frac{1}{\omega_{Base} Z_{Base}} \tag{B.2}$$

Appendix C

MATLAB® Code

In this appendix, example MATLAB code for running the simulink model used for case 1 is provided.

```
%% Simulation Values
Ts = 5e-5;% Simulation step

%% Enabling and step times

%Enabling
enableHC = 1;
enableVI = 1
enableVI_5 = 1;
enableVI_7 = 1;

%Steptimes
StepTime_HC = 0;
StepTime_VI_1 = 1;
StepTime_VHI = 2; %vi5
StepTime_VHI7 = 3;

%% Base values
v_line2line = 470;
voltageBase = sqrt(2/3)*v_line2line;
S_Base = 60000;
currentBase = 2/3*S_Base/voltageBase;
impedanceBase = voltageBase/currentBase;
wBase = 2*pi*50;
L_Base = impedanceBase/wBase;
C_Base = 1/(wBase*impedanceBase);
```

```
fsw = 6000; %switching frequency
Vdc = 750; %Converter DC voltage

%% Impedances

%L1C
filterInductor = 500e-6;
filterCapacitor = 50e-6;
filterResistor = 6e-3;

%L1
X_L1 = filterInductor*wBase;
X_L1pu = X_L1/impedanceBase

%L2
filterInductor2 = 200e-6;
filterResistor2 = 0.8e-3;

%LCL Filter
L_pu = filterInductor/L_Base;
L2_pu = filterInductor2/L_Base;
R_pu = filterResistor/impedanceBase;
R2_pu = filterResistor2/impedanceBase;
C_pu = filterCapacitor/C_Base;

%% Power References for each inverter
P_ref_1 = 55000;
Q_ref_1 = 22000;
P_ref_2 = 55000;
Q_ref_2 = 22000;

%% Current controller

%Based on pole placement, using the approach in "Tuning of control loops
%for grid-connected..." by Santiago et. al.

%The dominant pole has L/R as time constant
a_plant = wBase*R_pu/L_pu;
c_plant = wBase/L_pu; %Dominant pole given by c/(s+a)
%Calculate the small time constant based on fsw
T_small = 0.5*(1/fsw);
w_0i = 2*pi*fsw/10;%1/10 of the switching frequency
```

```
rho = 1.1; %Chosen > 1 to get a well damped system.
Kp_i = (2*rho*w_0i - a_plant)/c_plant;
Ki_i = ((w_0i)^2)/c_plant;

%Bode plots
s = tf('s');
cPlant = c_plant/(s + a_plant)*1/(1+s*T_small);
cPI = Kp_i + Ki_i/s;
c_openLoop = cPlant*cPI;
margin(c_openLoop)

%% Voltage controller

b_plant = wBase/C_pu;
w_0v = w_0i/10; %Bandwidth of the voltage controller
rho_v = 1;
Kp_v = 2*rho_v*w_0v/b_plant;
Ki_v = w_0v^2/b_plant;
T_eq = 1/w_0i

%Bode plots
s = tf('s');
vPlant = b_plant/(s)*1/(1+s*T_eq);
vPI = Kp_v + Ki_v/s;
v_openLoop = vPlant*vPI;
margin(v_openLoop)

%% Droop Coefficients
m = 0.5*2*pi/50000;%0.5 Hz change after a load change of 50000 W.
n = 0.1*voltageBase/30000;% 10% change in voltage when Q is changed with 30000 VAr.
powerFilterBandwidth = w_0v/10;
powerFilterTimeConstant = 1/powerFilterBandwidth;

%% Line impedances
%CIGRE: nr. 3: 4*50 (3*50), Rph = .397, Xph = .279
R_line_inv_1 = 0.397*1.2;
R_line_inv_2 = 0.397*0.8;

X_line_inv_1 = 0.279*1.2;
X_line_inv_2 = 0.279*0.8;

L_line_inv_1 = X_line_inv_1/wBase;
```

```
111 L_line_inv_2 = X_line_inv_2/wBase;
112
113 L_line_inv_1_pu = L_line_inv_1/L_Base;
114 L_line_inv_2_pu = L_line_inv_2/L_Base;
115
116 rPU1 = R_line_inv_1/impedanceBase;
117 rPU2 = R_line_inv_2/impedanceBase;
118 xPU1 = X_line_inv_1/impedanceBase;
119 xPU2 = X_line_inv_2/impedanceBase;
120
121 R_h = (L_pu + rPU1 + xPU1 + L2_pu)/(L_pu + rPU2 + xPU2 + L2_pu);
122
123 %% Load parameters
124 C_L = 1500e-6;
125 L_L = 0.12e-3;
126 R_LL = 0.520e-3;
127
128 %% Harmonic PI parameters
129 Kp_v5 = 150;
130 Ki_v5 = 10;
131
132 Kp_v7 = 150;
133 Ki_v7 = 10;
134
135 LPF_harm = 10; %Bandwidth
136
137 %% Virtual Impedances
138 r_pu_VI = (rPU1-rPU2);
139 L_pu_VI = (L_line_inv_1_pu-L_line_inv_2_pu);
140 VI_timeConstant = 0.1;
```

Appendix D

Simulink Diagrams

The following subsections contain the Simulink model diagrams needed to reproduce the model. In Section D.1, the complete simulink model is presented. In addition, the components of the microgrid is highlighted, as well as the subsystems containing the different parts of the control systems. The subsequent sections in this appendix display the insides of these subsystems. Namely, the primary current and voltage control subsystem structures are shown in sections D.2 and D.3, respectively. The droop control subsystem is shown in Section D.4. Moreover, the harmonic compensation subsystem structure is shown in Section D.5, while the harmonic sharing subsystem structure is located in Section D.6.

D.1 Complete Model

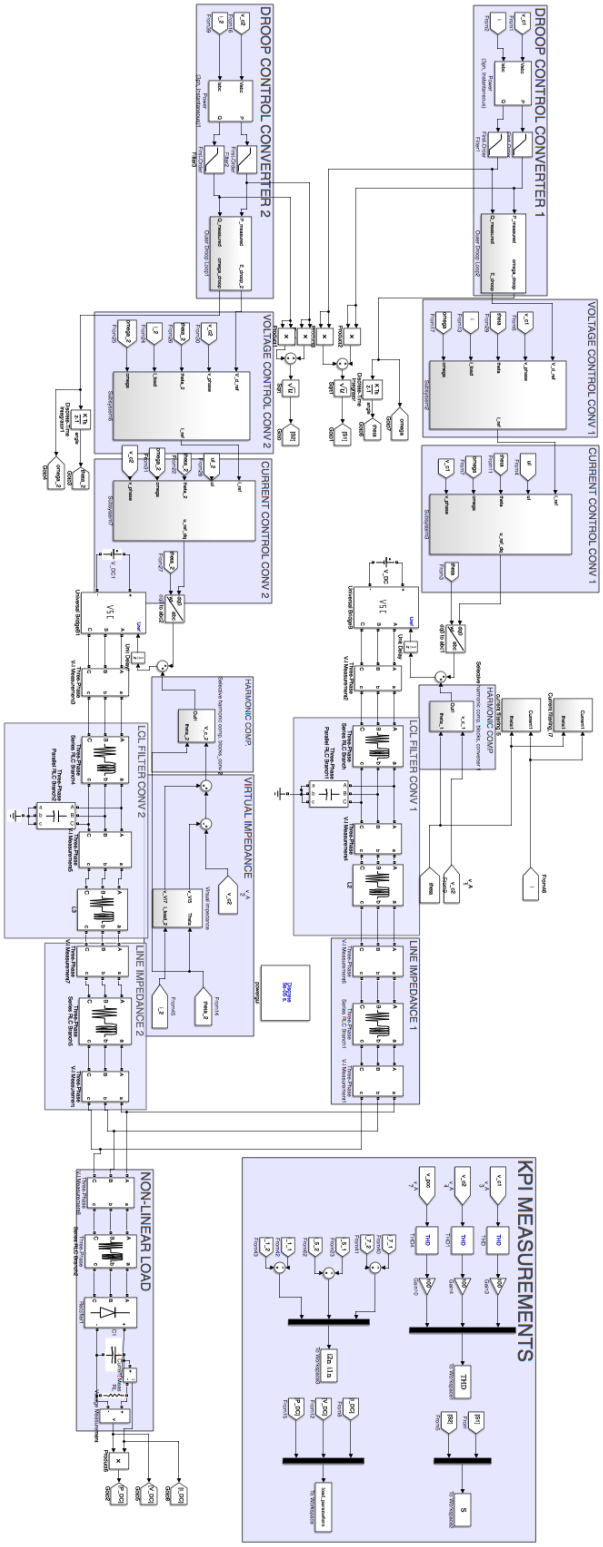

Figure D.1: An overview of the Simulink model.

D.2 Primary Current Control Model

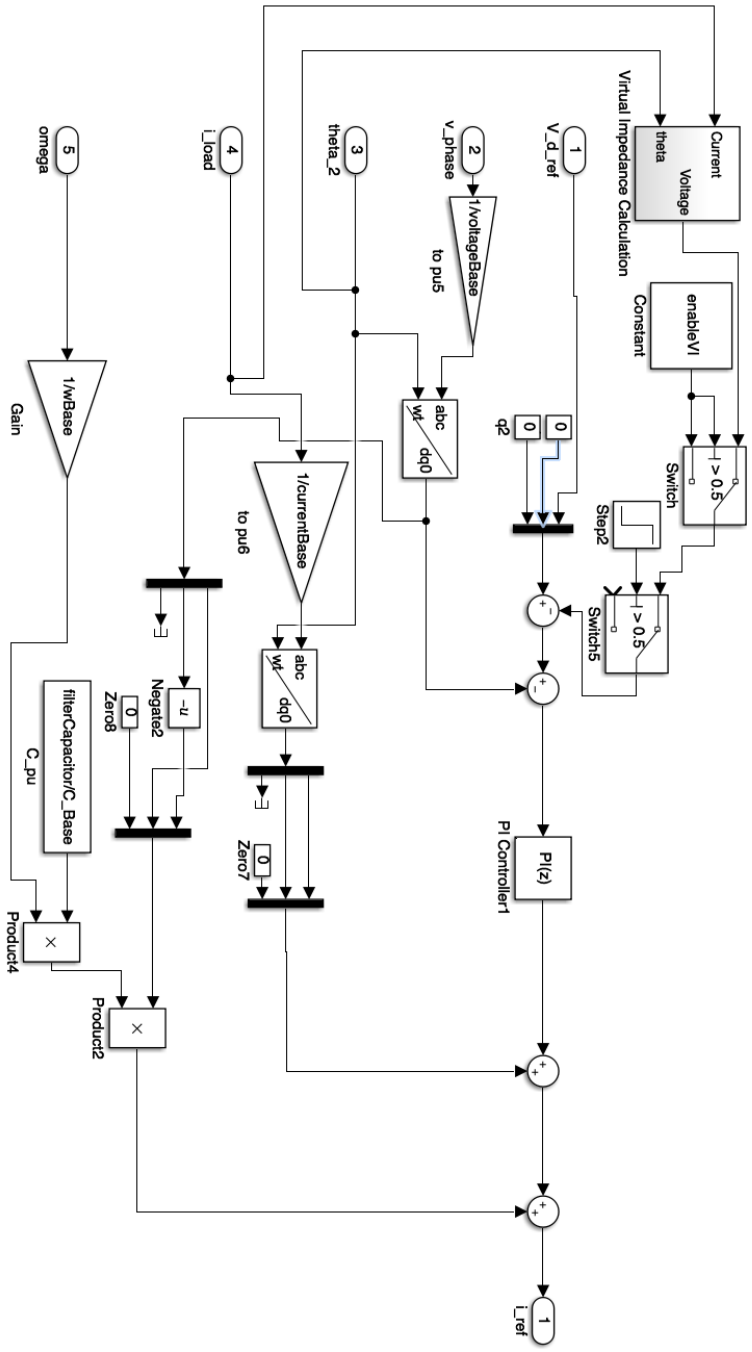

Figure D.2: The primary current control subsystem structure.

D.3 Primary Voltage Control Model

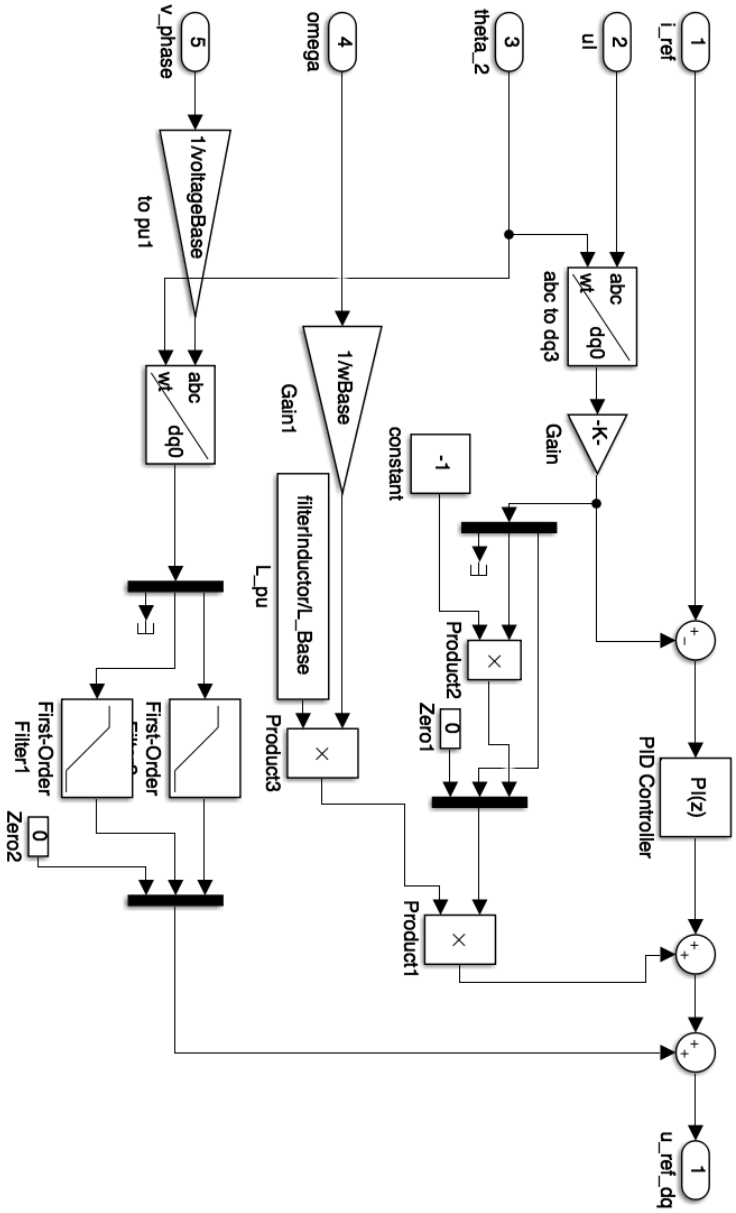

Figure D.3: The primary voltage control subsystem structure.

D.4 Droop Control Model

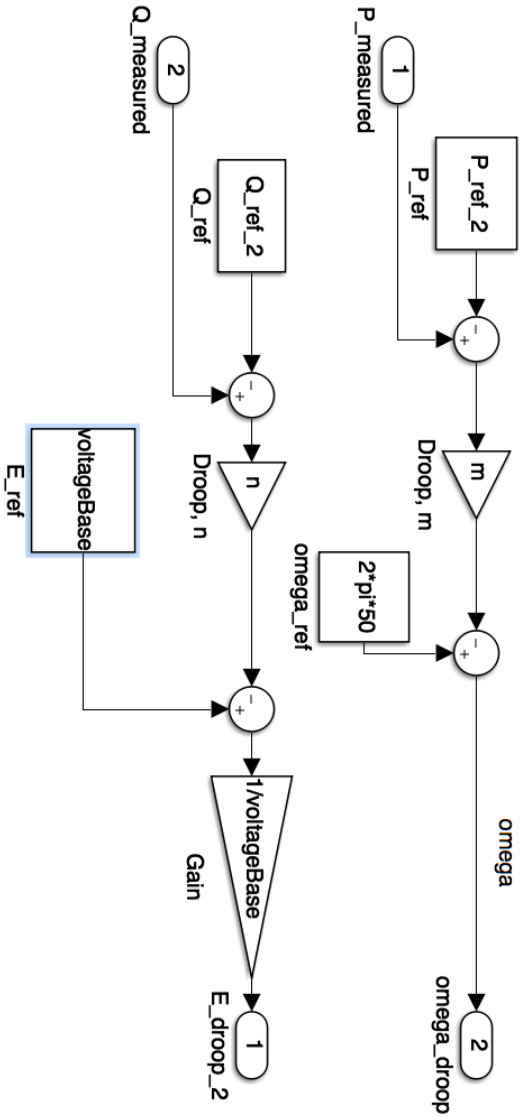

Figure D.4: The droop control subsystem structure.

D.5 Harmonic Compensation Model

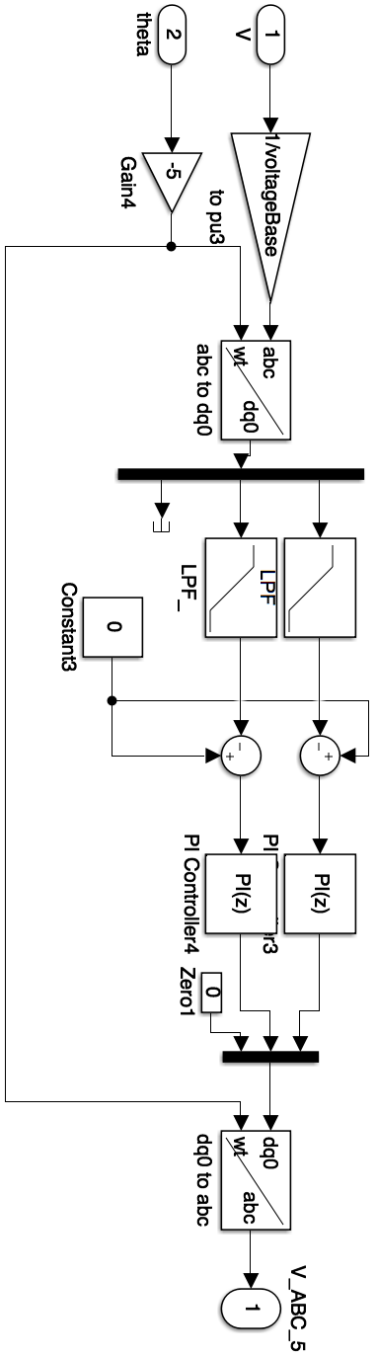

Figure D.5: The harmonic compensation subsystem structure.

D.6 Harmonic Sharing Model

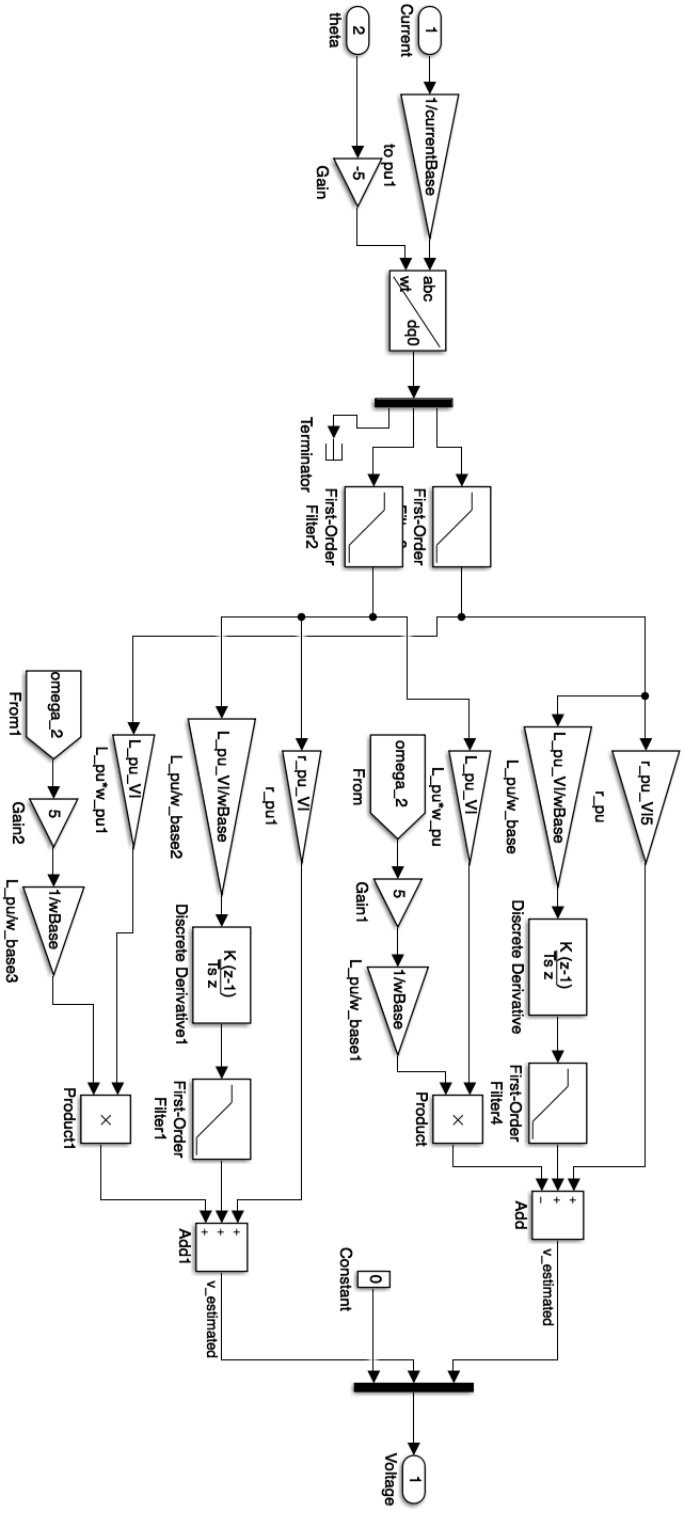

Figure D.6: The virtual impedance subsystem structure.

Appendix E

Excerpt From Specialization Project

The following document is an excerpt from the specialization project the author wrote in the fall of 2017. The excerpt is collected in its entirety from [2].

2 State-of-the-Art of Microgrids

This chapter will supply a definition of microgrids, explain the standard elements that comprise a microgrid, shortly look at both island and grid connected modes of operation, delve into control methods for microgrid operation and also provide an overview of benefits and disadvantages in the field of microgrids.

2.1 Definition

The concept of microgrids was introduced in the technical literature in [7] and [8] as a means to overcome several emerging challenges related to the integration of distributed generation. These challenges include the increase of power electronic interfaces and control of these, but also barriers regarding new economical models and regulatory issues [7]. Since then, microgrids have been subject to much research, with a rising interest in recent years due to its ability to integrate intermittent energy sources such as solar into the grid.

There is no single definition in relevant literature of what a microgrid is. Several variations exist, but the one established by the Conseil International des Grandes Réseaux Électriques (CIGRÉ) will be used for further exploration of the microgrid concept:

> *Microgrids are electricity distribution systems containing loads and distributed energy resources, (such as distributed generators, storage devices, or controllable loads) that can be operated in a controlled, coordinated way either while connected to the main power network or while islanded* [9].

This definition indirectly establishes the inherent flexibility of microgrids, as all the Distributed Energy Resources (DERs) mentioned can provide fast response in case of e.g. grid instability, power outage, power shortage and overproduction.

It should also be emphasized that the microgrid structure is deployed on the distribution level of the electricity transmission system, i.e. at a low voltage level. IEC 60038:2009 defines low voltage (LV) as 1000 V and under for AC systems [10]. Hence, this voltage interval is most relevant for microgrids.

Also note that the CIGRÉ definition sets no defined time scale for island operation, but supplements their definition by stating that a microgrid should be able to work in island mode for more than a few minutes [9].

Figure 4 illustrates the microgrid concept additionally and provides a reference for the elaboration of its components following in the next Section. The AC bus of this illustration is directly connected to residential loads, reflected in the line to line voltage of 400 V of the AC bus.

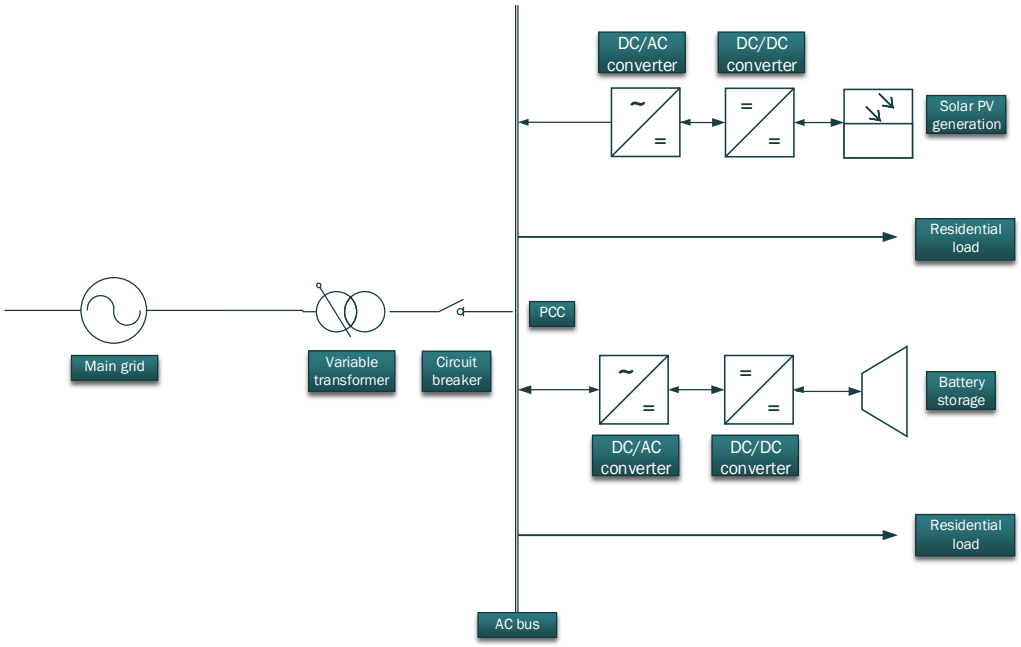

Figure 4: A basic microgrid consisting of generation, storage and loads.

2.2 Standard Elements

Referring to the definition given in the previous chapter, the components comprising a microgrid are given in this Section. The reader is advised to use Fig. 4 for illustrative purposes.

2.2.1 Distributed Energy Resources

DERs in the context of microgrids can be viewed as a common term for all small-scale entities capable of supplying power. This means that DERs includes storage systems capable of supplying power. The term is often divided into two subordinate terms, namely Distributed Generation (DG) and Energy Storage Systems (ESSs). Examples of DG are renewable energy sources such as wind turbines, PV arrays, and small-scale hydro power, but also non-renewable energy sources such as reciprocating engines and gas turbines [11], [12]. Typical ESSs are several diffent types of battery technology, supercapacitors and flywheel storage [13].

Two particular DERs attracting extraordinary focus in the world today, in the process to assess the environmental challenges mentioned in chapter 1, are PV and battery storage. Combining the volatile nature of solar production with the ability of battery units to provide flexibility, comprises an energy system that can elude the relatively unpredictable nature of the sun. This way, DG and ESS can approximate

the functionality of conventional energy sources as coal, gas and even hydro, at least for a limited amount of time.

Another salient feature of most DERs, is their extensive utilization of power electronic converters. These converters are deployed to enable the interconnection of DERs to the microgrid as well as the main grid.

A much used type of converter is the Voltage Source Converter (VSC) [14]–[17]. It is also called Voltage Source Inverter (VSI), as it most often inverts production side DC into grid side AC.

2.2.2 Loads

Loads in a microgrid are often divided into two types: fixed and flexible [18]. The former is, as the name states, fixed, and offers no flexibility with regards to power flow control. These loads can be viewed as critical, i.e. they should be prioritized during standard operating conditions. Examples of such loads include banking systems, semiconductor industries, hospitals and data centers. In this sense, the microgrid provides uninterruptible power supply (UPS) funcionality, which is a beneficial feature of the microgrid concept [12].

Microgrid power balancing/frequency stability in island mode can be a challenging task, due to low inertia in systems with power electronic interfaced DG [19]. Demand response should be emphasized to ease this challenge. This implies shedding loads to help maintain power balance.

Demand response will not only allow for additional flexibility in the microgrid, but can also optimize dispatch of DG and ESS [20]. The loads categorized as flexible fill this role as they are curtailable and/or deferrable and thus represent the load side flexibility with regards to control.

2.2.3 Point of Common Coupling (PCC)

The microgrid bus is often connected to the main grid at one single point, although the provided definition by CIGRÉ does not include this characteristic. This single point is referred to as the Point of Common Coupling (PCC). The connection to the grid, which is of a binary nature, can be realized with circuit breakers, solid-state switches or power electronic [19], where the preferred switchgear in microgrids is a switch [11]. In standard operation, surplus energy of the microgrid should flow towards the grid via the PCC. Similarly, when the microgrid is experiencing energy deficiency, it should import the needed power from the main grid to maintain power balance.

Microgrids that do not inhibit a PCC are called isolated microgrids, as they have no connection to a main grid and operate continually in island mode [19].

2.3 Voltage Configuration

Having established the standard elements of a microgrid, a fundamental question regarding interoperability arises. How can components of both AC and DC at different voltage levels be interconnected in a microgrid? The answer is often to establish a common DC or AC bus to interconnect all elements. An illustration of a typical AC and DC microgrid can be observed in 5.

Both technologies inherit advantages and disadvantages, meticulously investigated in [11]. There is also a possibility to have no common voltage bus and operate AC and DC distribution lines separately. This is called a hybrid AC/DC microgrid [11].

As there is no common global voltage level for manufactured electrical components, elements connected to the AC or DC bus in a microgrid must have an additional power electronic interface if their output voltage and/or frequency does not match the bus voltage and frequency. This implies a loss of inertia compared to the traditional grid, where synchronous generators act as a premier protection mechanism against sudden load or production [18]. This is part of what is regarded as primary control, and is elaborated in Section 2.6.

The choice of an AC or DC system is not evident as both configurations display both benefits and disadvantages that will not be investigated in this report. Summarized, the DC system configuration might be preferred, as it features a low system cost, simple structure and fewer power electronic converters compared to its AC counterpart [12]. The main advantage of choosing an AC configuration seems to be the seamless connection to the system's loads, as no converter is needed between them and the supplying AC bus.

2.4 Modes of Operation

Microgrids have two modes of operation, namely island mode and grid connected mode. Both modes have individual characteristics, especially with regards to control.

2.4.1 Island Mode

Island mode is defined as the mode when the microgrid operates without connection to the main grid [7]. A significant change in a load could be critical as the load can constitute a substantial part of the total load if the microgrid is small. The same apply to the fallout of a production unit. This characteristic is different from the main grid, where singular load and production changes usually only affect the grid stability marginally, and the control system is designed thereafter. This difference between microgrids and the main grid is important to bear in mind when designing the control system of the microgrid [21].

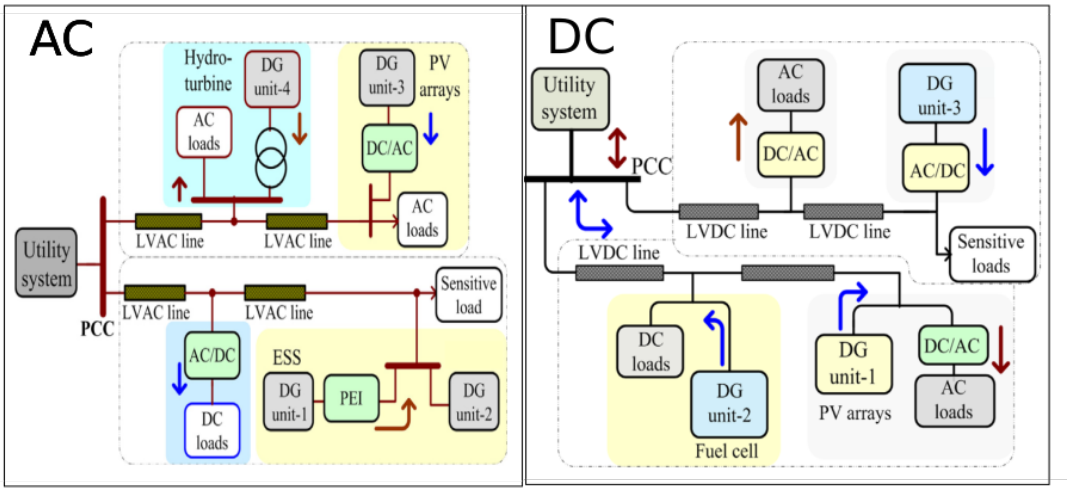

Figure 5: Illustration of typical AC and DC microgrids.

2.4.2 Grid Connected Mode

In grid connected mode, the microgrid must synchronize its frequency phase angle with the main grid. This is commonly done with a Phase Locked Loop (PLL), which is further described in section 2.6.1.

During this mode the microgrid has the opportunity to provide ancillary services to the grid, e.g. active and reactive power compensation, and harmonic compensation [21]. Moreover, it has the opportunity to import power from the main grid in case of power shortage internally in the microgrid, representing a safety net if the internal control system of the microgrid fails. Microgrids should however be designed to be able to sustain themselves [22].

2.5 Fault Characteristics

The protection scheme of the traditional power system is based on a unidirectional current flowing from the main grid towards the fault location [23]. This current is referred to as the short circuit current, and the corresponding protection scheme is designed with the magnitude of this current in mind. Relatively simple measures consisting of overcurrent relays, fuses, circuit breakers and reclosers can be deployed to isolate the fault location and maintain ordinary grid operation [23]. The different

protective entities are coordinated to ensure that the protection device closest to the fault location trips first, minimizing consequences of the fault.

Deploying a microgrid structure implies the presence of several production units and thus bidirectional power flow. It also implies very different scenarios during grid connected and island mode operation with regards to protection. When grid connected, a large short circuit current will flow from the main grid, allowing for the conventional protection devices to function properly. However, the current flowing towards the fault from nearby DG units has a chance of disturbing the coordination between protection devices, leading to a larger isolated area than necessary [12], [24].

During island operation, fault currents of the order of magnitude that conventional protection schemes are designed for, are not present [24]. This is due to the inherent fault current limitations of power electronic converters of about 2-3 p.u. of their rated current [12]. As such converters are close to ubiquitous in microgrids, it must be taken into consideration when designing a microgrid protection scheme.

The mentioned characteristics implies a worst case scenario in island mode of faults occurring, implicated power balance and frequency, but no fuses blowing as they are dimensioned for higher fault currents than the ones present. The entire microgrid operation is then in danger of collapsing, highlighting the need for a responsive protection scheme.

Due to the shown challenges of microgrid protection, specific features must be kept in mind when designing the microgrid protection scheme. The following features are considered necessary [23]:

1. The microgrid must respond to faults in both the distribution system and internal faults.

2. The microgrid must be isolated as quickly as possible during faults in the main grid, allowing for normal microgrid operation and affecting the main grid to a minimum degree.

3. An internal fault in the microgrid should be isolated affecting the rest of the microgrid to a minimum. This implies isolating as small a part as possible.

4. The protection of the consumers in the microgrid must be a top priority.

As assessing protection solutions is not within the scope of this report, the indicated challenges are not evaluated any further.

2.6 Control

Traditionally the approaches to control the power system, i.e. the measures taken to ensure stable operation, can be illustrated by two opposite strategies: centralized and decentralized [25]. The centralized control configuration in its purest form relies on communication between one central controller and all controllable units

in the power system. This demands extensive Information and Communications Technology (ICT) infrastructure between the controller and the units to enable fast response to changes. On the contrary, the decentralized approach bases its structure on local control where no controllable entities communicate directly with any other unit, but base its control on measurements of local quantities [26].

The massive, interconnected power system of Norway today stretches across the entire nation, making a centralized approach unsuitable. Simultaneously, a fully decentralized approach will have trouble coping with the level of dynamics in the system; A power outage in the north of the country might not trigger needed measures in the south. The solution is a mixture of the mentioned power system approaches where a hierarchical control strategy is implemented, namely consisting of a primary, secondary and tertiary control level [12], [19]. These control levels differ in their speed of response and their use of ICT, and is widely seen as the approach of choice for microgrids as well as for the main grid [12], [19], [21], [22], [27]. A description of the levels can be adopted as in the following subsections, where primary control is divided into two segments [27]. This level is also more elaborated, as secondary and tertiary control has limited relevance for the simulations done in this report. In addition, the work planned for the master thesis will not be relevant for the two upper layers.

Figure 6 show the different control layers and their role in controlling the microgrid.

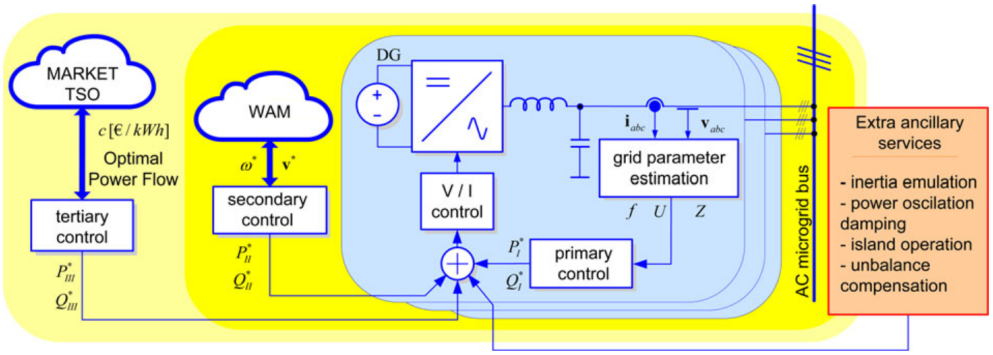

Figure 6: The different control layers of a microgrid [21].

2.6.1 Primary Control

Primary control is also called local or field control [25]. The tasks of this control level comprise of converter output control, power sharing mechanisms and island detection [19], which are all tasks of critical nature to microgrid stability. This implies the need for a fast response time in the scale of milliseconds [22]. Figure 7 provides an example of the structure of primary control.
As converter output control and power sharing control utilize separate techniques, it is purposeful to introduce them separately.

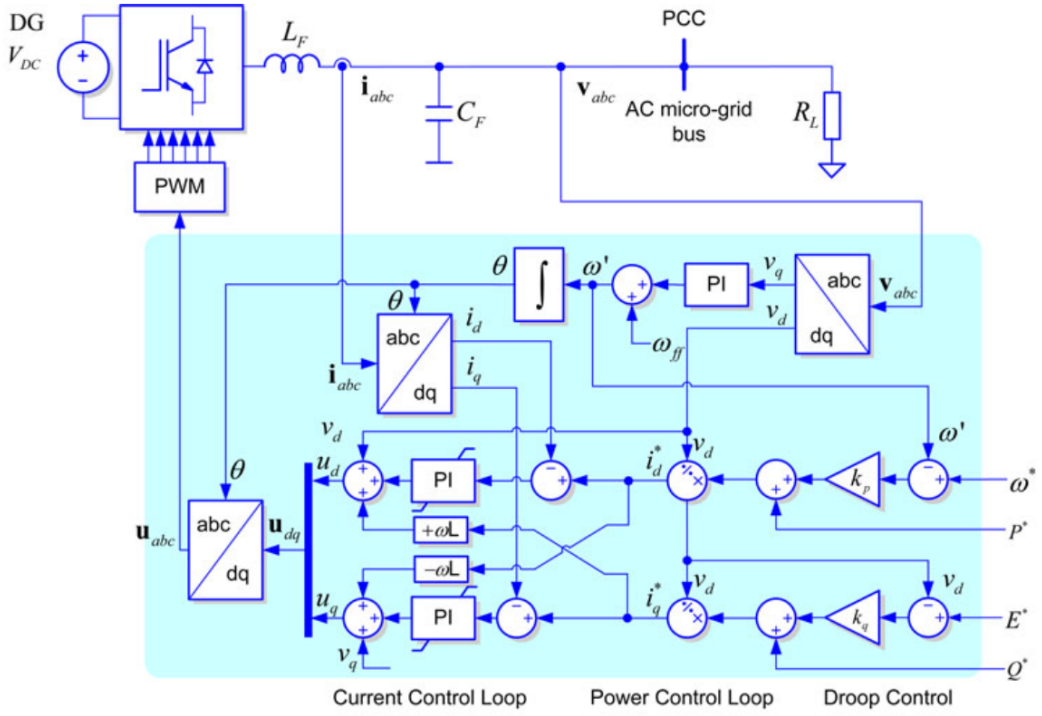

Figure 7: Typical structure of primary control [21].

Converter output control

This control structure typically consists of an outer voltage control loop and an inner current control loop [19], which can be identified in Figure 7. The most frequently used reference frames for implementing linear current controllers in three-phase systems are either the dq synchronous reference frame or the stationary reference frame ($\alpha\beta$) [21]. Controllers associated with these reference frames, and the natural reference frame, can be found in Table 1 [19].

Table 1: Reference frames used in converter control and its associated controllers [19].

Reference frame	**Associated controller**
Synchronous (dq)	Proportional Integral (PI)
Stationary ($\alpha\beta$)	Proportional Resonant (PR)
Natural (abc)	PI, PR, hysteresis, dead-beat

Inspecting Fig. 7, several essential characteristics of converter output control using the dq frame is observed:

1. abc quantities are transformed into dq quantities to be able to conduct regular PI control.

2. The strong coupling between the d and q axes is mitigated by cross coupling and feed-forward of the grid voltages. This is a standard procedure to improve control performance in terms of dynamic response [16].

3. The phase angle of the voltage frequency is extracted to be ensure that the converter is in phase with the grid voltage. This procedure is known as Phase Locked Loop (PLL).

In brief, the role of the converter output control is to track its reference quantities of voltage and current, and in addition ensure damping of any oscillations occurring [19].

Power sharing control Although a microgrid consisting of only one converter is possible, e.g. with a small scale hydro unit (with no power electronic interface) and an ESS utilizing a converter, most microgrids will consist of several power electronic converters. This implies a need for some sort of technique to coordinate the power sharing between them, which is either done in a centralized (with ICT) or decentralized manner (without ICT).

The centralized techniques used to coordinate parallel converters can be categorized into four different types. These are centralized control, master-slave control, average-load sharing or circular-chain controls [28]. All these techniques do however depend upon close proximity of the inverters and high-bandwidth communication channels to function properly [21]. These characteristics severely degrade the value of a centralized power sharing strategy for microgrids, where loads and generators in principle can be separated by several kilometers. In addition, the technique has an inherent weakness in its dependecy on ICT; If communication fails during island mode, the microgrid operation will collapse [19].

The decentralized technique is based on droop control algorithms. It utilizes measurements of local parameters and fixed droop characteristics to control the exchange of active and reactive power [27]. The concept of droop control can be viewed as virtual inertia, imitating primary control of traditional power systems having synchronous generators directly coupled to the grid. When an unbalance occurs in such power systems, the inertia of these generators balances the power at the loss or gain of system frequency. This characteristic is the basis of conventional primary control, called active power/grid frequency (P/f) droop control [29]. This characteristic coupling, in addition to the coupling between reactive power and voltage, comprise the inertia mimicked by microgrid droop control. Typical droop characteristics for an inductive network can be observed in Fig. 8.

However, it is important to note that this coupling can be done because the transmission grid primarily is inductive. The distribution system, including microgrids, is primarily resistive, limiting the efficiency of implementing this type of droop control [22]. Resistive networks imply a stronger coupling between active power and voltage, and frequency and reactive power, respectively [29]. This leads to P/V control instead of P/f.

Furthermore, conventional droop control has several additional disadvantages. These are identified in literature:

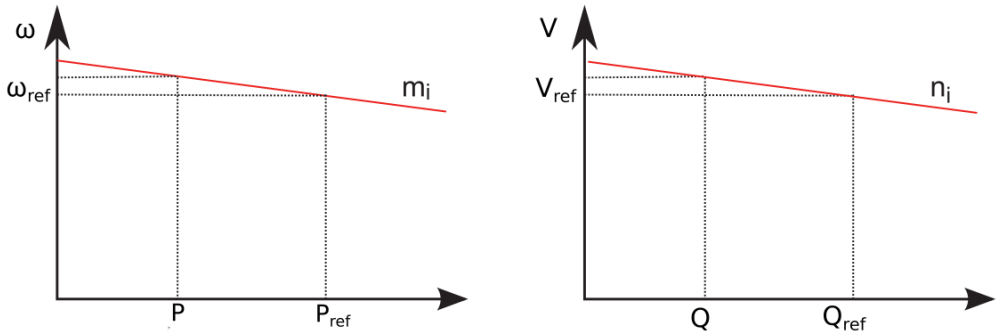

Figure 8: Typical droop characteristics of frequency and voltage in an inductive network [25].

1. Average values of P and Q are used, leading to limited transient performance and issues with stability [19].
2. It does not take load dynamics into account, thus running a risk of failure in the case of abrupt or large change of load [19].
3. No ability of black start if the system collapses [19].
4. It does not take into consideration the rating of the DER units, leading to the possibiliy of uneven power sharing and overstressing smaller units. Additional techniques, e.g. virtual impedance, must then be implemented [30].
5. It does not take into account harmonic components injected by nonlinear loads. Additional techniques must then be implemented. Virtual impedance is also a valid measure to mitigate this problem [19].
6. It is based on a coupling between system frequency and loading conditions, making it unable to impose a fixed system frequency [19].
7. Voltage is not a defined global variable. Hence, reactive power sharing can prove difficult to implement, in addition to circulating reactive current occurring [31].

Summarized, the task of the droop control is to adjust converter output control when unexpected changes in voltage and frequency occur. This means that the reference values of the converters are set by the the droop functions given in eq. (1). In this example, for an inductive network.

$$\begin{aligned} \omega &= \omega_{ref} - m_i(P - P_{ref}) \\ V &= V_{ref} - n_i(Q - Q_{ref}) \end{aligned} \tag{1}$$

As mentioned, other power sharing techniques do exist. However, due to the limited scope of this report, they are not discussed in detail.

2.6.2 Secondary Control

Secondary control can be thought of as control on a management level [25]. This is also referred to as the microgrid Energy Management System (EMS) as its responsibility is to safeguard the reliable, secure and economical operation of the microgrid in both grid connected and island mode [19]. Its responsibility includes optimizing the dispatch of the microgrid, taking into account criteria like electricity market prices, grid security and optimization of local production with regards to efficiency [25].

To decouple the secondary level from the primary level of control, the response is slower. Furthermore, the secondary level reduces bandwidth of communication by using sampled measurements. Lastly, the slow response allow enough time for complex calculations [32].

2.6.3 Tertiary Control

Tertiary control can be regarded as control on a grid level. This level controls the flow of power between the main grid and the microgrid. Moreover, this level sets set points for microgrid production and behaviour based on demand of the microgrid-connected power system [19].

Tertiary control is also responsible for coordination in the case of several microgrids interacting with each other, and can be considered part of the main grid [19]. During islanding this level is naturally nonexistent, as there is no grid interaction.

2.7 Benefits and Disadvantages of Microgrids

Evaluating the elaborated microgrid characteristics in this Chapter, it is evident that microgrids inherit both advantages and represent challenges. This Section provides an overview of these, and has the function of introducing the choice of the next Chapter.

2.7.1 Benefits

1. *Facilitating the implementation of DERs.* As mentioned in the Introduction, microgrid deployment is an effective way if integrating the rising number of renewable DERs [27], [33], facilitating the development of a low carbon society.

2. *Improved reliability of supply.* Reliability is normally evaluated with regards to system and customer interruption frequency using indices such as SAIFI and SAIDI [18]. In the case of transmission line outage, deploying a microgrid structure can improve the mentioned indices as a microgrid can enter island mode and thus function normally until the utility grid is functioning properly again [18], [33]. In effect the microgrid can then be viewed as a Uninterruptible Power Supply (UPS), often deployed today at critical loads such as hospitals [12].

3. *Improved resiliency against extreme events.* With extreme weather intensifying in both occurrence and strength due to global warming, the traditional utility grid faces recurring challenges regarding resiliency. Allowing microgrids to be supplied by local loads during these extreme events heightens the resilience of the entire system [18].

4. *Lower alternative costs.* Implementing DERs comes with a lower construction and deployment time and cost than the alternative, i.e. transmission and distribution of remotely produced energy [18].

5. *Alleviate stress on the existing grid.* Microgrids can provide flexibility in terms of stress to the existing grid, e.g. by supplying the grid during peak hours [33].

6. *Increase feasibility of rural electrification.* Microgrids can provide electricity to areas which are not feasible for the main grid to supply, either due to cost or difficult geographical locations [18].

7. *Ancillary services provided by power electronic devices.* Most power electronic devices are self-commutated, i principle allowing the devices to provide a customized voltage phase and amplitude. This is in fact the functionality of a Static Synchronous Compensator(STATCOM). As microgrids usually consist of several power electronic devices, this opens up the possibility of comprehensive reactive power regulation and power quality conditioning [18], [34].

2.7.2 Disadvantages

1. *Transition between island and grid connected mode.* The microgrid testbeds of the world have had severe difficulties in transitioning seamlessly between the modes of operation [33].

2. *Protection system response.* The protection system responding to both island and grid connected mode in a optimal manner has proven to be very challenging [12].

3. *Coordination between entities.* Coordinating the elements of a microgrid becomes additionally difficult when taking factors such as power balance, component failure rates, load profile and weather forecast into account [19].

4. *Bidirectional power flow.* The standard for distribution feeders and transformers is a unidirectional power flow. Changing this can lead to issues regarding protection ("tripping") coordination, undesirable circulating currents, fault current distribution and voltage instability [19].

5. *Exact mathematical modeling.* Conventional modeling of transmission systems comprise of balanced conditions, inductive lines and relatively small immediate fluctuations in production and load [19]. This is often not the case for microgrids, thus models need to be reevaluated.

6. *Low inertia.* The absence of synchronous generators in microgrids with a high number of power electronic devices imply a deficiency of inertia. This means the system does not have an inherent premier stability mechanism and must implement one to avoid large frequency deviations or, in worst case, system collapse [19].

7. *Power quality.* Several challenges related to power quality arise in microgrids. A selection of the most imminent of these challenges are elaborated in Chapter 3, including presence of low and high order harmonics as well as voltage sag.

All challenges listed are areas of extensive research and clearly has the potential of additional elaboration. However as the scope of this report is limited, the choice of further investigation is in the field of power quality in microgrids.

References

[1] United Nations, *Current status on Paris Agreement ratification*, 2017. [Online]. Available: http://unfccc.int/paris%7B%5C_%7Dagreement/items/9485.php.

[2] UNFCCC, "Paris Agreement," *Conference of the Parties on its twenty-first session*, vol. 21932, no. December, p. 32, 2015, ISSN: 1098-6596. DOI: FCCC/CP/2015/L.9/Rev.1. arXiv: arXiv:1011.1669v3. [Online]. Available: http://unfccc.int/files/essential%7B%5C_%7Dbackground/convention/application/pdf/english%7B%5C_%7Dparis%7B%5C_%7Dagreement.pdf%7B%5C%%7D0Ahttp://unfccc.int/resource/docs/2015/cop21/eng/109r01.pdf.

[3] International Energy Agency, *Launch presentation of Renewable Energy Market Report 2017*, 2017. DOI: 10.1787/re_mar-2017-en. [Online]. Available: https://www.iea.org/media/publications/mtrmr/Renewables2017LaunchPresentation.pdf.

[4] ——, *Renewables 2017 Analysis and Forecasts to 2022 Executive Summary*, 2017. DOI: 10.1016/S1471-0846(04)00194-5. [Online]. Available: http://www.iea.org/media/publications/mtrmr/Renewables2017ExecutiveSummary.PDF%7B%5C%%7D0Ahttp://www.iea.org/media/publications/mtrmr/Renewables2017LaunchPresentation.pdf.

[5] Navigant Research, *Microgrid Deployment Tracker 2Q17*, 2017. [Online]. Available: https://www.navigantresearch.com/research/microgrid-deployment-tracker-2q17 (visited on 12/20/2017).

[6] World Energy Council, *World Energy Perspectives 2016 - Executive Summary*, 2016. [Online]. Available: https://www.worldenergy.org/wp-content/uploads/2016/09/Variable-Renewable-Energy-Sources-Integration-in-Electricity-Systems-2016-How-to-get-it-right-Executive-Summary.pdf.

[7] B. Lasseter, "Microgrids [distributed power generation]," Tech. Rep. Power Engineering Society Winter Meeting, 2001, pp. 146–149.

[8] R. Lasseter, "MicroGrids," *2002 IEEE Power Engineering Society Winter Meeting. Conference Proceedings (Cat. No.02CH37309)*, vol. 1, pp. 305–308, 2002, ISSN: 0275-9306. DOI: 10.1109/PESW.2002.985003. [Online]. Available: http://ieeexplore.ieee.org/lpdocs/epic03/wrapper.htm?arnumber=985003.

[9] C. Marnay, S. Chatzivasileiadis, C. Abbey, R. Iravani, G. Joos, P. Lombardi, P. Mancarella, and J. Von Appen, "Microgrid evolution roadmap," *Proceedings - 2015 International Symposium on Smart Electric Distribution Systems and Technologies, EDST 2015*, pp. 139–144, 2015. DOI: 10.1109/SEDST.2015.7315197.

[10] IEC, *IEC 60038:2009*, 2009. [Online]. Available: https://webstore.iec.ch/publication/153.

[11] E. Planas, J. Andreu, J. I. Gárate, I. Martínez De Alegría, and E. Ibarra, "AC and DC technology in microgrids: A review," *Renewable and Sustainable Energy Reviews*, vol. 43, pp. 726–749, 2015, ISSN: 13640321. DOI: 10.1016/j.rser.2014.11.067.

[12] J. J. Justo, F. Mwasilu, J. Lee, and J. W. Jung, "AC-microgrids versus DC-microgrids with distributed energy resources: A review," *Renewable and Sustainable Energy Reviews*, vol. 24, pp. 387–405, 2013, ISSN: 13640321. DOI: 10.1016/j.rser.2013.03.067. [Online]. Available: http://dx.doi.org/10.1016/j.rser.2013.03.067.

[13] E. Hossain, E. Kabalci, R. Bayindir, and R. Perez, "A Comprehensive Study on Microgrid Technology," *International Journal of Renewable Energy Research*, vol. 4, no. 4, 2014.

[14] R. N. Beres, S. Member, X. Wang, F. Blaabjerg, M. Liserre, C. L. Bak, and S. Member, "Optimal Design of High-Order Passive-Damped Filters for Grid-Connected Applications," *IEEE Transactions on Power Electronics*, vol. 31, no. 3, pp. 2083–2098, 2016.

[15] R. N. Beres, S. Member, X. Wang, M. Liserre, F. Blaabjerg, C. L. Bak, and S. Member, "A Review of Passive Power Filters for Three-Phase Grid-Connected Voltage-Source Converters," *IEEE Journal of Emerging and Selected Topics in Power Electronics*, vol. 4, no. 1, pp. 54–69, 2016.

[16] A. Timbus, M. Liserre, R. Teodorescu, P. Rodriguez, and F. Blaabjerg, "Evaluation of Current Controllers for Distributed Power Generation Systems," *IEEE Transactions on Power Electronics*, vol. 24, no. 3, pp. 654–664, 2009.

[17] R. P. Rekha and E. R. Limpaecher, "Development of a Real-Time Hardware-in-the-Loop Power Systems Simulation Platform to Evaluate Commercial Microgrid Controllers," no. February, 2016. [Online]. Available: https://ll.mit.edu/mission/engineering/Publications/TR-1203.pdf.

[18] S. Parhizi, H. Lotfi, A. Khodaei, and S. Bahramirad, "State of the art in research on microgrids: A review," *IEEE Access*, vol. 3, pp. 890–925, 2015, ISSN: 21693536. DOI: 10.1109/ACCESS.2015.2443119.

[19] D. E. Olivares, A. Mehrizi-Sani, A. H. Etemadi, C. A. Cañizares, R. Iravani, M. Kazerani, A. H. Hajimiragha, O. Gomis-Bellmunt, M. Saeedifard, R. Palma-Behnke, G. A. Jiménez-Estévez, and N. D. Hatziargyriou, "Trends in microgrid control," *IEEE Transactions on Smart Grid*, vol. 5, no. 4, pp. 1905–1919, 2014, ISSN: 19493053. DOI: 10.1109/TSG.2013.2295514.

[20] F. Katiraei, R. Iravani, N. D. Hatziargyriou, and A. Dimeas, "Microgrids management," *IEEE Power and Energy Magazine*, vol. 6, no. 3, pp. 54–65, 2008.

[21] J. Rocabert, A. Luna, F. Blaabjerg, and I. Paper, "Control of Power Converters in AC Microgrids.pdf," *IEEE Transactions on Power Electronics*, vol. 27, no. 11, pp. 4734–4749, 2012, ISSN: 0885-8993. DOI: 10.1109/TPEL.2012.2199334.

[22] J. M. Guerrero, P. C. Loh, T. L. Lee, and M. Chandorkar, "Advanced control architectures for intelligent microgridsPart II: Power quality, energy storage, and AC/DC microgrids," *IEEE Transactions on Industrial Electronics*, vol. 60, no. 4, pp. 1263–1270, 2013, ISSN: 02780046. DOI: 10.1109/TIE.2012.2196889.

[23] A. R. Haron, A. Mohamed, and H. Shareef, "A Review on Protection Schemes and Coordination Techniques in Microgrid System," *Journal of Applied Sciences*, no. 12, pp. 101–112, 2012.

[24] H. J. Laaksonen, "Protection principles for future microgrids," *IEEE Transactions on Power Electronics*, vol. 25, no. 12, pp. 2910–2918, 2010, ISSN: 08858993. DOI: 10.1109/TPEL.2010.2066990.

[25] E. Planas, A. Gil-de-muro, J. Andreu, Kortabarria, Inigo, and I. M. de Alegria, "General aspects , hierarchical controls and droop methods in microgrids : A review," *Renewable and Sustainable Energy Reviews*, vol. 17, pp. 147–159, 2013. DOI: 10.1016/j.rser.2012.09.032.

[26] A. D. Paquette and D. M. Divan, "Providing improved power quality in microgrids: Difficulties in competing with existing power-quality solutions," *IEEE Industry Applications Magazine*, vol. 20, no. 5, pp. 34–43, 2014, ISSN: 10772618. DOI: 10.1109/MIAS.2013.2288377.

[27] J. M. Guerrero, J. C. Vasquez, J. Matas, L. G. De Vicuña, and M. Castilla, "Hierarchical control of droop-controlled AC and DC microgrids - A general approach toward standardization," *IEEE Transactions on Industrial Electronics*, vol. 58, no. 1, pp. 158–172, 2011, ISSN: 02780046. DOI: 10.1109/TIE.2010.2066534.

[28] J. M. Guerrero, L. Hang, and J. Uceda, "Control of Distributed Uninterruptible Power Supply Systems," *IEEE Transactions on Industrial Electronics*, vol. 55, no. 8, pp. 2845–2859, 2008.

[29] T. L. Vandoorn, J. C. Vasquez, J. De Kooning, J. M. Guerrero, and L. Vandevelde, "Microgrids: Hierarchical control and an overview of the control and reserve management strategies," *IEEE Industrial Electronics Magazine*, vol. 7, no. 4, pp. 42–55, 2013, ISSN: 19324529. DOI: 10.1109/MIE.2013.2279306.

[30] J. C. Vasquez, J. M. Guerrero, S. Member, M. Savaghebi, S. Member, J. Eloy-garcia, R. Teodorescu, and A. Power-electronics-based, "Modeling , Analysis , and Design of Parallel Three-Phase Voltage Source Inverters," *IEEE Transactions on Industrial Electronics*, vol. 60, no. 4, pp. 1271–1280, 2013.

[31] H. Han, X. Hou, J. Wu, M. Su, J. Yang, and J. M. Guerrero, "Review of Power Sharing Control Strategies for Islanding Operation of AC Microgrids," *IEEE Transactions on Smart Grid*, vol. 7, no. 1, pp. 200–215, 2016. DOI: 10.1109/TSG.2015.2434849.

[32] B. Marinescu and H. Bourles, "Robust Predictive Control for the Flexible Coordinated Secondary Voltage Control of Large-Scale Power Systems," *IEEE Transaction on Power Systems*, vol. 14, no. 4, pp. 1262–1268, 1999.

[33] M. Soshinskaya, W. H. Crijns-Graus, J. M. Guerrero, and J. C. Vasquez, "Microgrids: Experiences, barriers and success factors," *Renewable and Sustainable Energy Reviews*, vol. 40, pp. 659–672, 2014, ISSN: 13640321. DOI: 10.1016/j.rser.2014.07.198.

[34] B. Kroposki, C. Pink, R. Deblasio, H. Thomas, M. Simoes, and P. K. Sen, "Benefits of Power Electronic Interfaces for Distributed Energy Systems," *IEEE Transactions on Energy Conversion*, vol. 25, no. 3, pp. 901–908, 2010.

[35] IEC, *Definition of Power Quality*, 2009. [Online]. Available: http://www.electropedia.org/iev/iev.nsf/display?openform%7B%5C&%7Dievref=617-01-05.

[36] Ministry of Petroleum and Energy, *Forskrift om leveringskvalitet i kraftsystemet*, 2004. [Online]. Available: https://lovdata.no/dokument/SF/forskrift/2004-11-30-1557%7B%5C#%7DKAPITTEL%7B%5C_%7D3.

[37] S. Whaite, B. Grainger, and A. Kwasinski, "Power Quality in DC Power Distribution Systems and Microgrids," *Energies*, vol. 8, no. 5, pp. 4378–4399, 2015. DOI: 10.3390/en8054378.

[38] P. Basak, S. Chowdhury, S. Halder, and S. P. Chowdhury, "A literature review on integration of distributed energy resources in the perspective of control , protection and stability of microgrid," *Renewable and Sustainable Energy Reviews*, vol. 16, no. 8, pp. 5545–5556, 2012, ISSN: 1364-0321. DOI: 10.1016/j.rser.2012.05.043. [Online]. Available: http://dx.doi.org/10.1016/j.rser.2012.05.043.

[39] N. Mohan, T. M. Undeland, and W. P. Robbins, "Power electronics: converters, applications, and design," in, 3rd, Wiley, 2003, ch. 8, ISBN: 0471226939.

[40] Y. W. Li and J. He, "Distribution system harmonic compensation methods: An overview of DG-interfacing inverters," *IEEE Industrial Electronics Magazine*, vol. 8, no. 4, pp. 18–31, 2014, ISSN: 19324529. DOI: 10.1109/MIE.2013.2295421.

[41] E. F. Fuchs, *Power quality in power systems and electrical machines*, 2nd. Academic Press, 2015, p. 28, ISBN: 9780128007822. DOI: 10.1016/B978-0-12-800782-2.00001-4.

[42] M. Sclocchi, "Input Filter Design for Switching Power Supplies," National Semiconductor Corporation, Tech. Rep., 2010. [Online]. Available: http://www.ti.com/lit/an/snva538/snva538.pdf.

[43] S. Papathanassiou, H. Nikos, and S. Kai, "A benchmark low voltage microgrid network," *Proceedings of the CIGRE symposium: power systems with dispersed generation*, no. April, pp. 1–8, 2005. [Online]. Available: http://www.icevirtuallibrary.com/deliver/fulltext/ener163-143.pdf;jsessionid=fashh6hedd0n5.x-telford-live-01?itemId=/content/article/10.1680/ener.2010.163.4.143%7B%5C%%7D7B%7B%5C&%7D%7B%5C%%7D7DmimeType=pdf%7B%5C%%7D7B%7B%5C&%7D%7B%5C%%7D7DisFastTrackArti.

[44] F. Blaabjerg, R. Teodorescu, S. Member, M. Liserre, A. V. Timbus, and S. Member, "Overview of Control and Grid Synchronization for Distributed Power Generation Systems," *IEEE Transactions on Industrial Electronics*, vol. 53, no. 5, pp. 1398–1409, 2006.

[45] R. Teodorescu, F. Blaabjerg, M. Liserre, and P. C. Loh, "Proportional-resonant controllers and filters for grid-connected voltage-source converters," *IEE Proceedings - Electric Power Applications*, vol. 153, no. 5, 2006. DOI: 10.1049/ip-epa.

[46] J. Castano, "High Performance Voltage Control For Three-Phase UPS Inverter," PhD thesis, Universidade Federal do Rio de Janeiro, 2014.

[47] P. Rodriguez, A. Luna, I. Etxeberria, J. R. Hermoso, and R. Teodorescu, "Multiple second order generalized integrators for harmonic synchronization of power converters," *2009 IEEE Energy Conversion Congress and Exposition, ECCE 2009*, no. 1, pp. 2239–2246, 2009, ISSN: 1553-572X. DOI: 10.1109/ECCE.2009.5316279.